U.PORTO
FEUP FACULDADE DE ENGENHARIA
UNIVERSIDADE DO PORTO

Machinability of Maraging steel produced by LPBF based on milling tests

Miguel Silva Pinto Duro

Master's dissertation in Mechanical Engineering

Supervisor:
Prof. Dr. Abílio Manuel Pinho de Jesus

Co-Supervisor:
Dr. Tiago Emanuel Fraga Silva

July 2022

Abstract

Metal additive manufacturing is an emerging technology that allows the production of mechanical components with technical specifications suitable for structural applications, with a high level of complexity. Although large investments have been made in these technologies in recent years, these processes do not currently allow parts to be obtained with the geometrical, dimensional accuracy and surface finish level required for precision mechanical assembly. This factor often leads to the need for post-processing operations through precision machining technologies in order to comply with demanding geometrical and dimensional tolerances (required for their applications).

The present dissertation focuses on the machinability study of 18Ni300 maraging steel obtained by laser powder bed fusion as well as its comparison with the same alloy conventionally produced. Initially a brief characterisation of the two materials was performed with analysis of the chemical composition, hardness, microstructure, residual stress, roughness and, particularly for the additively manufactured material, also porosity. Next, an experimental milling tests campaign was carried out for a wide range of cutting parameters (feed, depth of cut and cutting speed) aiming at understanding their influence and comparing the obtained results in terms of cutting force, specific cutting pressure, roughness, residual stress, hardness, and chip morphology. Along with the experimental campaign, numerical simulations of the milling process in identical conditions to the experimentally conducted were performed using a material model that was previously calibrated for the same material. In short, a greater influence of the feed rate parameter on the analysed data is noticed. Moreover, the superior mechanical strength of the additively manufactured alloy, does not translate into an equivalent increase in the required specific cutting pressure. The numerical simulation revealed a good performance in the characterisation of the stability plateau of specific cutting pressures recorded in this material, which confirms the effectiveness of the employed approach.

Resumo

O fabrico aditivo metálico é uma tecnologia emergente que permite a produção de componentes mecânicos com especificações técnicas adequadas para aplicações estruturais, com elevado nível de complexidade. Embora grandes investimentos tenham sido realizados nestas tecnologias nos últimos anos, estes processos não possibilitam ainda a obtenção de peças com o rigor geométrico, dimensional e acabamento superficial necessários para uma montagem mecânica de precisão. Este fator frequentemente leva à necessidade de operações de pós-processamento através de tecnologias de maquinagem de precisão com vista a estar em conformidade com as requeridas tolerâncias geométricas e dimensionais (necessárias às suas aplicações).

A presente dissertação foca-se no estudo da maquinabilidade do aço maraging 18Ni300 obtido por sinterização laser em cama de pó assim como a sua comparação com a mesma liga produzida de forma convencional. Inicialmente é feita uma breve caracterização dos dois materiais com análise da composição química, dureza, microestrutura, rugosidade e ainda, em particular para o material produzido por fabrico aditivo, porosidade. Em seguida, realizou-se uma campanha experimental de testes de fresagem para uma vasta gama de parâmetros de corte (avanço, profundidade de corte e velocidade de corte) com o objetivo de compreender a sua influência e comparar os resultados obtidos principalmente em termos de força de corte, pressão específica de corte, rugosidade e morfologia da apara. A par da campanha experimental, foram realizadas simulações numéricas do processo de fresagem em condições idênticas às utilizadas nos ensaios experimentais utilizando para isso um modelo calibrado anteriormente para o mesmo material. Em suma, foi observada uma maior influência do parâmetro de avanço nos dados recolhidos. Para além disso, a maior resistência mecânica da liga de fabrico aditivo não se traduziu num aumento equivalente da pressão específica de corte necessária. A simulação numérica revelou um bom desempenho na caracterização do patamar de estabilidade de pressões especificas de corte registadas neste material, o que confirma eficácia da abordagem utilizada.

Acknowledgements

The realisation of this dissertation had the contribution of many people, to whom I am deeply grateful and could not forget to give a word of appreciation.

First of all, I would like to express my sincere gratitude to Professor Abílio de Jesus for his continuous support, availability, motivation and commitment during the last months. Your ability to deconstruct and simplify problems as well as your knowledge were central to the writing of this dissertation.

I am also deeply grateful to Dr. Tiago Silva for his precious help, availability, and constant willingness throughout the work. I commend his continuous effort throughout these months to monitor me in the best way.

I extend my appreciation to INEGI for all the work conditions and technical support. A kind word must be given to Armanda Marques for her precious help, availability provided during the development of this work.

I leave a word of appreciation to Professor Maria José Marques for her support, availability and help in the analyses that contributed to the enhancement of this work.

I would also like to thank Mr. José Bouças for his patience and help with the experimental part of this work and Dr. Filipe Silva, Eng. Omid Emadinia and Mr. Domingos Carvalho, for their precious contributions.

Moreover, I would like to acknowledge Palbit S.A. for the given support and counselling provided to the whole project.

Furthermore, I would like to leave a word of appreciation to my dissertation colleagues Joana Silva, Francisco Matos and Renato Silva for their help, support and motivation throughout this work.

I am also grateful for the support, help and good atmosphere created by my office colleagues Alexandre Fabião, Gonçalo Soares and Tiago Santos.

Finally, I would like to thank my family and close friends for their constant motivation and help throughout these months.

The MAMTOOL project (Reference PTDC/EME-EME/31895/2017) entitled "Machinability of Additive Manufactured Parts for Tooling Industry" funded by the Competitiveness and Internationalization Operational Programme, and Lisbon Regional Operational Programme funded by FEDER and National Fund (FCT) is recognized.

The Mobilizing Agendas for Business Innovation (AVISO No. 02/C05-I01/2022), in particular the agenda Hi-rEV - Automotive Components Industry (C644864375-00000002) is recognized for the support granted.

Contents

1. Introduction ... 1
1.1. Motivation and context ... 1
1.2. Goals ... 2
1.3. Thesis structure ... 3
2. Literature review ... 5
2.1. Metal cutting ... 5
2.1.1. Mechanics of metal cutting ... 5
2.1.2. Milling ... 9
2.1.3. Analytical models ... 12
2.1.4. Numerical modelling ... 18
2.2. Additive manufacturing ... 24
2.2.1. Powder bed fusion ... 26
2.2.2. Manufacturing parameters ... 28
2.2.3. Influence on material properties ... 29
2.3. Machinability of AM produced metals ... 33
3. Experimental and numerical procedures ... 37
3.1. Material characterisation ... 37
3.1.1. Optical and electron scanning microscopy and chemical analysis ... 38
3.1.2. Hardness, roughness, and residual stress analysis ... 39
3.2. Milling tests ... 41
3.2.1. Experimental setup ... 41
3.3. Simulation procedures ... 44
3.3.1. Constitutive model ... 45
3.3.2. Software ... 46
3.3.3. Milling model ... 46
4. Results and discussion ... 48
4.1. Material characterisation ... 48
4.1.1. Chemical analysis ... 48
4.1.2. Metallographic analysis and relative density ... 49

4.1.3. Surface and hardness analysis 50
4.2. Experimental milling tests results 51
4.2.1. Cutting forces 51
4.2.2. Specific cutting pressure 52
4.2.3. Surface roughness 56
4.2.4. Cutting insert wear tendencies 60
4.2.5. Taguchi method analyses 62
4.2.6. Hardness results on machined surfaces 62
4.2.7. Residual stresses 64
4.2.8. Chip morphology 66
4.3. Numerical simulation results 69
4.3.1. Cutting length calibration 69
4.3.2. FEM mesh sensitivity analysis 70
4.3.3. Material model definition 72
4.3.4. Friction calibration 72
4.3.5. Cutting forces and specific cutting pressures analysis 73
4.3.6. Chip modelling 74
5. Conclusions and future work 75
5.1. Conclusions 75
5.2. Future works 76
Bibliography 77

List of figures

Figure 1 - Additive manufacturing (powder bed fusion) and topological optimization of a Bugatti brake caliper: a) building process, b) final component [2]. 1
Figure 2 - Temperature distribution on plastic injection mould insert using conventional drilled and additively manufactured conformal cooling channels [4]....................2
Figure 3 - Most common conventional machining processes: drilling, turning, face milling, peripheral milling, adapted from [5]. 6
Figure 4 - Simplification of the cutting phenomena: a) Oblique cutting; b) orthogonal cutting, adapted from [7]....................7
Figure 5 - Main angles in orthogonal cutting: rake angle, γ, clearance angle, α, wedge angle, ß, shear angle, ϕ, adapted from [5]. 7
Figure 6 - Shear zones in chip formation, adapted from [5]....................8
Figure 7 - Most common chip formation mechanisms: a) Continuous chips; b) continuous chips with BUE; c) serrated chips; d) discontinuous chips, adapted from [5]....................9
Figure 8 - Cutting insert for turning operations showing cutting edge and rake cross-section: a) without and b) with chip breaker, adapted from [10]. 9
Figure 9 - Milling processes, adapted from [9]....................10
Figure 10 - a) Down-milling; b) Up-milling, adapted from [5]. 10
Figure 11 - Tool-workpiece engagement parameters in plain face milling, adapted from [9].......11
Figure 12 - a) Components of milling cutting forces, b) Cutting force components evolution during engagement, adapted from [11]. 12
Figure 13 - Analytical models: a) shear plane model, b) slip line field model, c) shear zone model, adapted from [5]....................12
Figure 14 - Force diagram in orthogonal cutting, adapted from [9]. 13
Figure 15 - Lee and Shaffer's slip-line field solution for orthogonal cutting, adapted from [15]. .15
Figure 16 - ALE scheme models with different boundary conditions: a) pure Lagrangian boundary conditions; b) pure Eulerian boundary conditions, adapted from [24]. 19
Figure 17 - Idealized plastic behaviour of materials: a) Linear work-hardening; b) Nonlinear work-hardening, adapted from [28]....................20
Figure 18 - Temperature distribution comparison between a FEM model developed by Stevenson et al. (continuous lines) and experimental results obtained by a metallographic method (dashed lines), adapted from [38]....................22
Figure 19 - Comparison of a meshfree (a) and a FEM (b) simulation, adapted from [44]. 23
Figure 20 - Remeshing process in DEFORM software during cutting simulation (a)-c)). 23
Figure 21 - Manufacturing processes: a) Additive, b) subtractive, c) formative, adapted from [45]. 25
Figure 22 - Less commonly used processes MAM processes: a) material extrusion, b) binder jetting, c) sheet lamination, adapted from [45]. 25
Figure 23 - Laser-based Direct Energy Deposition process diagram, adapted from [47]. 26

Figure 24 - Laser-based Powder Bed Fusion process diagram, adapted from [47]. 27
Figure 25 - Scanning geometry parameters: hatch spacing, layer thickness and scanning speed, adapted from [51]. 28
Figure 26 - Different scanning strategies: a) unidirectional, b) bidirectional, c) sectorial ("chessboard"), d) bidirectional with linear melting of the contours; different scanning schemes: e) stripes alternating 45°, f) stripes alternating 90°, g) chess with adjacent blocks alternating 90°, h) chess with adjacent blocks alternating 45°, adapted from [52, 53]. 29
Figure 27 - Effect schematic of the energy density: a) lack of energy density; b) excess of energy density, adapted from [57] 30
Figure 28 - Metallographic samples of AM 18Ni300 in parallel (a) and in perpendicular direction (b) to building direction, adapted from [58]. 31
Figure 29 - SLM maraging steel microstructure with different magnifications: a) LOM picture adapted from [61], b) and c) SEM picture, adapted from [63]. 32
Figure 30 - Number of articles per year in Scopus on the subject of machining of metallic materials produced by additive manufacturing. 33
Figure 31 - Example of a car tyre maraging steel mould produced by additive manufacturing [67]. 34
Figure 32 - Schematic illustration including movable axes of the hybrid additive manufacturing machine used in the work of Wüst et al. [74] 36
Figure 33 - a) As-built AM material samples attached to build plate, b) CM steel plate, c) CM and AM specimens produced (dimensions: 120x20.5x20.5 mm3). 38
Figure 34 - Porosity analysis of AM produced parts: a) unetched metallographic sample, b) binary image. 38
Figure 35 - a) Optical microscope OLYMPUS PMG3; b) spark emission spectroscopy SPECTROMAXx; c) Scanning Electron Microscope (FEI Quanta 400FEG ESEM / EDAX Genesis X4M) at CEMUP 39
Figure 36 - a) Hardness measuring machine (EMCO® Test M4U-075), b) microhardness measuring device, c) hardness measurements diagram. 40
Figure 37 - a) Roughness evaluation with MITUTOYO Surftest SJ-210, b) residual stress measurement by x-ray diffraction (XRD). 40
Figure 38 - a) and b) Experimental setup with Kistler Rotating Cutting Force Dynamometer Type 9170 A, c) DMG Mori DMU 60 evo CNC used in the experimental tests. 41
Figure 39 - Experimental setup illustration of apparatus. 42
Figure 40 - a) and b) Milling shank geometry and dimensions, c) and d) cutting insert geometry and dimensions. 42
Figure 41 - Milling tests illustration setup and acquired loads labelling. 43
Figure 42 - Quasi-static numerical and experimental curves obtained by Silva [18]. 46
Figure 43 - Example of the remeshing procedure during the executed simulations. 47
Figure 44 - Different tested less (a) and more (b) refined meshes. 47

Figure 45 - Electrolytically etched metallographic samples of AM 18Ni300 in parallel (a) and in perpendicular to build direction (b); chemically etched samples of CM 18Ni300 (c); unetched metallographic sample showing voids occurrence in AM 18Ni300 (d). 49
Figure 46 - SEM image highlighting the difference between an AM and a machined surface. 50
Figure 47 - Overview of the conducted milling tests. 51
Figure 48 - a) Experimental correlation between Fc and Ff, Fz; b) Cutting force in function of feed, for different depths of cut and materials. 52
Figure 49 - Specific cutting pressure, Kc, in function of feed, f, for: a) all the tests, b) comparison of AM and CM 18Ni300 steel. 53
Figure 50 - Chip geometry for ap = 0.2 mm and f = 0.05 mm/rev. 53
Figure 51 - Specific cutting pressure, Kc, in function of feed, f, for: a) different depths of cut, ap, and b) cutting speeds, vc. 54
Figure 52 - Specific cutting pressure, Kc, in function of feed, f, for different depths of cut, ap, for: a) AM, b) CM. 54
Figure 53 - Specific cutting pressure, Kc, in function of feed, f, for different cutting speeds, vc, for: a) AM, b) CM. 54
Figure 54 - Variation of specific cutting pressure, Kc, in function of: a) depth of cut, b) feed, c) cutting speed, d) material; e) influence of the different parameters in the specific cutting pressure. 55
Figure 55 - Comparison between the results of specific cutting pressure of this work and the work of Laínho [79], Couto and Silva et al. [78]. 55
Figure 56 - Experimental correlation between Ra and Rz, Rz max. 56
Figure 57 - Roughness, Ra, in function of feed, f, for: a) all the tests, b) the AM and CM 18Ni300 steel. 56
Figure 58 - Diagram of two successive passages of the cutting tool, for a_p = 0.6 mm and f = 0.2 mm/rev. 57
Figure 59 - Roughness, Ra, in function of feed, f, for: a) different depths of cut, a_p, and b) cutting speeds, v_c. 57
Figure 60 - Roughness, Ra, in function of feed, f, for different depths of cut, a_p, for: a) AM, b) CM. 57
Figure 61 - Roughness, Ra, in function of feed, f, for different cutting speeds, v_c, for: a) AM, b) CM. 58
Figure 62 - Variation of roughness, Ra, in function of: a) depth of cut, b) feed, c) cutting speed, d) material; e) influence of the different parameters in the specific cutting pressure. 58
Figure 63 - Comparison of machined surfaces for different feeds and materials: a) f=0.05 mm/rev, AM; b) f=0.1 mm/rev, AM; c) f=0.2 mm/rev, AM; d) f=0.2 mm/rev, CM, for a cutting speed of 200 m/min. 59
Figure 64 - a) Difference between a machined and an original AM surface, b) first and second pass of the tool registered on the surface. 59
Figure 65 - Defects of the machined surfaces: a) pores, b) chip dragging, c) and d) adhered material, e) and f) fragments of chips. 60

Figure 66 - Identification of different chemical compositions at the insert tip surface with EDS analysis, for v_c = 80 m/min, and AM material..61
Figure 67 - SEM observations of the cutting insert tips used with different conditions - AM: a) v_c = 80 m/min, b) v_c = 200 m/min c) v_c = 320 m/min; CM: d) v_c = 80 m/min, e) v_c = 200 m/min f) v_c = 320 m/min..61
Figure 68 - Comparison of the results between the total data and the Taguchi method in function of feed: a) comparison of global Kc, b) comparison of Ra, c) difference in Kc between materials, d) differences in Kc between different depths of cut. 62
Figure 69 - Variation of surface hardness with: a) feed, b) depth of cut, c) cutting speed and comparison with hardness measurements in non milled surfaces. 63
Figure 70 - Microhardness measurement: a) comparison with surface and original hardness, b) microhardness measurement marks, for v_c = 80 m/min, a_p = 0.6 mm, f = 0.2 mm/rev, AM. 64
Figure 71 - Microstructures of the profile cut samples: a) AM, b) CM. 64
Figure 72 - a) Evolution of residual stress along the AM and CM specimens, b) AM specimen...65
Figure 73 - Variation of residual stress in the machining direction (perpendicular to build direction) for different: a) feeds, b) depths of cut), c) cutting speeds, for the two materials. 65
Figure 74 - Variation of residual stress in the direction perpendicular to the machining direction (parallel to build direction) for different: a) feeds, b) depths of cut), c) cutting speeds, for the two materials. 66
Figure 75 - Chip evolution with the variation of the feed per revolution, f, and depth of cut, a_p, and the cutting speed, v_c, for the additive manufactured 18Ni300 steel.......................................67
Figure 76 - Chip evolution comparison between additive and conventional manufactured 18Ni300 steel with the variation of the feed per revolution, f, and depth of cut, a_p , for a cutting speed of 320 m/min..67
Figure 77 - Influence of feed in the morphology of the chips: a) f = 0.4 mm/rev, b) f = 0.6 mm/rev. 68
Figure 78 - Influence of depth of cut in the morphology of the chips: a) a_p = 0.2 mm, b) a_p = 0.6 mm, for a v_c=200 m/min and f=0.05 mm/rev. 68
Figure 79 - Influence of cutting speed in the morphology of the chips: a) v_c = 80 m/min, b) v_c = 320 m/min, for f=0.05 mm/rev and AM material. 68
Figure 80 - a) CM chip, b) surface generated by the cutting tool, c) AM chip, d) detail of powder particle..69
Figure 81 - Geometry of forces obtained by: a) simulation, b) experimental tests. 70
Figure 82 - a) Comparison of results of different engagement ranges of cut between 85º and 95º, b) cutting length of 80º-100º. 70
Figure 83 - Simulated cutting force comparison between different principal meshes: a) simulations b) comparison with simulation time. 71
Figure 84 - a) Comparison of different mesh size ratios for the secondary part mesh and b) comparison of different number of elements in tool mesh in simulation. 71
Figure 85 - a) Cutting length and computational cost of simulations for different feeds, b) mesh for f = 0.2 mm/rev, c) mesh for f = 0.05 mm/rev. 72

Figure 86 - Flow curves of AM maraging steel experimentally and numerically obtained by Silva [18], for different ranges of true plastic strain. 72
Figure 87 - Comparison of different friction coefficients in simulation results (vc = 320 m/min, ap = 0.6 mm, f = 0.2 mm/rev). 73
Figure 88 - Comparison of FEM and experimental results in terms of: a) specific cutting pressure, b) cutting force. 73
Figure 89 - Chip morphology: a) FEM, b) experimental tests, for f = 0.2 mm/rev and a_p = 0.6 mm. 74

List of tables

Table 1 - Shear angle analytical model according to different authors, adapted from [8, 18]. 16

Table 2 - Material constitutive model equations according to different authors [28]. 21

Table 3 - Most common damage criteria [8, 18, 25]. 24

Table 4 - Printing parameters of the AM 18Ni300 specimens: laser power, P_L, scan speed, v_s, hatch spacing, h_s, layer thickness, d_s, particle size distribution, PSD. 37

Table 5 - Cutting parameters combinations used in milling tests (3 parameters x 3 levels). 44

Table 6 - Swift-Voce equation parameters for hardening curves of the AM material. 45

Table 7 - Material properties of AM 18Ni300 used in the numerical model of Silva [82]. 45

Table 8 - Chemical composition (wt%) of 18Ni300 steels with respective reference values. 48

Table 9 - Roughness measurements averages (x) and standard deviation (σ) of Ra, Rz, and Rz max parameters in as-built AM condition and CM after grinding (values in μm). 50

Table 10 - Hardness measurements (HV) of 18Ni300 steel in both CM and AM metallurgical conditions 51

Abbreviations

ALE	arbitrary Lagrangian-Eulerian
AM	additive manufacturing/manufactured
AMG	automatic mesh generation
BUE	built-up edge
CEL	coupled Lagrangian-Eulerian
CFD	computational fluid dynamics
CM	conventional manufacturing/manufactured
CNC	computer numerical control
CNEM	constrained natural element method
CPU	central processing unit
DED	direct laser deposition
E-PBF	electron beam-based powder bed fusion
EDM	electrical discharge machining
EDS	dispersive x-ray spectroscopy
EXP	experimental
FEM	finite element method
HAZ	heat affected zone
L-PBF	laser-based powder bed fusion
MAM	metal additive manufacturing
PBF	powder bed fusion
PSD	particle size distribution
PVD	physical vapor deposition
RCD	rotating cutting force dynamometer
SEM	scanning electron microscope
SLM	selective laser melting
SPH	smooth particle hydrodynamics

Symbols

A_C	uncut chip cross section area
A_S	shear plane area
C	workpiece material constant
E	Young's modulus
F_c	cutting force
F_F	force along the tool face
F_N	force normal to the tool face
F_S	force along the shear plane
F_{SN}	force normal to the shear plane
F_t	force normal to the cutting force
F_z	force on the z-axis
G_f	fracture energy
K_c	specific cutting pressure
P_L	laser power
R	resultant force
c_p	specific heat
d_s	layer thickness
h_s	hatch spacing
k	workpiece material shear strength
l	distance
l_C	sticking distance
m, n	correction factor
t_0	uncut chip thickness
t_c	chip thickness
v_s	scan speed
$\bar{x}$	average

Greek letters

α	clearance angle
α_{inst}	thermal expansion coefficient
β	wedge angle
ε_P	true strain
ϕ	shear angle
μ	friction coefficient
ρ	mean angle of friction between chip and tool
σ	normal stress
τ	shear stress
τ_0	pure shear
τ_S	shear strength
λ	conductivity
γ	rake angle

1. Introduction

1.1. Motivation and context

Additive manufacturing (AM) technology has been a leading edge technology in the new industrial revolution (Industry 4.0), enabling the production of near net-shape components with high design freedom. Advantages have been recognized in these processes in terms of complex parts feasibility, which can be highly complex or even impossible through conventional processes. In addition, the production of parts without the need for tools such as moulds and dies may reduce the necessary costs for the rapid production of small series, which has attracted many areas of industry. Although not new, new light has been shed over topology optimization and its enhanced viability with additive manufacturing, which has been employed in areas such as aerospace, aeronautics, motorsport, as shown in Figure 1, among others [1].

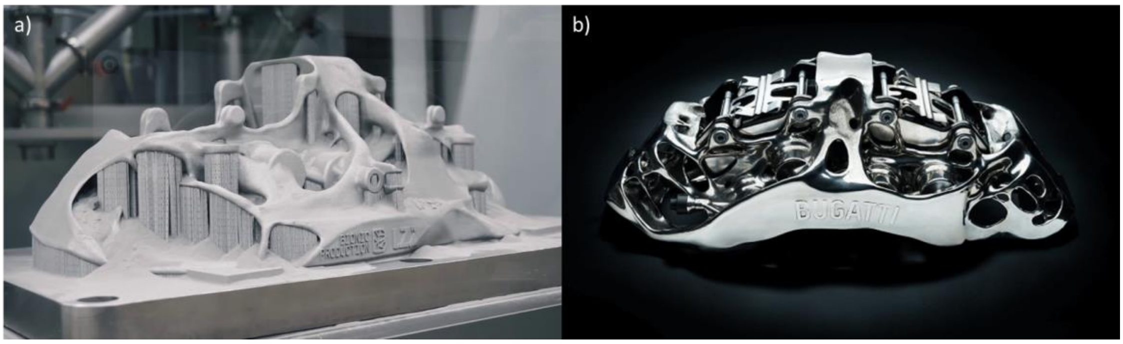

Figure 1 - Additive manufacturing (powder bed fusion) and topological optimization of a Bugatti brake caliper: a) building process, b) final component [2].

The requirement for high quality surface roughness as well as tight geometrical and dimensional tolerances bring into focus the need for post processing of additively manufactured parts in order to be successfully integrated into functional assemblies. Regarding this fact, the machinability assessment and evaluation of additive manufactured (AM) parts need to be studied, since important aspects such as the anisotropic structure, microstructure, and residual stresses are distinct from components produced by conventional processes which, in turn, may lead to a different behaviour when subjected to machining operations. The importance of an appropriate choice of cutting parameters in order to achieve the high requirements is also highlighted.

The present dissertation integrates the MAMtool research project, which focuses on the machinability and need for post-processing of metal components produced by the additive manufacturing process powder bed fusion, in particular, the 18Ni300 maraging steel. In the plastic injection moulding industry, maraging steel is used for the production of additive AM mould inserts with conformal cooling channels [3]. The better control of the cooling channels position (following the geometrical features of the mould) allows for a more efficient and faster heat dissipation from the mould, when compared to straight line perforated channels, as shown in Figure 2. The reduction of injection time and consequent higher productivity also represent a great advantage, capable of large cost reductions when applied to large series. The assembly of the components of a mould requires high precision and tight dimensional tolerances. As main results of this work, it is expected an analysis of the loads in cutting, chips, quality, and integrity of machined surfaces.

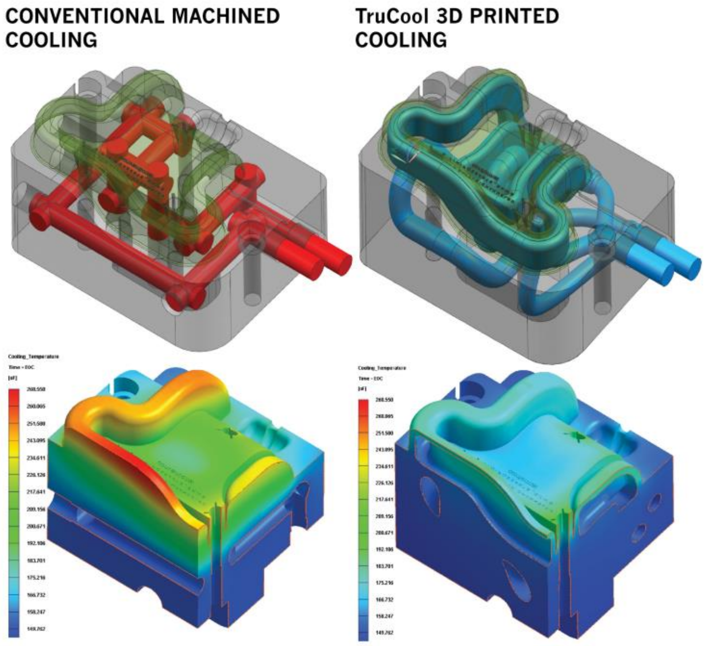

Figure 2 - Temperature distribution on plastic injection mould insert using conventional drilled and additively manufactured conformal cooling channels [4].

1.2. Goals

The machinability of AM metals still presents many challenges concerning their characterisation and improvement. This dissertation aims to study the machinability of both additively and conventionally manufactured 18Ni300 maraging steel. To achieve this, a set of multidisciplinary and ordered objectives has been established:

1. Comprehensive literature review on the topics of cutting fundamentals, analytical and numerical modelling, with focus on metal machining, as well as additive manufacturing, in particular powder bed fusion. State of the art on machinability of metals produced by additive manufacturing, in particular 18Ni300 maraging steel;
2. Characterisation of the as-received two different materials by analysis of roughness, hardness, density and microstructure;

3. Machinability analysis of the selected steels through instrumented milling tests with analysis of the cutting loads involved, as well as of the roughness, hardness, chip morphology and residual stresses obtained on the specimens;
4. Definition of a constitutive model of additive manufactured 18Ni300 maraging steel for 3D simulation of the milling process.

1.3. Thesis structure

This dissertation is divided into 4 main chapters, each of which is briefly described below:

1. **Introduction:** In this section the subject of the thesis is presented, as well as its motivation and context. Furthermore, main objectives are defined aiming towards machinability characterisation of 18Ni300 maraging steel.
2. **Literature review:** In this chapter a literature review is carried out on the theory of metal cutting. The analytical models used to describe the machining processes are documented, serving as a bridge to the more complex numerical models, which are also analysed, in what regards material modelling (plasticity and damage), cutting temperature distribution and chip formation. Furthermore, the metal additive manufacturing processes are briefly reviewed, focusing mainly on the powder bed fusion process. The influence that the process parameters have on the final characteristics of the parts is also lightly addressed, always emphasizing on 18Ni300 maraging steel. A state of the art on machinability studies of metals produced by additive manufacturing, in particular 18Ni300 maraging steel, is made. Innovative technologies such as hybrid manufacturing are also addressed due to the convenient combination of additive manufacturing with conventional machining.
3. **Experimental and simulation procedures:** The third chapter describes the whole experimental process from material characterisation to the experimental milling campaign performed. The analyses of hardness, roughness, density, residual stress, and microstructure are described. In addition, the numerical model definition is detailed.
4. **Experimental and numerical results:** The results of each characterisation procedure described in the previous chapter are discussed in this section. A detailed machinability analysis of the steels considered is performed, comparing the two materials and when possible, with the literature. Furthermore, the results of the numerical milling simulations are analysed and compared with the experimental data obtained.

2. Literature review

In this section, a review of cutting processes is made, starting with the basics of orthogonal cutting, which serves as a starting point for the understanding of analytical models that try to replicate the cutting mechanisms. Analytical models serve as a bridge to numerical models, commonly used for the simulation of cutting processes, which are also documented. Then a brief review of the metallic additive manufacturing processes is presented, with special attention to the powder bed fusion process and the influence of the parameters of this process on the characteristics of the obtained parts. Finally, the state of the art of machining operations in materials produced by additive manufacturing, especially 18Ni300 maraging steel, is documented.

2.1. Metal cutting

In this chapter, the mechanisms of metal cutting, such as chip formation and the involved forces will be analysed, with an emphasis on the milling process. This will be followed by the review of analytical models that have been used over the years to describe the process and which today are still seen as a bridge to numerical simulation. Finally, the techniques and numerical models used today that allow a better approximation of the real conditions will be addressed.

2.1.1. Mechanics of metal cutting

In the cutting processes, a cutting tool is used to remove excess material from a workpiece in order to achieve the desired shape. A chip is formed by shear deformation of the work material and an approximation of the final shape is done removing successively chips. Machining processes are usually applied to a wide range of materials (i.e metals, polymers, composites) and although the use of unconventional manufacturing processes is increasing nowadays, the conventional metal cutting processes (refer to Figure 3) continue to represent a substantial role in the industry. This is especially relevant since the characteristic geometric features, dimensional accuracy and good surface quality are difficult to obtain by other processes [5].

The study of metal cutting mechanisms is of tremendous importance since the prediction and optimization of these processes may represent significant economic benefits. Despite the large amount of industrial machining operations, a simplified cutting model, the orthogonal cutting, is still widely used to analyse the influence of the cutting parameters in the processes performance.

As a relatively good option to predict the mechanisms in cutting processes, orthogonal cutting continues as a fundamental basis to numerical models.

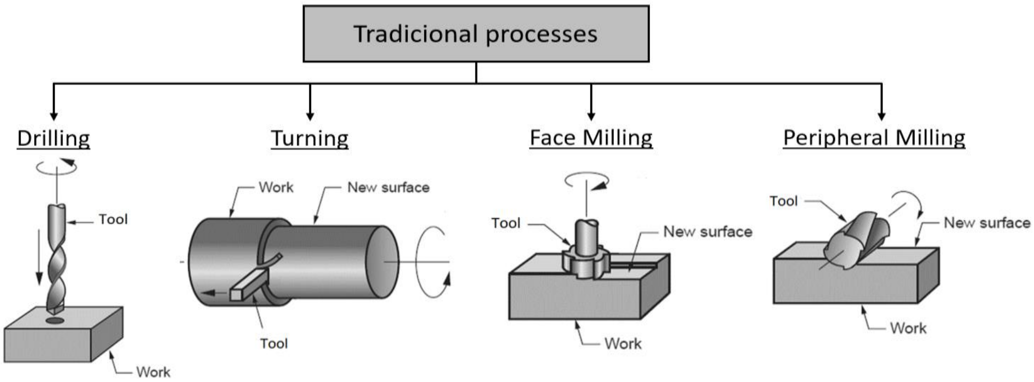

Figure 3 - Most common conventional machining processes: drilling, turning, face milling, peripheral milling, adapted from [5].

2.1.1.1. Orthogonal cutting

In conventional machining processes, although the chips may flow in an arbitrary direction relative to the cutting edge, it could be generally considered that, at each point of the cutting edge, there are conditions of oblique cutting, in other words, the orientation of the cutting edge is oblique to the direction of the cutting movement of the tool. A simplification of the cutting process is orthogonal cutting, where the effective cutting direction is perpendicular to the cutting edge (refer to Figure 4), and the chip is under a planar shear deformation, allowing the model to be bidimensional, which simplifies the analysis [6, 7].

The tool (wedge shape and straight cutting edge) consists of two surfaces: (i) the rake face, the one along which the chip flows; (ii) the flank, which provides a small clearance between the new machined surface and the tool, while maintaining its robustness. The basic geometry of the tool and the cutting process is defined by the angles between these surfaces. As illustrated in Figure 5, the rake angle, γ, is the angle between the rake face and a line perpendicular to the machined surface. On the other side, the angle between the flank and the new machined surface is called clearance angle, α. Finally, the angle between the two tool surfaces is the wedge angle, β, and the sum of these three angles is always equal to 90º, as it could be seen in Figure 5 [8].

As the tool is forced into the material, the tool's cutting edge plastically deforms the workpiece, promoting shear deformation along a plane oriented at an angle ϕ, with the surface of the work, called the shear plane, forming a chip [5].

Although the orthogonal cut is a simplification of the cutting process, it is a bridge to extrapolate to more general and real cutting situations. Still, the oblique cutting represents a more realistic version of the orthogonal cutting model, as it is similar to the more common three-dimensional machining processes [6].

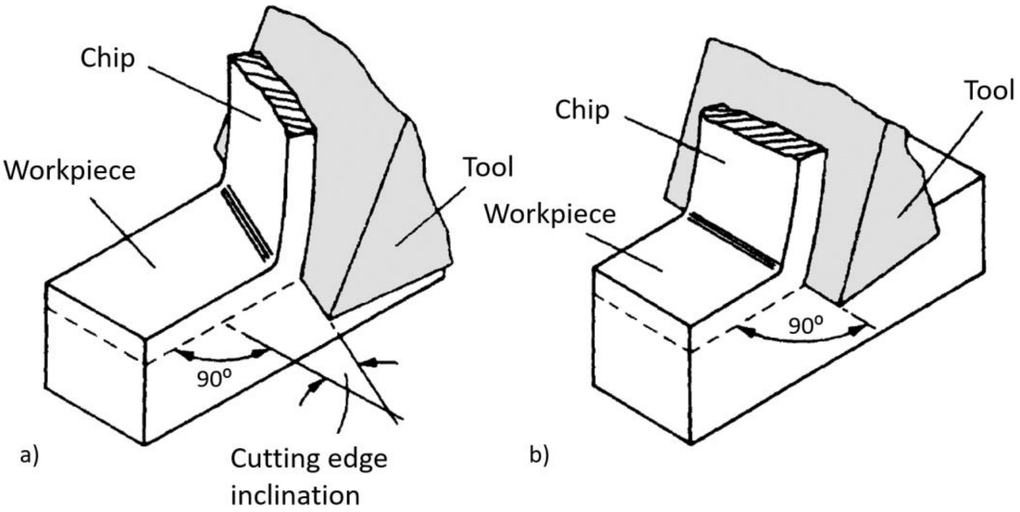

Figure 4 - Simplification of the cutting phenomena: a) Oblique cutting; b) orthogonal cutting, adapted from [7].

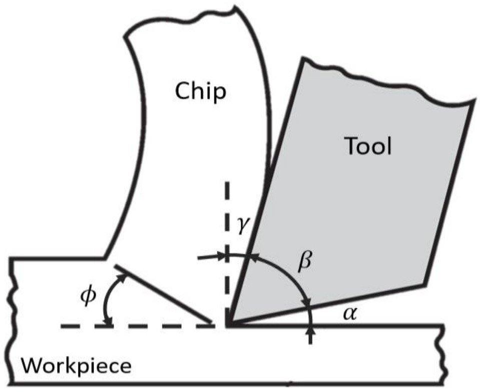

Figure 5 - Main angles in orthogonal cutting: rake angle, γ, clearance angle, a, wedge angle, β, shear angle, ϕ, adapted from [5].

2.1.1.2. Chip formation

As mentioned before, there is intense plastic deformation during the chip formation process, and three zones of the cutting process could be identified, as seen in Figure 6. The first zone (primary shear zone), which defines the so-called cutting plane, is located at the base of the chip, where intense plastic deformations, shear, and compression stresses, are dominant. The compression stresses are responsible for the increased chip thickness, t_c, when compared to uncut chip thickness, t_0[5, 6]. The secondary shear zone results from the contact between the chip and the tool. The high friction and contact pressures between the two parts cause intense plastic shear deformation in the lower part of the rake face. The higher is the friction coefficient and pressure, the higher will be the deformation in the chip [6, 8]. Although in theory, with positive clearance angles, the tool flank face only contacts the new generated surface in the cutting edge, in reality there is always part of the flank face that contacts the workpiece. The tertiary shear zone is caused by the friction between the flank and the new generated surface [6].

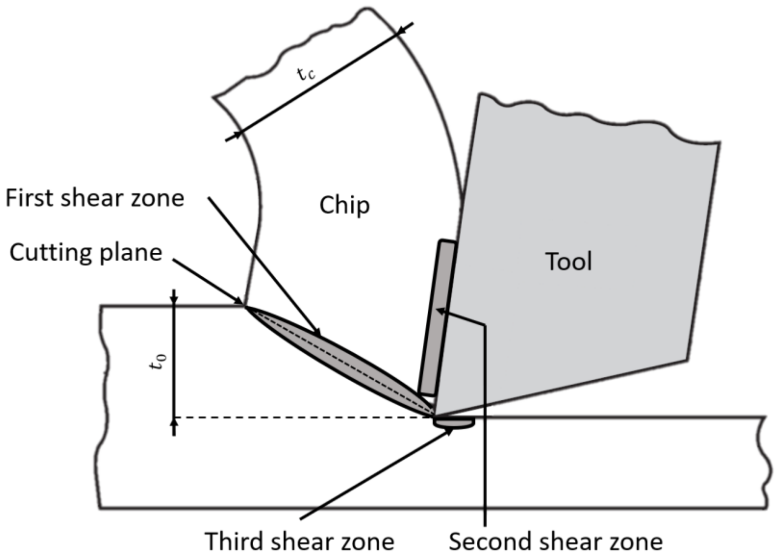

Figure 6 - Shear zones in chip formation, adapted from [5]

Depending on the deformation behaviour of the workpiece material and the cutting conditions, the resultant chip from metal cutting process could be very different. Some different classifications have been developed over the years. However, all aim to describe the different mechanisms from a continuous chip to a totally discontinuous chip. It is possible to divide metal chips in three main categories: continuous chips, semicontinuous or serrated chips, and discontinuous chips, as shown in Figure 7 [5].

When ductile materials are machined with high cutting speeds, the chip slide along the tool in a stationary flow. This is promoted not only by the sharp cutting edges and low tool-chip friction, but also positive rake angles and low undeformed chip thickness [9]. The long chips formed by this continuous flow could damage the new surface and cause problems in the equipment when wrapped around the tool. In order to overcome this problem and maintain the good surface quality generated by the stationary flow, a chip-breaker (refer to Figure 8) could be used to break the chip in segments. When ductile materials are machined with low cutting speeds, portions of work material tend to adhere to the rake face of the tool near the cutting edge, called built-up edge (BUE), derived from friction between tool and chip. This type of chip could be considered a subtype of the continuous chip. The formation of BUE has an important role in tool life and in surface quality of the process. Although it may offer protection on the rake face, it can also cause premature wear on the tool and inevitably increases the surface roughness in the new surface [5]. On the other hand, when brittle materials are machined at low cutting speeds, discontinuous chips are generated. In contrast to continuous chips formation, high tool-chip friction and large feed and depth of cut contribute to its occurrence. The new surface is produced by the chip break-out rather than by the tool itself [5].

Finally, serrated chips are often resultant from difficult-to-cut metals, particularly for high cutting speeds. The name reflects the saw-tooth appearance, produced by a cyclical chip formation of alternating high shear strain followed by low shear strain. Although this chip formation mechanism is associated with certain difficult-to-cut materials, such as titanium alloys and nickel-base superalloys, serrated chips could also occur when machining common work metals at high speeds [5, 6].

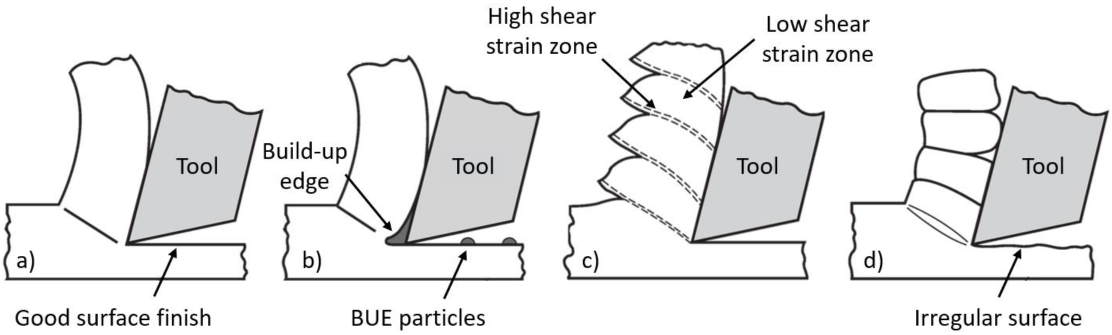

Figure 7 - Most common chip formation mechanisms: a) Continuous chips; b) continuous chips with BUE; c) serrated chips; d) discontinuous chips, adapted from [5].

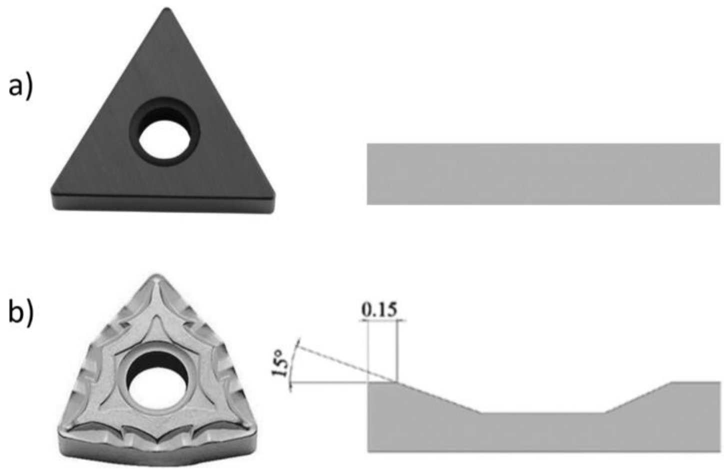

Figure 8 - Cutting insert for turning operations showing cutting edge and rake cross-section: a) without and b) with chip breaker, adapted from [10].

2.1.2. Milling

Milling is one of the traditional machining processes, where the axis of rotation of the cutting tool is perpendicular to the direction of feed. The process incorporates a feed motion, that can be performed by the tool, the workpiece or by a combined movement of the two, and a rotational cutting motion of the tool [5]. There are two major types of milling: peripheral milling, where the axis of the tool is parallel to the surface being machined and face milling, where the axis of the cutter is perpendicular to the surface being milled [11]. However, there are several varieties of these two categories which can be divided in accordance with other criteria, as shown in Figure 9.

Also important to note in the kinematics of the milling process is the feed direction angle φ (refer to Figure 11). When the cutting edge of the milling cutter enter the workpiece at the maximum undeformed chip thickness (refer to Figure 10), the process could be called down-milling. On the other side, if the cutting edge enters at the theoretical minimum undeformed chip thickness (h = 0), the process could be called up-milling. Some milling operations (i.e. slot milling) may include both processes [11].

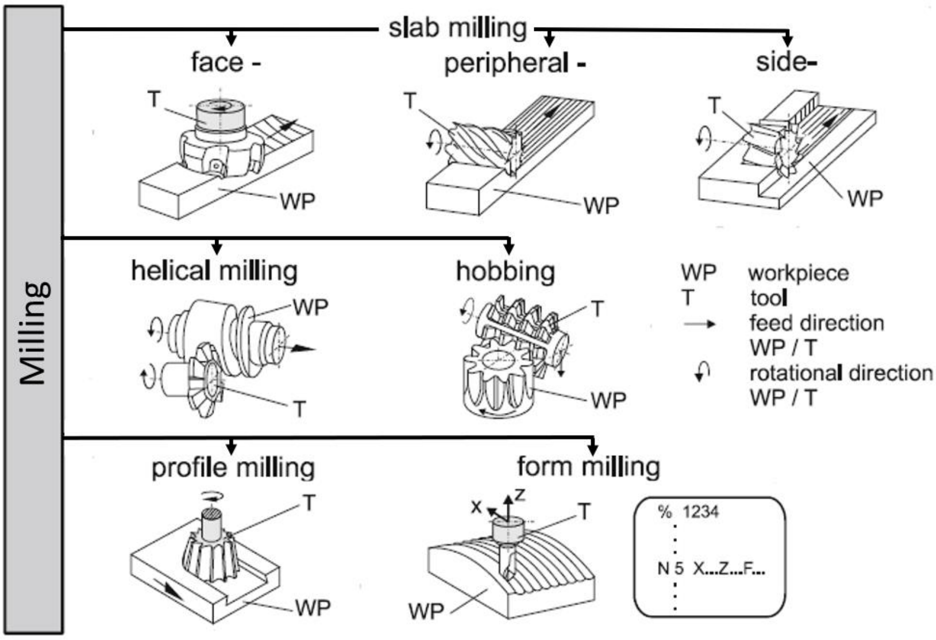

Figure 9 - Milling processes, adapted from [9].

The process can be described by cutting parameters as the cutting speed v_c, the feed of the cutting edge f_z, which is measured in the feed direction, the depth of cut a_p, measured parallel to the tool axis, and finally the cutting engagement a_e, measured perpendicularly to the feed direction and tool axis simultaneously [11].

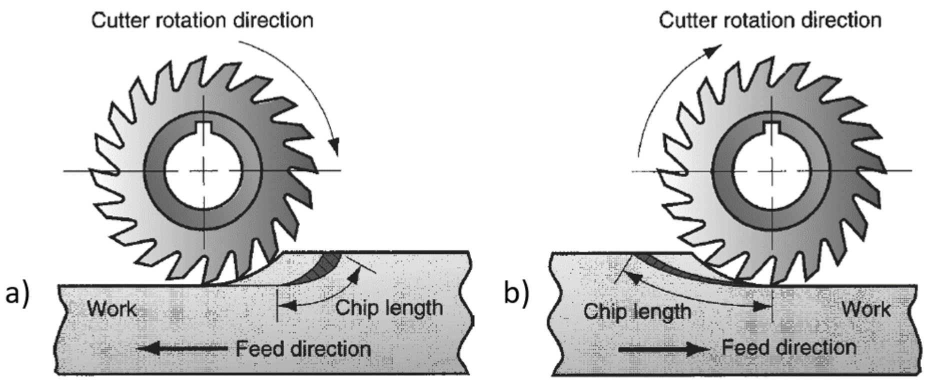

Figure 10 - a) Down-milling; b) Up-milling, adapted from [5].

During the cutting process, the milling tool edges are constantly being engaged, one after the other, leading to an interrupted cut, with a maximum tool engagement of 180º. The cutting edges describe cycloid trajectories in relation to the workpiece and as the feed velocity is significantly lower than the feed velocity, they can be approximated by circular paths. Due to the cycloid movement of the cutting edge, comma-shaped chips are generated, as shown in Figure 11 [9, 11].

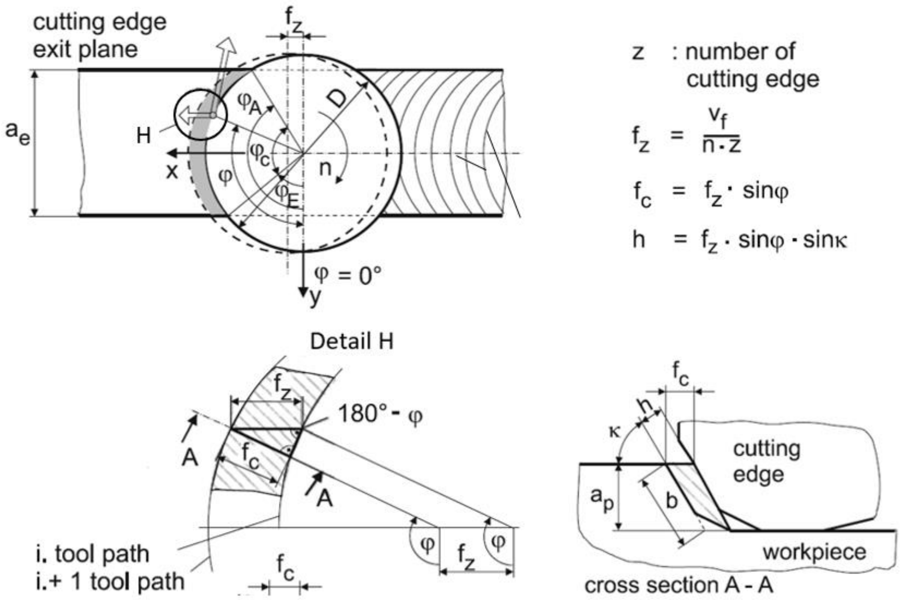

Figure 11 - Tool-workpiece engagement parameters in plain face milling, adapted from [9].

Due to the complexity of the milling process, some authors try to model the process by employing the orthogonal cutting [12, 13], using simplifications. To fully characterise the process, an average chip thickness, h_m, is often calculated in function of the engagement path, as shown in Equation (2.1).

$$h_m = \frac{1}{\varphi_c}\int_{\varphi_E}^{\varphi_A} h(\varphi)d\varphi = \frac{1}{\varphi_c} f_z \sin k \,(\cos\varphi_E - \cos\varphi_A) \tag{2.1}$$

Regarding the cutting forces, the active machining force F_a can be resolved in two components in relation to the direction of cutting speed, assuming a tool rotating referential: the cutting force, F_c, and the force perpendicular to the former, F_{cN}, that are related with the tool. On the other hand, related to the workpiece, the active force could be resolved in the feed force, F_t, and the force perpendicular to the feed force, F_{fN}, assuming a fixed referential (refer to Figure 12 a)). As the cutting edge is changing constantly, with the entry angle φ, the direction of the active force is also changing [11].

As the direction of cutting forces change with the engagement angle, the components of the active force oscillate in sinusoidal pattern for plain face milling with an end milling cutter, as shown in Figure 12 b) [11].

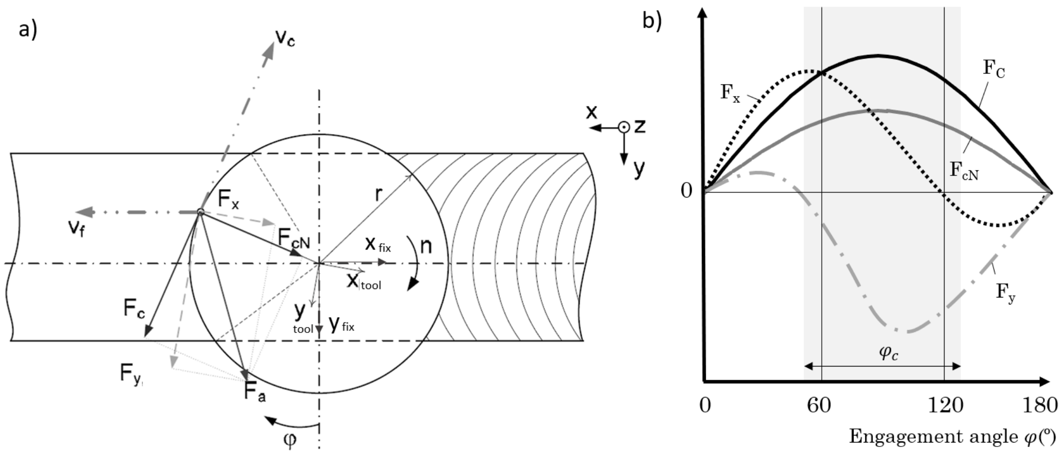

Figure 12 - a) Components of milling cutting forces, b) Cutting force components evolution during engagement, adapted from [11].

2.1.3. Analytical models

Throughout the years, many efforts have been made in order to specify the forces involved in cutting processes. The use of analytical models emerged as a necessity for the determination of these forces and are based on basic material properties and their plastic behaviour. These approaches do not actually provide exact descriptions of forces, however, they allow relevant input and process parameters and their interdependencies to be described. Although analytical models could be considered as predecessors of numerical models, they are still often employed given their simplicity and cost-effectiveness [8, 9].

2.1.3.1. Primary deformation zone analytical modelling

The determination of cutting forces emerge as the focus of most analytical models, as with these, it is possible to obtain values of parameters such as tool wear, surface integrity and workpiece quality. The relation between the shear angle, the rake angle and the friction coefficient is normally the key for these models. There are some distinct approaches that could be classified into three many categories: single shear plane (a), slip line field (b) and shear zone (c), as shown in Figure 13.

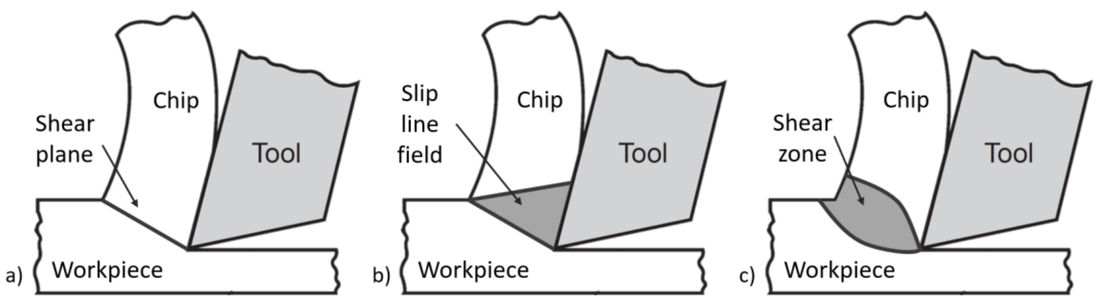

Figure 13 - Analytical models: a) shear plane model, b) slip line field model, c) shear zone model, adapted from [5].

The shear plane model is the most commonly used model to predict the forces during cutting. Although Piispanen attempted to establish a theorical law that predicts the shear angle in 1937, the first complete solution was presented by Ernst and Merchant [14], which is still the most popular approach. The chip was assumed to behave as a rigid body, being in equilibrium by the action of the forces transmitted across the chip-tool interface, where the Amonton's friction law is applied, and across the shear plane [7]. The model assumes that the deformation would be two-dimensional (orthogonal cutting), and the resultant force would be transmitted to the cutting edge on a linear contact orthogonal to the working plane. In addition, the deformation would only take place in the shear plane, where the stress is constant [9].

In Figure 14, for simplification purposes, all forces are shown acting at the tool tip. The resultant force, R, could be resolved in components F_N and F_F that are normal to and along the tool face, respectively. F_{SN} and F_S, that are normal to and along the shear plane, can also be result of R. Finally, it could also be resolved into components F_C, the cutting force, and F_t the force normal to the cutting force. The shear angle ϕ, the rake angle γ and the mean angle of friction between chip and tool ρ are also shown.

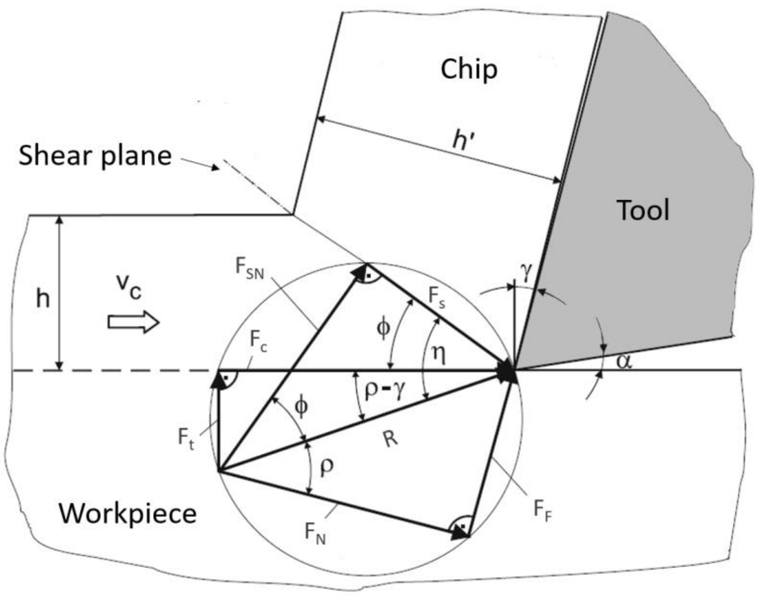

Figure 14 - Force diagram in orthogonal cutting, adapted from [9].

As the cutting force, F_C, is proportional to the cutting work, an expression of F_C with the shear angle, ϕ, needs to be found and then obtain the ϕ for which F_C is a minimum. From Figure 14, the relation shown in Equation (2.2) could be concluded [8]:

$$F_S = R \cdot \cos(\phi + \rho - \gamma) \quad (2.2)$$

Where:

Fs is the force along the shear plane;
R is the resultant force;
Φ is the shear angle
ρ is mean angle of friction between chip and tool;
γ is the rake angle.

The force along the shear plane could also be calculated by the product of the shear strength of the workpiece material on the shear plane, τ_S, by the cross-sectional area of the shear plane, A_S, as shown in Equation (2.3):

$$F_S = \tau_S A_S = \frac{\tau_S A_C}{\sin\phi} \tag{2.3}$$

Where:

A_C is the uncut chip cross section area.

With Equations (2.2) and (2.3), it is possible to rearrange R, as shown in Equation (2.4):

$$R = \frac{\tau_S A_C}{\sin\phi} \cdot \frac{1}{\cos(\phi + \rho - \gamma)} \tag{2.4}$$

It can be geometrically deducted that (Equation (2.5)):

$$F_C = R \cdot \cos(\rho - \gamma) \tag{2.5}$$

Where:

F_C is the cutting force.

From Equations (2.4) and (2.5), F_C can also be obtained in function of ϕ, as shown in Equation (2.6).

$$F_C = \frac{\tau_S A_C}{\sin\phi} \cdot \frac{\cos(\rho - \gamma)}{\cos(\phi + \rho - \gamma)} \tag{2.6}$$

If Equation (2.6) is differentiated with respect to shear angle ϕ and equated to zero, it is possible to obtain the shear angle for which the cutting force is minimum, as shown in Equation (2.7).

$$\phi = \frac{\pi}{4} - \frac{\rho}{2} + \frac{\gamma}{2} \tag{2.7}$$

This equation did not correspond well with experimental results of metal machining as it was assumed that A_C, γ and τ_S were independent of ϕ, as stated by Markopoulos [8]. In a revised theory, deformation and friction are reflected through a change of the force acting in the direction perpendicular to the plane of shear, thus the normal stress, σ_S, of the shear plane affects the shear stress, τ_S, resulting in Equation (2.8) [8].

$$\tau_S = \tau_o + k\sigma_S \tag{2.8}$$

Where:

τ_o is pure shear;
k is slope of the $\tau - \sigma$ relation.

The shear stress increases linearly with an increase in normal strength which is known as the Bridgman relation [8]. The revised theory presents the following relation, Equation (2.9), for the shear angle, where C is a constant that depends on the workpiece material.

$$\phi = C - \frac{\rho}{2} + \frac{\gamma}{2} \qquad (2.9)$$

Despite the popularity of the shear plane model, it presents some limitations as it is based on restrictive material assumptions, more specifically, the assumption that the deformation occurs on a single plane, which results in a velocity discontinuity along which the strain rate is infinite. In addition, the constant friction coefficient characterisation of the rake face is not consistent with experimental data [15].

Regarding the slip line field models, the model proposed by Lee and Shaffer [16] is the most popular one (refer to Figure 15). The model defines the triangular region ABC as an area where the material is stressed. All deformations are supposed to occur on a plane inclined at an angle ϕ with respect to the plane of cut. In equilibrium, the angle ACB could be shown as equal to 45º, which results in the shear angle been given by Equation (2.10). For ϕ = 0, a different solution is proposed, which assume the formation of built-up edge [15].

$$\phi = \frac{\pi}{4} - \rho + \alpha \qquad (2.10)$$

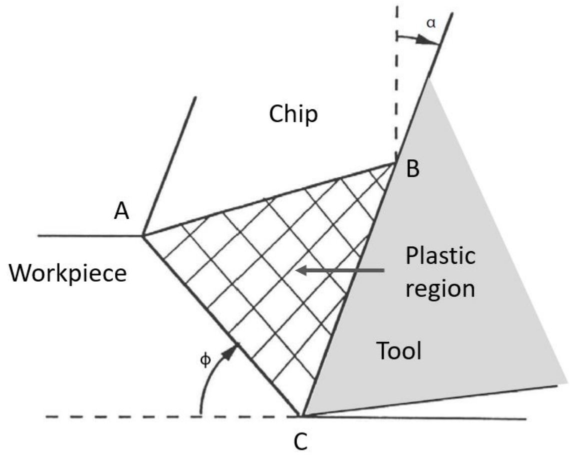

Figure 15 - Lee and Shaffer's slip-line field solution for orthogonal cutting, adapted from [15].

The third approach, the shear zone model, attempts to achieve a more realistic characterisation of cutting. The Oxley's theory [17] is the best-known shear zone model, and its intricate analysis includes a procedure to determine the chip thickness and tool-chip contact length, and rather than a plane, a shearing region is assumed in workpiece deformation, where strain hardening is considered.

Shear zone models are complex and require specialized material test data and substantial computer code development for application and for these reasons, their application outside of the research community as not been largely explored. Experimental data support the Oxley's model, especially when modifications are made to include a larger range of material models. Models as the Oxley model include temperature effects, allowing the investigation of tool wear and shear localized chip formation, which cannot be studied using simpler approaches [8, 15].

Markopoulos [8] and Silva [18] have compiled some of the most important analytical models used to date, as could be seen in Table 1.

Table 1 - Shear angle analytical model according to different authors, adapted from [8, 18].

Author (Year)	Model formula	Eq.
Ernst-Merchant (1941)	$\phi = \frac{\pi}{4} - \frac{\rho}{2} + \frac{\gamma}{2}$	(2.11)
Merchant (1945)	$\phi = C - \frac{\rho}{2} + \frac{\gamma}{2}$	(2.12)
Stabler (1951)	$\phi = \frac{\pi}{4} - \rho + \frac{\gamma}{2}$	(2.13)
Lee-Shaffer (1951)	$\phi = \frac{\pi}{4} - \rho + \gamma$	(2.14)
Shaw et al. (1953)	$\phi = \left(\frac{\pi}{4} + \eta'\right)(\rho - \gamma)$	(2.15)
Zorev (1958)	$\phi = \cot K\phi - \tan(K\phi + \rho - \gamma) = \cot\phi + \tan(\rho - \gamma)$	(2.16)
Oxley (1961)	$\phi = \arctan\left[1 + \frac{\pi}{2} - 2\phi + \frac{\cos 2(\phi - \gamma)}{\tan\rho} - \sin 2(\phi - \gamma)\right] - (\rho - \gamma)$	(2.17)
Sata and Yoshikawa (1963)	$\phi = \operatorname{arccot}\left[\cot\theta + \frac{\cos\theta}{\sin(\theta + \gamma)kL}\right]$	(2.18)
Atkins (2003)	$\phi = \left[1 - \frac{\sin\rho\sin\phi}{\cos(\rho - \gamma)\cos(\phi - \gamma)}\right]\left[\frac{1}{\cos^2(\phi - \gamma)} - \frac{1}{\sin^2\phi}\right]$	(2.19)

2.1.3.2. Friction modelling

The modelling of the friction between the tool and the chip is of utmost importance since it has great influence on the forces and temperatures registered during the cutting process. In addition, wear and tool life may also be accurately estimated if friction conditions are correctly characterised. Although it is an area in cutting of great importance, the truth is that it is still a phenomenon not fully known and consequently, it is difficult to model. Some simple models have been proposed during the years.

In 1699, Amontons stated that friction was independent of the apparent area of contact and proportional to the normal load between two surfaces. In 1785, Coulomb verified these laws and showed that the coefficient of friction was substantially independent of the speed of the sliding. Many machining finite element models assume this classical view. In the Coulomb's law, presented in Equation (2.20), the frictional sliding force is proportional to the applied normal load and the ratio between these is the coefficient of friction μ, which is constant in all the contact length between chip and tool [8].

$$\tau = \mu\sigma \tag{2.20}$$

Where:

τ is the shear stress;

σ is the normal stress.

Despite its popularity, the Coulomb's law fails to give accurate predictions, as the normal stresses increase and surpass a critical value. Zorev [19] proposed other model, where two contact regions may be distinguished in dry machining, namely the sticking and the sliding region. In the first region, near the tool cutting edge and up to a distance l_C, the shear stress is equal to the shear strength of the workpiece material, k, and in the sliding region, the friction is described by the Coulomb's law, as shown in Equation (2.21).

$$\tau = \begin{cases} k, & 0 \leq l \leq l_c \\ \mu\sigma, & l > l_c \end{cases} \tag{2.21}$$

The work of Zorev was studied and redefined by other researchers such as Usui and Childs [20, 21]. Usui [20] proposed a non-linear model (Equation (2.22)) which approaches the sticking region of the Zorev model for large stresses and the sliding part for smaller stresses.

$$\tau = k\left(1 - e^{-\frac{\mu\sigma}{k}}\right) \tag{2.22}$$

Based on the Usui model, Childs [21] proposed another model which incorporates correction factors (m and n) to regulate the transition from sticking to sliding region (n) and to ensure that at high normal stresses the frictional stresses do not exceed k, as shown in Equation (2.23).

$$\tau = mk\left(1 - e^{\left(-\frac{\mu\sigma}{mk}\right)^n}\right)^{1/n} \tag{2.23}$$

Research in the contact area has continued over the years and a number of other models have been proposed. Some researchers have studied de influence of these models in the results of machining simulations. Özel [22] compared some different models and not only concluded that the models have a significant influence in the predicting of chip geometry, forces, stresses on the tool and the temperatures at the tool-chip interface, but also that the most accurate results were achieved when the friction models were based on the measured normal and frictional stresses on the tool rake face and when implemented as variable friction models at the tool-chip contact in the simulations. However, in the study of Filice et al. [23], five different friction models were analysed and apart from small differences, the main mechanical results as forces and contact length, were practically not sensitive to the friction model.

Arrazola and Özel [24] studied the influence of the boundary conditions and the finite element method (FEM) formulations. It was concluded that in finite element simulations of chip formation processes, in order to predict forces, stresses, and temperatures more accurately, stick–slip friction models should be used with caution and limiting shear stress values must be determined for each cutting condition.

2.1.4. Numerical modelling

Numerical simulation inevitably arises to bring modelling closer to reality. As mentioned before, the metal cutting processes incorporate intense deformations, involving large strains, high strain rates, high stresses, and elevated temperatures. To account for these extreme conditions, the material models must have the capability to portray this variety of situations, often in operations that cannot be simplified by continuous regimes. Hence, adequately selecting the constitutive equation and its calibration method constitute a challenge.

2.1.4.1. Numerical formulations

Regarding mathematical formulations of continuum-based FEM, it is possible to identify two major ones: Eulerian and Lagrangian. In both analyses, either implicit or explicit time integration techniques can be utilized. In the Eulerian formulation, a fixed mesh in space is used, which functions as a control volume. This analysis is more compatible with continuous regimes and is standard for Computational Fluid Dynamics (CFD) analysis. In machining simulations, it has the advantage of being able to deal with large deformations without a large increase in computational cost. Despite that fact, it is necessary to define the geometry of the chip a priori, which makes it impossible to analyse the influence of the cutting parameters on its morphology [8, 25].

The Lagrangian formulation uses a mesh that deforms in time with the material. The separation of the undeformed chip from the workpiece could be perform with automatic remeshing or with element deletion criteria. As the deformations in cutting are very high, mesh regeneration is used to smooth distortions, and avoid using a damage models, however, it represents a cost of an increased central processing unit (CPU) time and the need for refined meshes to reduce the errors of the approximations made when transferring values between different meshes. These approaches enable the analysis of chip morphology without the need for a predefined geometry. Thus, many researchers have adopted the computationally intensive Lagrangian approach [25, 26].

In order to combine the advantages of both formulations, hybrid solutions have been developed, of which Arbitrary Lagrangian-Eulerian (ALE) and Coupled Lagrangian-Eulerian (CEL) could be highlighted. The former adopts an explicit solution technique for fast convergence. This method allows the arbitrary characterisation of boundary conditions, choosing purely Lagrangian, Eulerian or a combination of both in order to optimize the simulation. In the CEL approach, for the tool is assumed a Lagrangian formulation as opposed to workpiece where a Eulerian formulation is used [25, 26].

Although FEM methods have been much more widely used, there are other methods, based on conservation of mass, momentum, and energy. Meshless techniques are included in this, where material properties and state variables are approximated by their values at a set of discrete points, or particles. The Constrained Natural Element Method (CNEM) and Smooth Particle Hydrodynamics (SPH) are examples of these methods. These techniques have some advantages because there is no need for a mesh of elements and so remeshing, mesh distortion, separation criteria problems are avoided [24, 25].

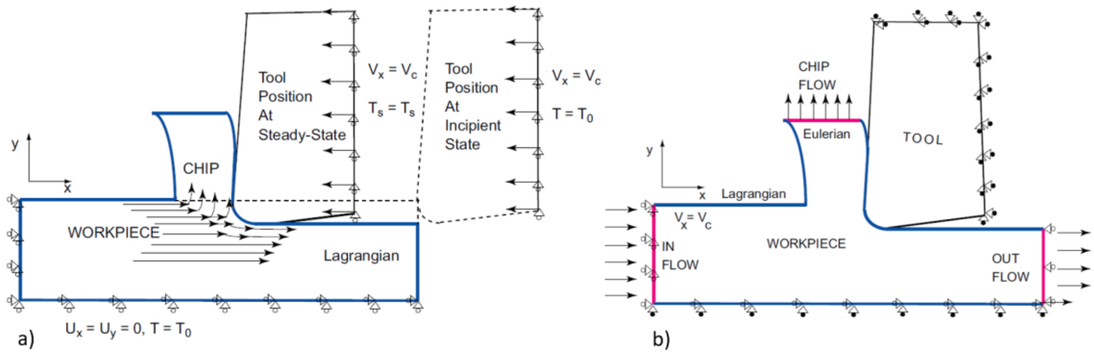

Figure 16 - ALE scheme models with different boundary conditions: a) pure Lagrangian boundary conditions; b) pure Eulerian boundary conditions, adapted from [24].

2.1.4.2. Material modelling

The modelling of the material behaviour is of great importance in machining since it aims to describe the material response to different mechanical and/or thermal loading conditions, based on stress-strain governing equations, together with the conservation laws and kinematic relations. In the literature, constitutive models could be mainly classified regarding their field of application as elastic-plastic, elastic-viscoplastic, rigid-plastic, and rigid-viscoplastic and in relation to their method of derivation and identification of constants as empirical, semi-empirical and physics-based models [8, 27].

Physics-based constitutive equations are solely based on physical theory. These models are not widely used since a larger number of constants are involved and their determination require precisely controlled experiments.

Despite the complexity of the experimental plastic behaviour of engineering materials, some simple models have been used over the years to simplify the characterisation of the cutting process. In the elastic-work-hardening idealization after the yield point, the stress continues to rise with strain increments that could be modelled by material hardening functions (refer to Figure 17). In the literature, several models have been proposed for the material hardening deformation. The simplest models, also called strain rate-independent plastic models, assume that stress is only a function of the strain and not of the strain rate, such as the Hollomon's law (Equation (2.24)), which does not fit the stress–strain relationship at low strains [8, 28, 29]:

$$\sigma = K(\varepsilon_P)^n \tag{2.24}$$

Where:

σ is the true stress;
K and n are experimental constants describing the plastic behaviour of the material;
ε_P is the true strain.

Other simple models were proposed over the years, as it is the case of the Ludwik's (Equation (2.26)), Voce's (Equation (2.27)) and Swift's (Equation (2.28)) laws, as shown in Table 2.

The Swift's law reflects better the constant slope of the stress–strain curve of metals at large strain than the Ludwik' law. The Voce's law is more suitable for moderate strain values [28].

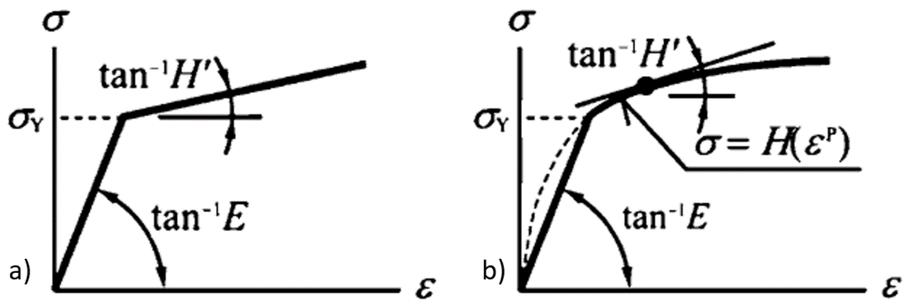

Figure 17 - Idealized plastic behaviour of materials: a) Linear work-hardening; b) Nonlinear work-hardening, adapted from [28].

Despite the advantages of the simple models, their applicability in the simulation area is limited, since they do not provide complete solutions, especially for high strains, strain rates and temperatures observed in the cutting processes. The most used and studied model is the one proposed by Johnson and Cook (Equation (2.30)) [30], which has a small number of parameters and a simple calibration. In addition to hardening, it incorporates terms of viscoplasticity and temperature. Since the Johnson-Cook model does not also correspond perfectly to stress values at very high strain rates, many different versions of the model were proposed over the years by different authors. Umbrello [31] et al. (2006) investigated the influence of the constants used in the Johnson-Cook model equation on the forces, temperatures, chip morphology and residual stresses in the machined components of AISI 316L steel. The best results were obtained in works where the constants were inversely identified through machining tests where material shear flow stress is matched to the one obtained in the primary shear zone based on cutting forces results as the works of Tounsi et al. [32] and Chandrasekaran et al. [33]. As the Johnson-Cook model neglects the coupling of strain, strain-rate and temperature known to occur in real materials, some authors suggested modified versions to include novel multiplicative strain and temperature dependent terms, as Calamaz et al. [34] and Sima and Özel [35].

Among the semi-empirical models, which are based on the fundamental physics with constants are based experimental data, the Zerilli-Armstrong (Equation (2.31)) [36] model has had considerable application for a variety of materials. For material flow stress calculations, it is based on the initial displacement density and displacement motion, having different relationships depending on the material structure [28, 29].

The Zerilli-Armstrong model is believed to provide a better approximation since the Johnson-Cook model does not consider the influence of the coupled effects of strain and temperature and of strain rate and temperature. Although the original formulation of this model does not include the absolute effect of strain rate and the coupled effect of strain and temperature, authors as Samantaray et al. [37] developed a modified version to account for these deficiencies. Over the years, more relevant material constitutive models have been proposed. Some of the more relevant are listed in Table 2.

Table 2 - Material constitutive model equations according to different authors [28].

Author (Year)	Model constitutive equation	Eq.
Hollomon	$\sigma = K(\varepsilon^P)^n$	(2.25)
Ludwik (1909)	$\sigma = \sigma_Y + K(\varepsilon^P)^n$	(2.26)
Voce (1948)	$\sigma = \sigma_Y + K(1 - me^{-n\varepsilon^P})$	(2.27)
Swift (1952)	$\sigma = \sigma_Y(1 + K\varepsilon^P)^n$	(2.28)
Swift-Voce	$\sigma = \alpha[\sigma_Y(1 + K\varepsilon^P)^n] + (1-\alpha)[\sigma_Y + K(1 - me^{-n\varepsilon^P})]$	(2.29)
Johnson and Cook (1985)	$\sigma = (A + B{\varepsilon_p}^n)\left[1 + Cln\frac{\dot{\varepsilon}}{\dot{\varepsilon_0}}\right]\left[1 - \left(\frac{T - T_0}{T_m - T_0}\right)^m\right]$	(2.30)
Zerilli and Armstrong (1987)	$\sigma = \sigma_a + Be^{-\beta T} + \beta_0 {\varepsilon_p}^{1/2} e^{-\alpha T}$ $\beta = \beta_0 - \beta_1 ln\dot{\varepsilon}$ $\alpha = \alpha_0 - \alpha_1 ln\dot{\varepsilon}$	(2.31)

2.1.4.3. Temperature modelling

The prediction of the temperature distribution in a cutting process is of critical importance since is a central and inseparable component of the process. Its simulation presents some difficulties as it is not easy to acquire a precise measurement. A true predictive model should estimate the temperature fields considering the empirical uncertainty.

Many researchers have developed finite element models to predict these distributions in the rake face and flank faces of the tools and in the chip. Coupled models, where initial predictions of forces and chip properties were used as inputs to the calculation of temperature distributions are the most common complete models, some of which include wear and coolant effects. Other numerical methods, such as the boundary element method and finite difference method, have also been applied. Although these methods cannot be used with a wide range of tool geometries and field equations, the computational time is reduced when compared to finite element methods [15, 25].

Stevenson et al. [38] developed a model that does not require flow field as input, and the basic mesh could be adjusted for shear angle and contact length over wide range. The measurement of the temperature distribution showed good agreement with the calculated temperatures (refer to Figure 18). Davies et al. [39] studied the differences between measured temperature fields and FEM models and concluded that large discrepancies could be found due to the following causes: (i) use of material data not suitable for the deformation regimes and/or (ii) heating rates encountered in machining; (iii) errors in the experimental system not accounted for by uncertainty analysis; (iv) poor implementation of the adopted machining modelling method; (v) failing in achieving an equilibrium temperature distribution in simulation.

Grzesik et al. [40] and Usui et al. [41] developed finite differences based methods. In the former, temperature was analysed for uncoated and coated carbide tools when machining C45 carbon steel at the cutting speed range of 72-145 m/min. The results demonstrated a reasonably good correlation (6%) compared to thermocouple measurements. Another important conclusion to be drawn from the study is related to the fact that the heat source shape influences the temperature distribution along the tool-chip interface. The trapezoidal heat source was the shape that better agreement between computed and measured average interface temperature values provided. The model of Usui et al. make use of the predicted cutting force based on the energy approach and the prediction of the crater wear progression was made with temperatures and stresses at the rake face.

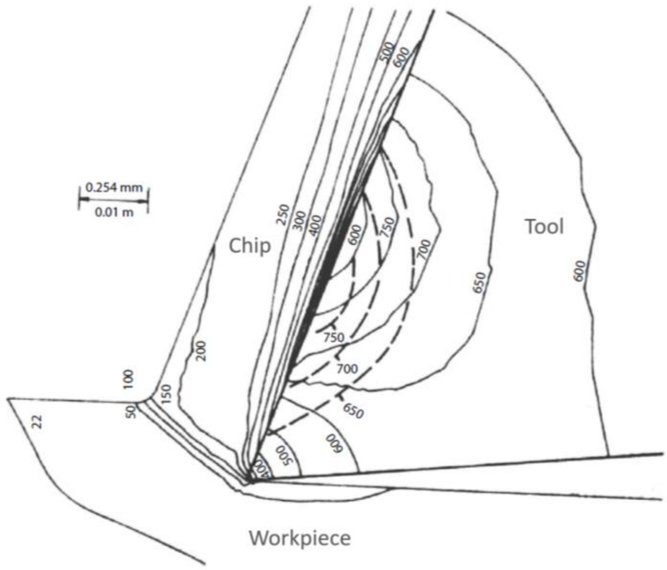

Figure 18 - Temperature distribution comparison between a FEM model developed by Stevenson et al. (continuous lines) and experimental results obtained by a metallographic method (dashed lines), adapted from [38].

2.1.4.4. Chip modelling

The modelling of the chip separation from the rest of the work material is a complex phenomenon that depends on several different parameters, involving many physical processes. As a result, the creation of a model that correctly depicts this experimental phenomenon is quite challenging.

Over the years, some different approaches have been applied. In the literature, the models used to simulate the separation of the chip from the workpiece could be categorised as: sacrifice layer; meshfree models; remeshing models and damage models. All these techniques have their respective area of usage, their pros and cons. In relation to the non-physical methods, the sacrifice layer, it consists in the chip separation along a predefined cutting plane that act as a sacrifice layer, splitting or eliminating elements. A critical distance between the tool tip and the nearest node along a predefined line have been used as indicator criterion to define the separation line.

As its base is non-physical with a separation line defined in advance, the chip separation is easy to control, and the mesh could be optimized for that area [42].

Regarding physical-based models, Eulerian formulation is not so used because, as described in section 2.1.4.1, they function as volume controls and it is necessary to define a chip geometry in advance, which makes difficult to study its morphology according to cutting parameters. Meshfree models have also been used and present some advantages when compared to Lagrangian FEM methods (refer to Figure 19). The non-required remeshing and separation criterion, in conjunction with the easiness to handle severe deformations, which is the case of machine cutting, make it useful for some studies even though it may not be as accurate as FEM [25, 42, 43].

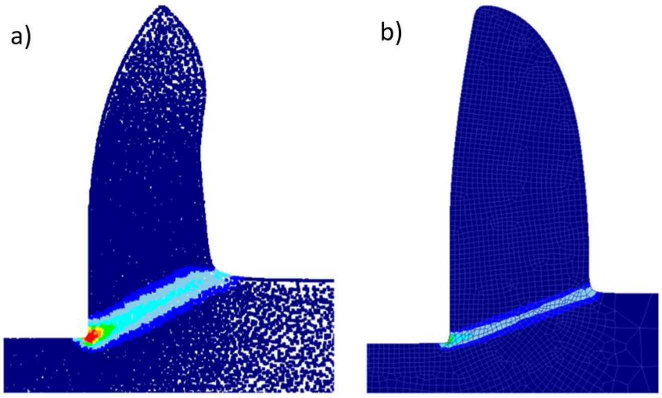

Figure 19 - Comparison of a meshfree (a) and a FEM (b) simulation, adapted from [44].

The remeshing method is used to continuously deal with highly deformed elements during the FEM analysis and alone is capable of perform chip-workpiece separation, without any damage criteria. A completely new mesh is generated from the old distorted one and so (refer to Figure 20), a good data transitions has to occur in order to achieve good results. Although it presents some advantages when compared with other element failure models, it represents a high computational cost which results in long time simulations [25, 42].

The last, and probably the most common method make use of a damage criteria to split or delete elements during the formation of the chip. The elimination of elements has as disadvantage the loss of mass and to account for this problem a fine mesh has to be generated, which reduces the overall computational gain when compared to the remeshing method [42].

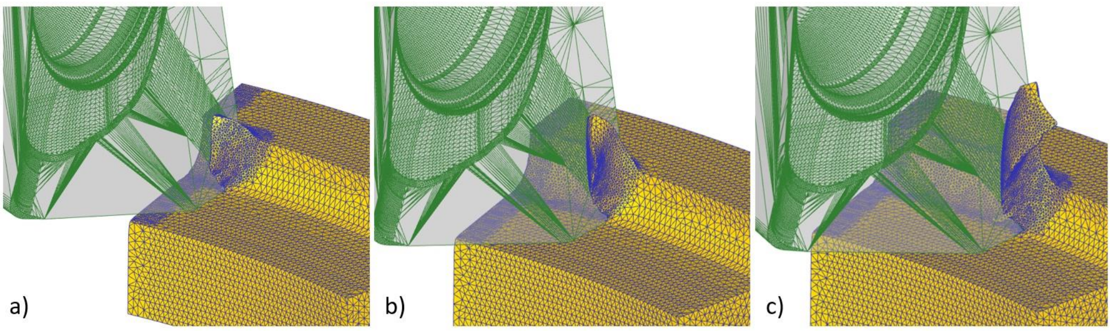

Figure 20 - Remeshing process in DEFORM software during cutting simulation (a)-c)).

In relation to the damage criteria, some have been proposed over the years as the constant equivalent strain criterion and maximum shear stress criterion, and fracture models like Johnson-Cook criterion and Cockroft-Latham criterion. The strain and maximum shear stress criteria assumes the fracture when plastic strain or shear stress calculated at the nearest node to the cutting edge reaches a critical value. A too fast propagation could occur, forming a large crack ahead the tool tip, if the method is not well controlled. The Johnson-Cook failure criterion (Equation (2.36)) assumes the fracture when an equivalent fracture strain critical value, function of stress, strain rate and temperature, is achieved. The Cockcroft-Latham fracture criterion (Equation (2.35)) is another similar criterion [18, 25]. Some of the most used damage criteria are shown in Table 3.

Table 3 - Most common damage criteria [8, 18, 25].

Criterion / Author (Year)	Criterion definition	Eq.
Nodal distance	$d = d_{cr}$	(2.32)
Equivalent plastic strain	$I_{cr} = \varepsilon$	(2.33)
Energy density	$I_{cr} = \int \sigma : d\varepsilon$	(2.34)
Cockcroft and Latham (1968)	$d = \int_0^{\varepsilon_f} \sigma_1 \, d\varepsilon$	(2.35)
Johnson and Cook (1985)	$d = \left(d_1 + d_2 e^{d_3 \frac{\sigma_m}{\sigma}}\right)\left(1 + d_1 ln \frac{\dot{\varepsilon}}{\dot{\varepsilon_0}}\right)\left[1 + d_5\left(\frac{T - T_0}{T_m - T_0}\right)\right]$	(2.36)

2.2. Additive manufacturing

Additive manufacturing could be defined as a process of adding material, usually layer upon layer, guided by a digital model in order to obtain a three-dimensional part. These technologies enable the production of complex or customized parts, some impossible to manufacture by traditional processes. Without the need for expensive tooling or forms such as punches, dies or casting moulds, the cost and time needed to produce small series or prototypes is drastically reduced. In addition, there are no limitations in terms of commercial shapes available, as for example tubes and sheets, assembly steps could be reduced or eliminated, and almost only the material that makes up the part is required, as opposed to traditional machining and forming processes, which contributes to cost reduction (refer to Figure 21). For these reasons, AM is now widely accepted as a new paradigm for the design and production of high performance components for aerospace, medical, energy and automotive applications [1].

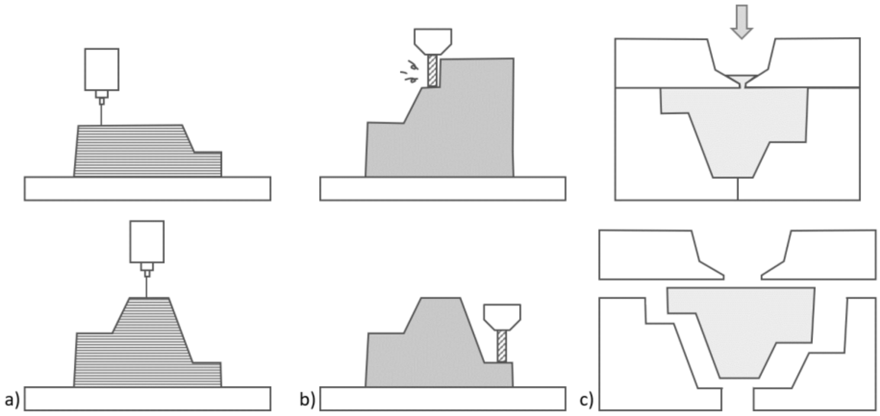

Figure 21 - Manufacturing processes: a) Additive, b) subtractive, c) formative, adapted from [45].

The wide-range of possibilities in metal parts industry quickly led additive manufacturing from only polymers to metal processing. Metal additive manufacturing, as the name indicates, refers to the processes that enable the manufacturing of metal parts by additive manufacturing methods. In recent years, there have been an exponential increase in MAM options, with many new companies entering the market.

Although there are some processes that could produce metal parts, the processes of powder bed fusion (PBF) and direct laser deposition (DED) are used in the majority of metal applications as they provide near net shape parts with only one stage, without the need for sintering or other operations. The sheet lamination process, where material sheets are bounded to create an object, could make use of metal sheets; however, it requires welding mechanisms for consolidation and CNC contour milling for ensuring the parts' shape. Other processes as binder jetting, where a bounding agent is selectively deposited to bound material particles, and material extrusion, which make use of a nozzle to deposit material layers, could also produce metal parts. These processes involve washing and sintering stages. Due to these facts, this literature review will focus on the description of PBF and DED, especially the former, since it is the process used in the production of the specimens used in the tests of this thesis [45].

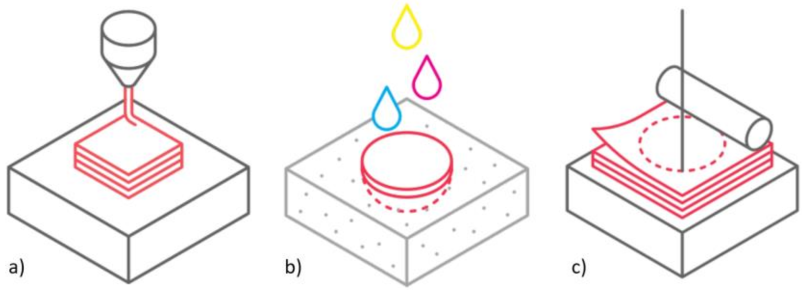

Figure 22 - Less commonly used processes MAM processes: a) material extrusion, b) binder jetting, c) sheet lamination, adapted from [45].

Direct energy deposition is a group of additive manufacturing processes that consist of material feeding alongside the heat input simultaneously, as shown in Figure 23. The heat input can either be a laser, electron beam, or plasma arc. The material feedstock is either powder or wire. As a powder bed is not needed, during the process, materials can be changed from layer to layer. Compared to PBF, DED systems are often larger in size, require higher energy density and have a poorer surface quality [46].

Usually, the heat source is moved relatively to the workpiece depositing raw material layer upon layer. As the particles (or wire raw material) are deposited, the heat input delivers sufficient thermal energy to melt the particles along the deposition path, with a surrounded inert gas atmosphere to prevent oxidation, creating a molten pool (liquid metal) and a heat affected zone (HAZ) with varying penetration depth. Once deposition of a single layer is complete, the build plate moves via CNC relative to the deposition head and the process is repeated. DED often uses multiple axis turntables to rotate the build platform in order to repair or print on existing parts [47, 48].

Even though the use of wire as feedstock material can increase the process efficiency and surface quality, their use in the industry is a minor fraction when compared to powder fed. This greater use of powder is due to the fact that it is easier to control in real time and therefore allows for more accurate manufacturing of complex geometries. Wire requires more control and is susceptible to vibration and disturbance. In addition to this, when not used, powders can be recycled, which contributes to a better use of resources [47].

The DED processes are quite complex to model/control due to the large number of variables. The occurrence of many interconnected physical events in a short period of time contributes to this complexity [47].

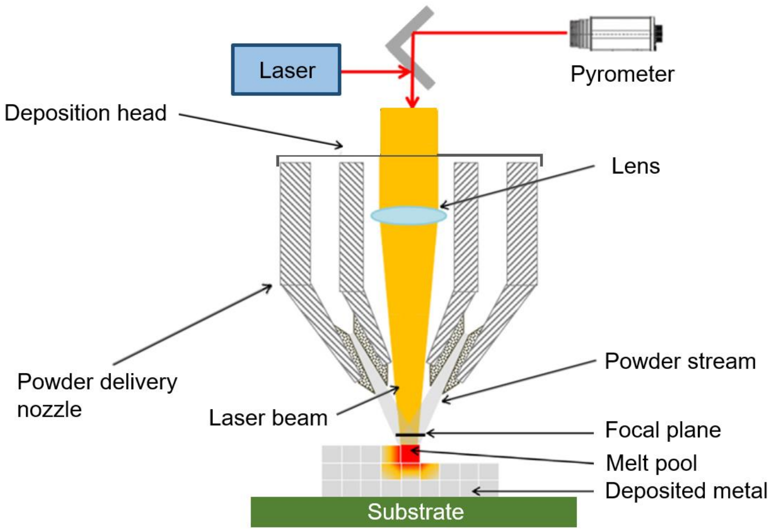

Figure 23 - Laser-based Direct Energy Deposition process diagram, adapted from [47].

2.2.1. Powder bed fusion

The additive manufacturing process of Powder Bed Fusion consists in the creation of a component based on the bounding by a heat source of metallic powders disposed on the build platform. The process initiates with a formation of a powder bed in the build platform, which is taken from a supply recipient automatically, then the heat source scan the powder layer according to the defined scan path. To restart the cycle, the building platform is lowered according to the layer thickness and a new powder bed is formed. The cycle continues until the part is completed.

As the DED processes, PBF makes use of vacuum or inert gas atmospheres to prevent oxidation and contaminations [1, 49].

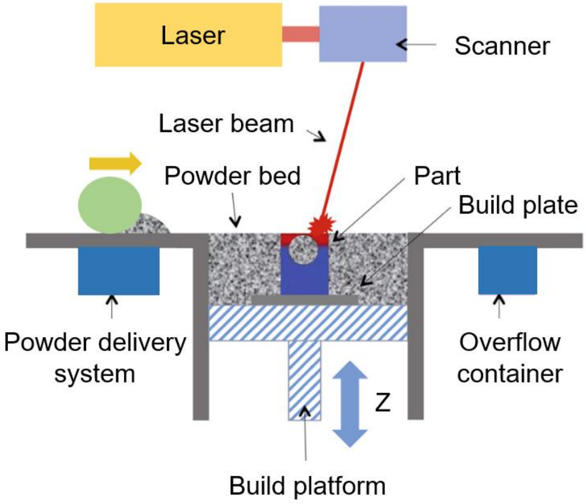

Figure 24 - Laser-based Powder Bed Fusion process diagram, adapted from [47].

In PBF, the heat source could be either a laser beam or an electron beam and it could fully melt the metal particles or heat them to a point so that they can fuse together on a molecular level. When an electron beam is used as heat source (E-PBF), there is a complete fusion of the powder particles and the process has a generally superior build speed, because of its higher energy density. However, it could only use conductive materials and the higher energy density results in a poorer accuracy: larger minimum feature size, powder particle size, layer thickness and poorer surface quality when compared to laser-based Powder Bed Fusion (L-PBF) [47, 50].

In order to improve the adhesion of the first layer, the build plate is usually heated to approximately 200 ºC in laser systems and 700 ºC in electron beam systems. This build plate is generally of the same material as the processed metal powder, which ensures metallurgical compatibility as well as identical heat expansion, minimizing residual stresses. As in the final, the build plate is linked to the part as one piece, it has to be removed, and typically EDM is applied [1, 49].

Unlike the polymer version, in PBF, structural support is required, in order to limit the likelihood of any distortion that may occur, despite the fact that the surrounding powder provides physical support. On the other hand, as in the polymer version, the powder that was not used is commonly sieved and reused. Due to the high processing temperatures and the re-melting phenomenon, printed components are typically heat treated after printing, while still attached to the build plate, to relieve any stresses in the parts due to printing. Regarding the laser-based PBF processes, solid state lasers (for example: fibre lasers) are commonly used.

In order to have a comprehensive knowledge of all physical principles present in the process, there has been an intensive investigation of L-PBF. The improvement of the degree of maturity of the process has enabled, nowadays, the use of L-PBF not only for prototyping but also for the manufacturing of final and customized parts [50].

This literature review will focus on the characterisation of L-PBF, especially the characteristics of methods that consist in full fusion of powder particles, since it is the process used in the production of the specimens used in the tests of this thesis.

2.2.2. Manufacturing parameters

The powder bed fusion process has several parameters that affect the quality of the parts obtained. These parameters are mainly related to the scanning geometry, the nature of the laser and the raw material.

Regarding the scanning geometry, it could vary as to scanning speed, hatch spacing, layer thickness and scanning strategy (refer to Figure 25). The laser scanning speed can generally range from 150 mm/min to 15 m/min. Increasing the speed favours the productivity of the process, however, care must be taken when choosing a maximum speed so as not to compromise the integrity of the parts. The hatch spacing defines the distance between successive sweeps and needs to be defined together with the other parameters in order to observe good adhesion between different layers and different sweeps. In parts produced by additive manufacturing it is common to observe overlapping melt baths. Layer thickness is also very important in the production of AM parts. The thickness must be uniform throughout the entire layer and the properties of the powder, the material of the blade that spreads it and the surrounding atmosphere all play a role in the production process [51].

In relation to the scanning strategy, it refers to the paths followed by the heat source during additive manufacturing processes. More complex strategies, such as sectorial "chessboard" (refer to Figure 26 c)) developed by Concept Laser GmbH, are currently used in order to reduce residual stresses in the final parts. In addition, different orientation rotations of the deposition between layers are commonly used in order to decrease the anisotropy of the parts produced by additive manufacturing (refer to Figure 26 e) to h)). In order to improve the surface quality, it is common to first sweep the entire outer perimeter and then deposition in the inner region (refer to Figure 26 d)) [51, 52].

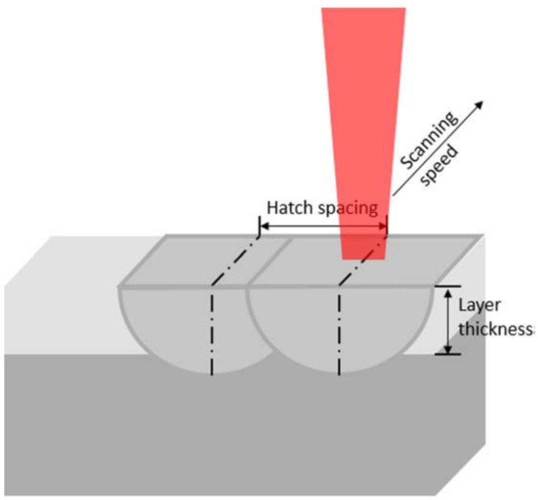

Figure 25 - Scanning geometry parameters: hatch spacing, layer thickness and scanning speed, adapted from [51].

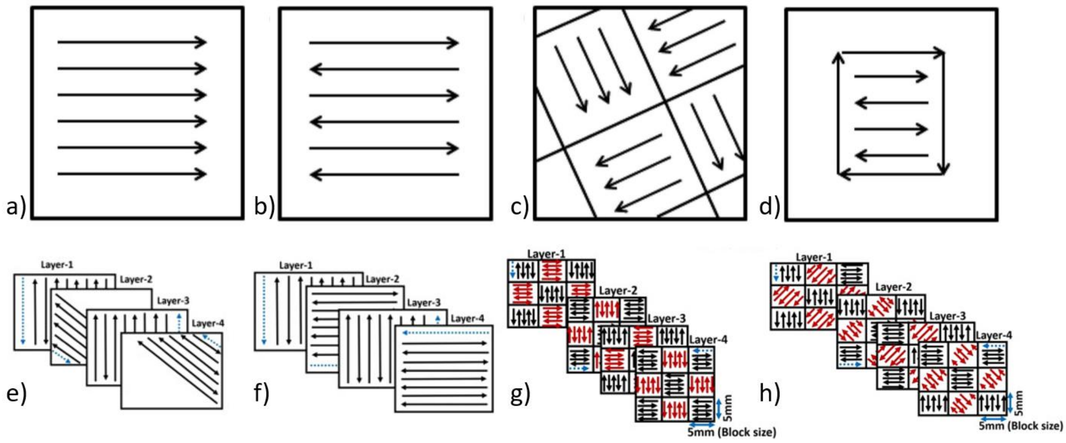

Figure 26 - Different scanning strategies: a) unidirectional, b) bidirectional, c) sectorial ("chessboard"), d) bidirectional with linear melting of the contours; different scanning schemes: e) stripes alternating 45°, f) stripes alternating 90°, g) chess with adjacent blocks alternating 90°, h) chess with adjacent blocks alternating 45°, adapted from [52, 53].

With regard to the heat source used, the laser power, the spot size, the scan field as well as the laser type are the parameters to be considered. The laser power has a direct influence on the melting pool and is generally between 20W and 1 kW. The values of laser power and scanning speed are usually conciliated in order to maintain constant thermal delivery.

The spot size is considered to be the diameter of the laser beam at the focal plane. This parameter influences the resolution of the process, i.e., the smaller it is, the finer the details of the parts built. For SLM technologies, it is generally around 50 to 180 μm. In machines using multiple lasers, the area of "responsibility" of a laser is called the scan field. The use of multiple lasers in some situations avoids large temperature gradients in very large parts, contributing to a reduction in residual stresses.

The quality of the raw material is of paramount importance and is determined by the size, geometric shape, surface morphology and internal porosity. This quality is usually evaluated quantitatively by variables such as fluidity and apparent density. Density assesses the degree of compaction of the powder and fluidity the flowability of the particles. It is important to note that spherical particles improve the fluidity and the apparent density of the powder, because the sliding of spherical surfaces is of less friction when compared to irregular geometries, while fine particles although improve the apparent density, by reducing the spaces between particles, hinder its fluidity [54, 55].

2.2.3. Influence on material properties

The parameters discussed have an influence on the characteristics of the materials produced by additive manufacturing. Then the influences on mechanical characteristics, roughness, microstructure, and hardness are presented.

2.2.3.1. Relative density and surface roughness

The density of PBF parts could be seen as a fundamental property that determines the resultant mechanical properties and influences their performance. Despite the increase in mechanical properties, a less dense part could provide advantages in terms of weight.

One of the parameters that most influences the density of the final parts is the laser power, which is directly related to the relative energy applied. Many researchers have studied this influence in maraging steels. Casalino et al. [56] varied the laser power between 57 and 100 W, obtaining relative densities of 99.9% for the highest powers and with the slower scanning speeds, which was also obtained by Bai et al. [57] for laser powers between 100 and 190 W. Mutua et al. [58] carried out tests for higher laser powers (100-400 W) and concluded that too high powers lead to a decrease in relative density. Although the increase of laser power leads to the full melting of powder, in these cases, the higher laser powers result in a strong vaporization and spatter in the metal molten pool as the relative energy is too high, leading to a lack of sufficient liquid metal to fill the molten track and lots of voids, which result in a decrease of relative density. In Figure 27, it is shown the differences between the two extreme cases: lack of power and excess of power, with the formation mechanism of spatters and voids under the action of laser beam.

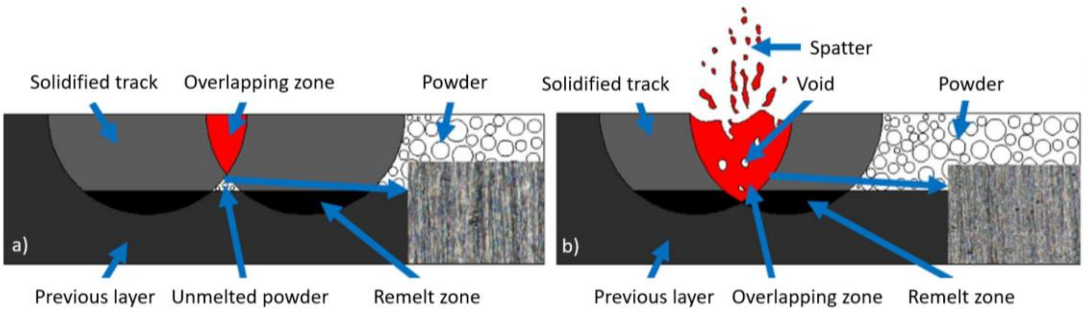

Figure 27 - Effect schematic of the energy density: a) lack of energy density; b) excess of energy density, adapted from [57].

Despite the great influence of the laser power in the relative density of the parts, other process parameters as the scanning speed, pitch, overlap rate have also significant impact in this property. Mutua el al. [58] and other researchers [56, 57] made studies on the influence of these parameters in the final quality of the parts. The scanning speed has an opposite influence of the laser power, as an increase in speed does not favour such a good fusion of powders. The same logic could be applied to the overlap rate or pitch, where bigger melting pool and a smaller distance favour the increase in relative density.

Regarding the surface roughness, the laser power is also the most significant parameter, as demonstrated by Casalino et al. [56] in their studies. In line with previous reasoning, the process requires an energy density capable of producing an effective melting of the particles, without resulting in an excess of power. The full melting of the powder smoothes the surface, as opposed to a higher power which favour the occurrence of spatters which will result in a sharper irregular roughness. For a laser power of 100 W and a scanning speed of 180 m/min, Casalino et al. [56] obtained specimens with a surface roughness (Sa) of 15 μm. By using slower scan speeds

(≈ 55 m/min), Fortunato et al. [59] and Bai et al. [60] were able to produce parts with surface roughness around 11 μm.

2.2.3.2. Microstructure and hardness

The material microstructure has an important role on the machinability of metal parts. The microstructure resultant from the PBF process has a solidification pattern characteristic of the molten/re-solidified zones with almost parabolic edges, as seen in Figure 28. This is a result of the solidification of each layer on the underlying layers, in other words, the laser tracks overlapped each other, which reduces the porosity. In perpendicular direction to these parabolic edges, clear melt tracks could be seen as result of the building direction and scanning strategy [60, 61].

When observations are made at higher magnifications it is possible to identify fine normal and deformed cellular microstructures could be seen (refer to Figure 29 b) and c)), which is due to the high cooling rate. These structures are affected by heat transfer between both tracks and layers. The melt track in formation has a higher temperature than its surroundings, which increases the temperature gradually from the pre-built melt track to the current melt track. This temperature gradient causes the formation of a strip structure morphology growing perpendicular to the boundary. This effect is also observed between different adjacent layers. The temperature gradient rate has an important role in the final microstructure of the part, the higher cooling rate, the finer microstructure features are. As gradient decreases, crystallization mode changes from planar to cellular, cellular-dendritic and, finally, dendritic solidification mode [60, 62].

As shown in the Figure 29 b), the directions of the white boundaries of the deformed cellular structure are approximately perpendicular to the boundary.

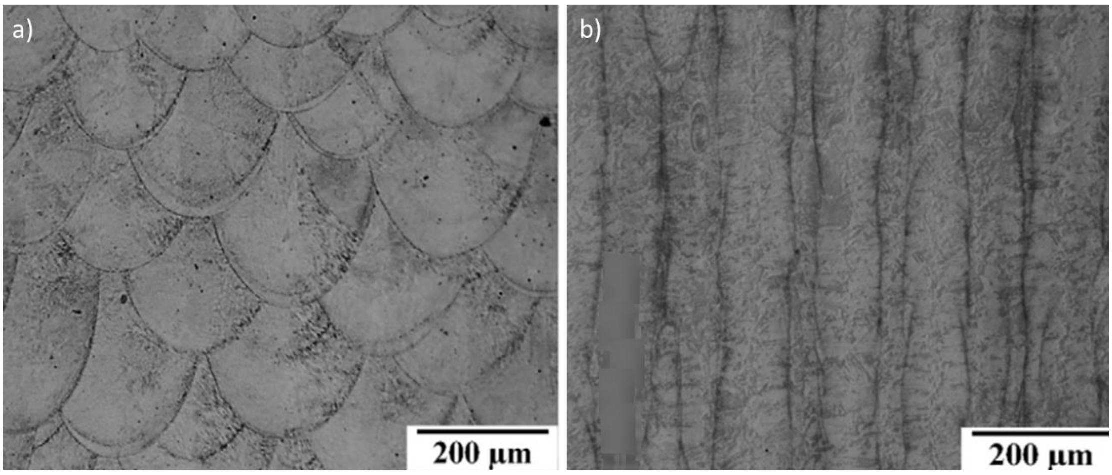

Figure 28 - Metallographic samples of AM 18Ni300 in parallel (a) and in perpendicular direction (b) to building direction, adapted from [58].

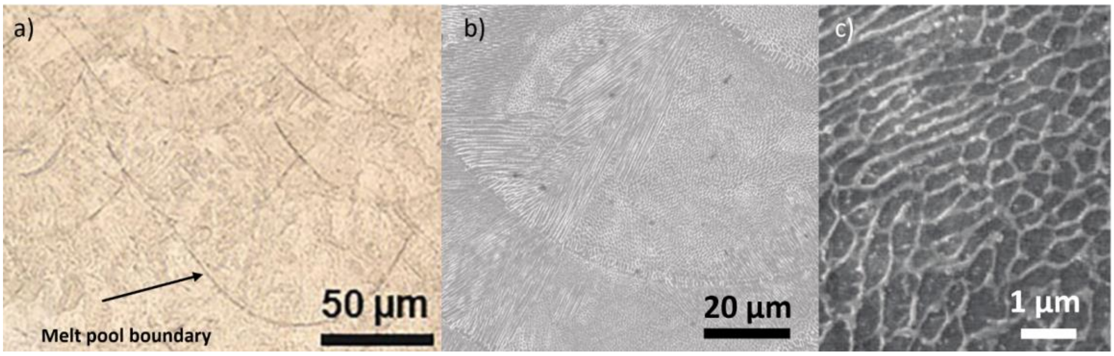

Figure 29 - SLM maraging steel microstructure with different magnifications: a) LOM picture adapted from [61], b) and c) SEM picture, adapted from [63].

Due to these growth mechanisms and the intercellular spacing less than 1 µm, excellent strength and hardness are found in LPBF materials. Kempen et al. [63] concluded that scanning speed and layer thickness had an important impact on the hardness of the AM maraging steels. These parameters influence the cooling rates, as explained above, and change the resulting microstructure. Higher scanning speeds and layers with smaller remelting zone will increase the cooling rate and produce fine microstructure, increasing the overall hardness [64].

Regarding AM maraging steels, Demir and Previtali [64] produced parts with 360-380 HV. Similar results were also found by other researchers [56, 58]. These materials are commonly subject to solution treatment and aging treatments in order to improve the material's characteristics. Bai et al. [57] studied the influence of the heat treatments in a AM maraging steel and registered an improve from 381 HV to 646 HV after the as built material has been subjected to the solution and aging treatments, respectively. This result could be explained by the dissolution of Ni, Mo, and Ti in the matrix, forming Ni3Mo, Fe2Mo and Ni3Ti which generates precipitation strengthening. The second phase particles precipitated strongly hinder the movement of dislocations which significantly enhance the hardness of the samples [57].

2.2.3.3. Mechanical properties/residual stress

In order to evaluate the performance of materials produced by additive manufacturing and compare them with their counterparts produced by conventional processes, many researchers have carried out tests normally used in the characterisation of metallic materials such as tensile, compression and Charpy tests, among others.

As demonstrated in the study of Kempen et al. [63], it was possible to observe a higher yield stress (≈ 1214 MPa), tensile strength (≈ 1290 MPa) and lower Young's modulus (163 GPa) in AM maraging specimens than in wrought maraging steel. This is a result of the occurrence of aging during the PBF process when the melting track constantly heat the layers and material beneath. The precipitation phenomenon accompanied with the cellular growth in the heat affected zones may facilitate this. With regards to the building direction, no significant differences were found, however the building direction parallel to the loading direction tends to have slightly lower tensile strength and much lower elongation, due to layer separation.

Casalino et al. [56] noted a great influence of the density on the tensile strength results obtained and on the fracture behaviour of the material itself. With an increase in relative density from 91% to 99%, the actual fracture behaviour shifted from the brittle one to the ductile one. As stated by Manfredi et al. [65], this is due to the reduction in size of the voids presented in the AM process, avoiding macro-voids which do not coalesce and bring the part to a brittle rupture.

As mentioned in Section 2.2.3.2, these alloys are usually subjected to heat treatment to improve their mechanical properties. Mutua et al. [58], who also carried out tensile tests with similar results, observed an increase of about 100% in the tensile strength when the specimens were subjected to a solution and an aging treatment. On the other side, the ductility decreased from 10% to 5%.

Bai et al. [57] preformed Charpy tests in order to evaluate the toughness of an AM maraging steel. It was found that the impact energy of as built samples is very high, showing good impact toughness, which is result of a fine microstructure of the AM parts.

2.3. Machinability of AM produced metals

Over the course of the last two decades, the application of additive manufacturing processes has drastically increased, evolving from prototype parts to real part components production. These processes have been actively used to manufacture different metallic parts in materials such as maraging steels, tool steels, titanium alloys and others [66]. As previously mentioned in Section 1.1, the traditional machining processes continue to have a significant importance in order to achieve the quality required in many industries in terms of surface quality and dimensional accuracy. Over the past decade, the scientific investment in the area of AM metallic parts machining has registered an exponential growth, as may be seen in Figure 30. The non-continuity of the trend in 2021 may be explained by the appearance of the Covid-19 pandemic and in 2022 because at the time of recording these data, the year was still halfway through.

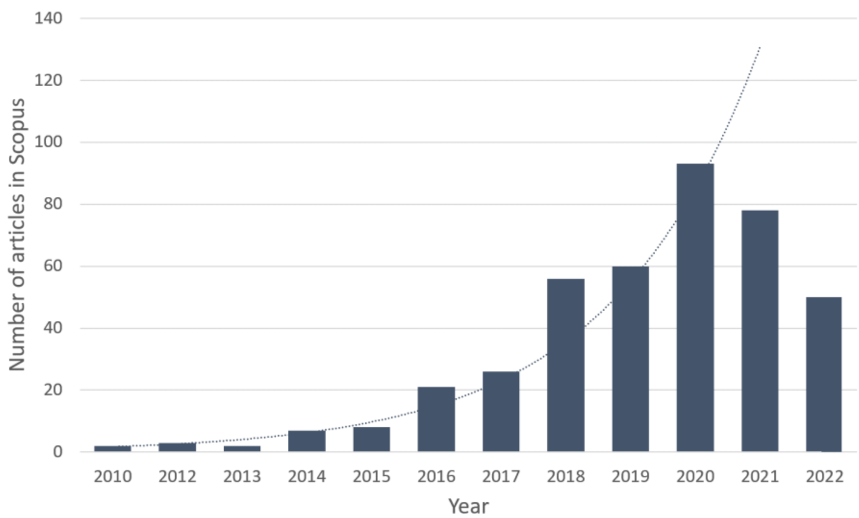

Figure 30 - Number of articles per year in Scopus on the subject of machining of metallic materials produced by additive manufacturing.

The study of post-processing machining of AM metal parts is focused mainly on titanium alloys, especially Ti6-Al-4V, nickel and chromium super alloys, such as Inconel 625 and Inconel

718, and high corrosion resistance steels such as AISI 316L stainless steel and maraging steels such as 18Ni300 steel. Their excellent strength, good corrosion resistance, and good strength to ductility ratio make these materials excellent choices for applications with high demands such as aerospace, aeronautical, military, marine, mould (refer to Figure 31) and medical industries. The combination of these characteristics with their good weldability makes them ideal candidates for use in the production of parts produced by additive manufacturing for high value-added applications, capable of withstanding the high costs associated with metal additive manufacturing (MAM). Post-processing machining is needed to correspond to the high requirements in terms of precision and tolerance of these areas.

Figure 31 - Example of a car tyre maraging steel mould produced by additive manufacturing [67].

Additive manufacturing processes yield anisotropic parts which in a post-processing stage, could result in different machining characteristics. Guo et al. [68] studied the effect of building direction on the microstructure, mechanical properties and machinability of the AISI 316L stainless steel produced by direct laser deposition. Differences were found between directions of the pieces due to anisotropy caused by the process used. It was possible to observe that perpendicular-to-build direction, the microstructure was homogeneous, which resulted in tensile properties and hardness values higher than those in parallel-to-build direction. The same trend was observed for the cutting forces, tool wear and surface roughness. These results reflect the lower mechanical properties in build direction (due to the well-known phenomena of columnar grain formation along that direction). This results in a higher density of grain boundaries in perpendicular-to-build direction and, therefore, higher mechanical strength.

Several studies have been carried out on these materials as is the case of Bordin et al. [69], who evaluated the tool wear mechanisms in turning operations of additive manufactured Ti-6Al-4V, under dry and cryogenic conditions using coated tungsten carbide inserts at varying cutting speed and feed rate. The results demonstrated a reduction of adhesive wear mechanism of the workpiece material on the tool cutting surfaces when using cryogenic cooling compared with dry cutting.

Regarding additive manufactured maraging steels, noteworthy studies have been carried in the last years. After a preliminary experimental campaign to determine the optimal AM process parameters, Fortunato et al. [59] carried out milling tests under different build directions, heat treatments and cutting speeds. It could be seen that the mean hardness of all samples increases slightly after milling due to the associated plastic deformation and there was no significant difference, in terms of hardness, between different building directions. The highest hardness was obtained for solutionized and aged samples, with a value around 56 HRC. In terms of surface roughness (Sa), all process combinations resulted in values below 0.45 μm and a minimum value of 0.175 μm was achieved. Oliveira et al. [70] investigated not only the effects of different cutting speeds, but also different feeds per tooth, finding that the variation of two parameters contributed to an improvement in surface roughness and compressive residual stress of the specimens. Those results highlight the importance of considering both parameters in the milling process of AM maraging steel parts. A minimum surface roughness (Ra) of 0.31 μm was achieved when a feed of 0.02 mm/tooth and a cutting speed of 250 m/min were adopted.

In addition to the variation of cutting parameters, Neuenfeldt et al. [71] additionally studied the variation of AM process parameters and how the whole process could be optimized in order to obtain the best results. For most milling parameter sets, an increase in surface roughness with an increase of scanning speed was noticed. In addition, it was found that the AM process parameters that lead to higher porosity induce lower cutting forces. Tamura et al. [72] focused on studying the characteristic anisotropic behaviour of AM materials, and its influence in the measured cutting force through milling tests on maraging steel. Differences in shear stress on the shear plane due to the anisotropy in the workpiece have been reported. It was also noted that the shear stresses become small at the edge engagement, the maximum uncut chip thickness, and the edge disengagement. The authors also produced a model to predict not only the cutting force but also the changing rate in the cutting force. Bai et al. [60] investigated the influence of microstructure evolution on the machinability of the AM specimens. Solution-treated samples (620 HV) presented higher surface roughness (Ra ≈ 0.6 μm) than as-built parts (375 HV), which showed an average Ra of 0.4 μm. These differences were associated to defects, such as adhered chip segments, that are formed on the ageing-treated samples. Solution-treated and as-built samples showed better machinability, with a decrease of 40% - 50% in surface microhardness, cutting force and tool wear. Oliveira and Conte [73] analysed the influence of milling cutting parameters, build orientation and thermal treatments in the average roughness and residual stress of maraging steel samples. The best surface roughness (Ra) was around 0.38 μm, which goes in line with literature [59, 60, 70], with a feed per tooth of 0.02 mm/tooth. The variation of cutting speed did not yield significant differences in terms of roughness. The compatibility between processing AM parameters and post-processing through milling process seemed to be notoriously relevant when it comes to surface condition improvement.

Some researchers studied the possibility of performing in the same machine, with alternative steps, additive manufacturing processes and machining operations. Wüst et al. [74] used an hybrid machine combining an AM process and three-axis milling to produce maraging steel parts, as shown in Figure 32. Similar results in terms of surface roughness were obtained in the final parts when compared in the studies which opt for separated operations. Du et al. [75, 76] and Sarafan et al. [77] also make efforts using similar machines and obtained similar results. Inspection of the part dimensions after hybrid manufacturing indicated high accuracy in the final geometry in the overall deviations. It was observed that after the milling operations, the AM parts recorded higher compressive residual stresses than those recorded for the wrought material due to the low plasticity of the AM material.

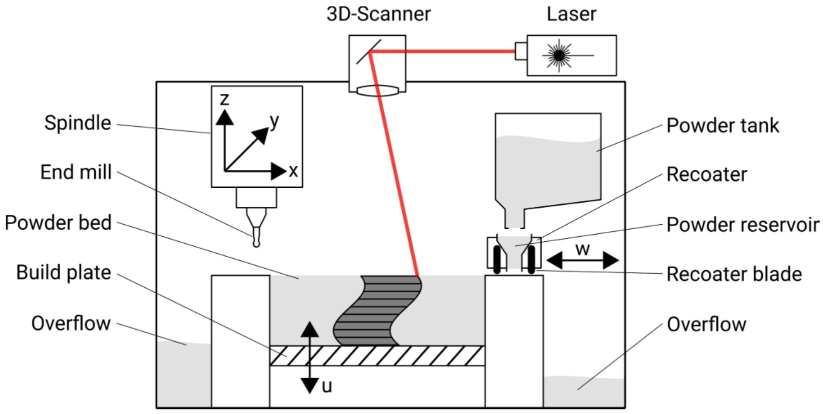

Figure 32 - Schematic illustration including movable axes of the hybrid additive manufacturing machine used in the work of Wüst et al. [74]

3. Experimental and numerical procedures

As mentioned in Section 1.2, the main goal of this dissertation is to evaluate the machinability of additive manufactured 18Ni300 maraging steel. For this purpose, a comparison between the AM maraging steel and a conventional manufactured (CM) maraging steel through milling tests was carried out. Prior to performing the machining tests, a characterisation of the two materials was performed, in particular of the steel produced by additive manufacturing. In MAMTool project, Silva [18] carried out a more extensive mechanical characterisation of AM maraging steel with a view of developing a constitutive model of the material. In the numerical studies presented in this dissertation, the same model was used for simulations of the milling process.

3.1. Material characterisation

In order to address the milling tests, sets of test specimens of each material were built. The additive manufactured specimens were built, through laser powder bed fusion, using an ytterbium laser with a spot size of 70 µm. These parts were built according to manufacturer's recommendations for optimal printing conditions. In order to fully understand the materials' as-built conditions, a comprehensive analysis of some properties as roughness, hardness, microstructure was preformed, as described in the following sections.

A more detailed description of the printing parameters of the AM specimens can be found in Table 4. Prismatic parts were built in height position, as shown in Figure 33 a), according to the manufacturers' recommendation for optimal printing conditions and overall quality.

Table 4 - Printing parameters of the AM 18Ni300 specimens: laser power, P_L, scan speed, v_s, hatch spacing, h_s, layer thickness, d_s, particle size distribution, PSD.

P_L [W]	v_s [m/s]	h_s [µm]	d_s [µm]	PSD (d10/d90)
400	0.86	95	40	15/45

The CM material was produced through Vaccum Arc Remelting. The specimens were produced to the required dimensions (refer to Figure 33 c)) and subjected to a griding, unlike those produced by additive manufacturing which were tested in the as-built state.

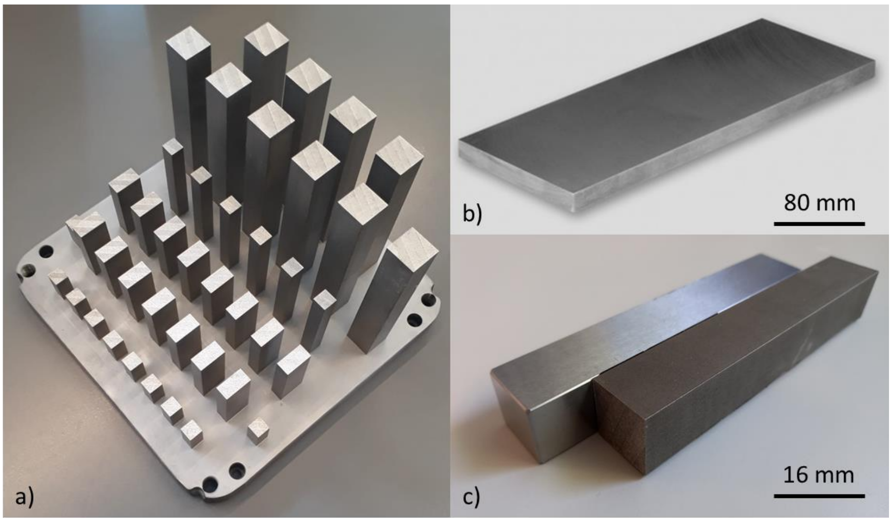

Figure 33 - a) As-built AM material samples attached to build plate, b) CM steel plate, c) CM and AM specimens produced (dimensions: 120x20.5x20.5 mm3).

3.1.1. Optical and electron scanning microscopy and chemical analysis

As mentioned in Section 2.2.3.1, the porosity in AM parts plays an important role in the mechanical properties of the final parts. Samples were cut in two distinct directions (perpendicular and parallel to the build direction), embedded in resin, polished (Struers Pedemax-2, INEGI), and finally observed in the optical microscope (Olympus PMG3 and Zeiss Axiophot), shown in Figure 35 a), without the use of etchant to reveal the presence of pores on the surface. In order to obtain a representative result of the porosity of the machined parts, measurements were made in two different directions using various micrographs. Through the use of ImageJ software, binary maps were generated for easy measurement of the percentage of pores on the surface. In Figure 34, it is possible to observe an example of a binary map generation from a metallographic sample, where black correspond to pores in the sample.

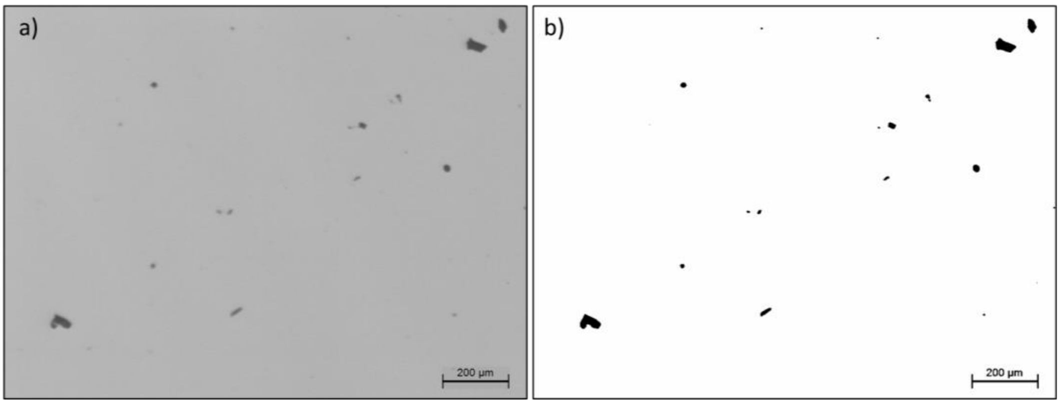

Figure 34 - Porosity analysis of AM produced parts: a) unetched metallographic sample, b) binary image.

According the objective of evaluating the microstructures presented, the samples were subjected to electrolytic etching to highlights important features like laser scan tracks, melt pools boundaries and others. The electrolytic etching was performed using Oxalic Acid Dihydrate, in an electrolysis cell where D.C. current was applied on the specimen, controlled by the regulation of the current value and the duration of the process. Chips, machined surfaces, and cutting inserts were also observed under the scanning electron microscope (SEM) in order to obtain higher magnification images and a more detailed analysis. The equipment used (refer to Figure 35 c)) was a high-resolution environmental scanning electron microscope, with X-ray microanalysis and analysis of backscattered electron diffraction patterns (FEI Quanta 400FEG ESEM / EDAX Genesis X4M) in CEMUP (Materials Centre of the University of Porto) facilities.

Chemical composition analysis of the considered materials in this study was performed using spark emission spectroscopy (SPECTROMAXx, at INEGI), shown in Figure 35 b). Knowing the chemical composition of each considered alloy, enables the comparison/verification compliance with material standards, for each alloying element.

Figure 35 - a) Optical microscope OLYMPUS PMG3; b) spark emission spectroscopy SPECTROMAXx; c) Scanning Electron Microscope (FEI Quanta 400FEG ESEM / EDAX Genesis X4M) at CEMUP

3.1.2. Hardness, roughness, and residual stress analysis

Hardness measurements (HV) were conducted according to standards ISO6507 and ISO6508. These measurements were performed on polished specimens before machining and on machined surfaces. In order to reduce the number of samples analysed, the Taguchi method was implemented, thus reducing the number from 54 to 18 samples. Three repetitions were performed on each analysed sample. Figure 36 a) shows the EMCO Test M4U-075 hardness measurement machine. In addition, microhardness measurements (Shimadzu HVM-2000 - refer to Figure 36 b)) were conducted at the machined surfaces and in-depth, as described in Figure 36 c). For this purpose, the specimens were cut in a direction perpendicular to the machining feed direction using a disc saw machine and embedded in resin (through compression mounting).

Another important aspect in AM manufactured and milled samples is overall surface quality. Roughness through parameters Ra, Rz and Rz max, were measured using a portable profilometer MITUTOYO Surftest SJ-210 (refer to Figure 37 a)) provided in the DEMEC Workshops. Three measurements were taken on each surface, for all combinations. In this analysis the Taguchi method was not used as it is a key parameter in the analysis of the surfaces obtained. On the as-built AM specimens, measurements were taken on the surface parallel to the building direction, which was to be machined. As the specimens were constructed in height and the area perpendicular to the direction of construction was very small, the anisotropic differences of the material were not evaluated in this thesis, especially taking into account the very small difference in mechanical strength associated to each direction [18]. The CM specimens were also analysed on the surface to be milled, previously machined and grinded. For the machined specimens, measurements were taken in the machining direction and in the direction perpendicular to the machining feed direction.

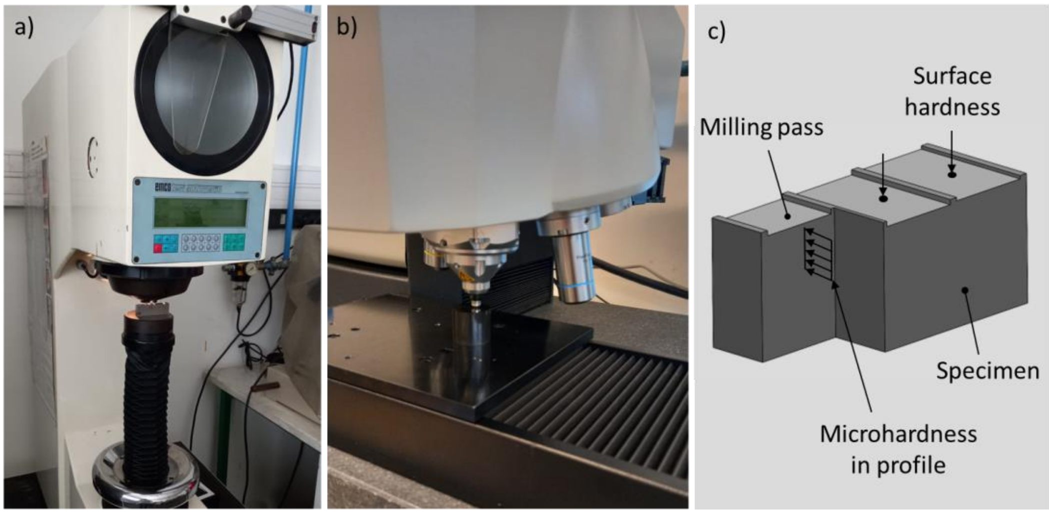

Figure 36 - a) Hardness measuring machine (EMCO® Test M4U-075), b) microhardness measuring device, c) hardness measurements diagram.

In order to better evaluate the effects of machining on the surfaces, in particular the additive manufacturing surface, the specimens were subjected to residual stress measurements. In this analysis, the Taguchi method was also implemented. The residual stresses in the samples were measured by x-ray diffraction (XRD) with Cr-Kα radiation (refer to Figure 37 b)). The measurements were conducted in the component's surface machining feed direction and on the direction perpendicular to machining direction.

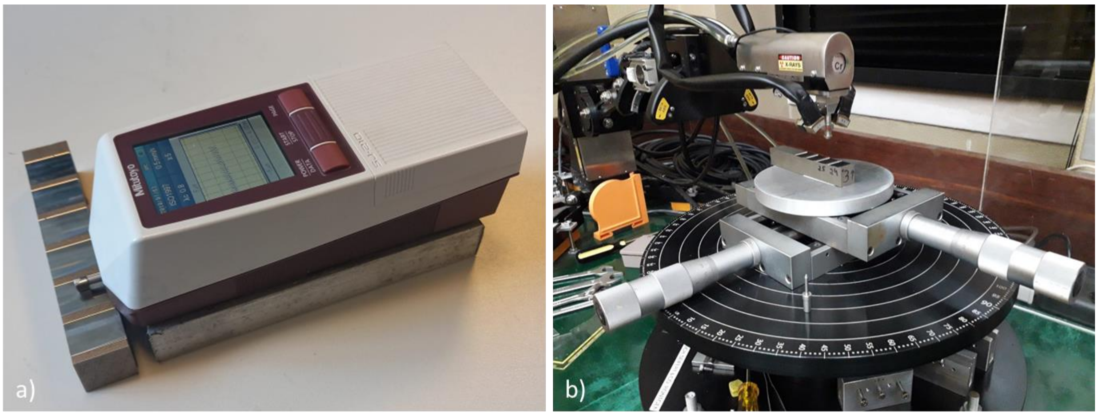

Figure 37 - a) Roughness evaluation with MITUTOYO Surftest SJ-210, b) residual stress measurement by x-ray diffraction (XRD).

3.2. Milling tests

3.2.1. Experimental setup

The experimental milling tests were performed in order to evaluate the differences in the machinability of the conventional and additive manufactured 18Ni300 steel. The experimental tests were conducted with a rotating dynamometer to measure the forces and torques during cutting. The equipment used was the Kistler Rotating Cutting Force Dynamometer (RCD), Type 9170A, which is shown in Figure 38 a).

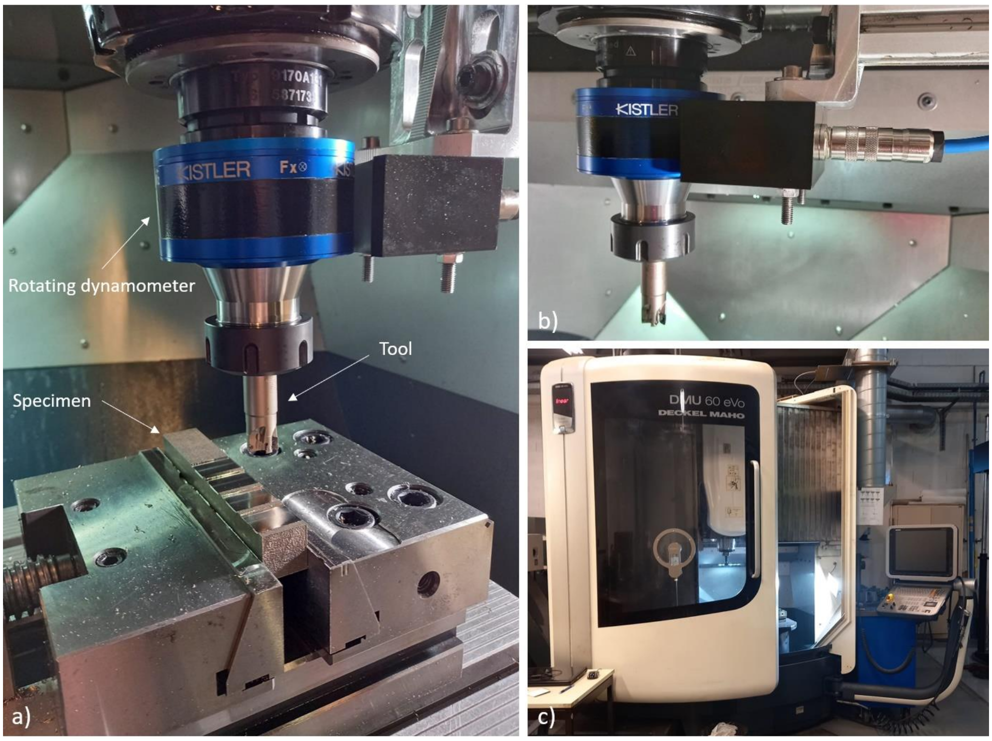

Figure 38 - a) and b) Experimental setup with Kistler Rotating Cutting Force Dynamometer Type 9170 A, c) DMG Mori DMU 60 evo CNC used in the experimental tests.

The experimental milling campaign was carried out in INEGI facilities. A 5-axis CNC machine was used to conduct the tests (DMG Mori DMU 60 evo), as shown in Figure 38 c). The piezoelectric rotating dynamometer was installed in the spindle head of the CNC machine following the manufacturer's recommendations. In order to convert the signal from the dynamometer and record the data from the tests, a charge amplifier (Kistler 5070A) connected to a computer with a data acquisition system (Kistler USB DAQ System Type 5697A1) was used (refer to Figure 39). A 5 kHz data sampling rate was used in the experimental campaign and the data was further analysed with Dynoware software, specific for machining.

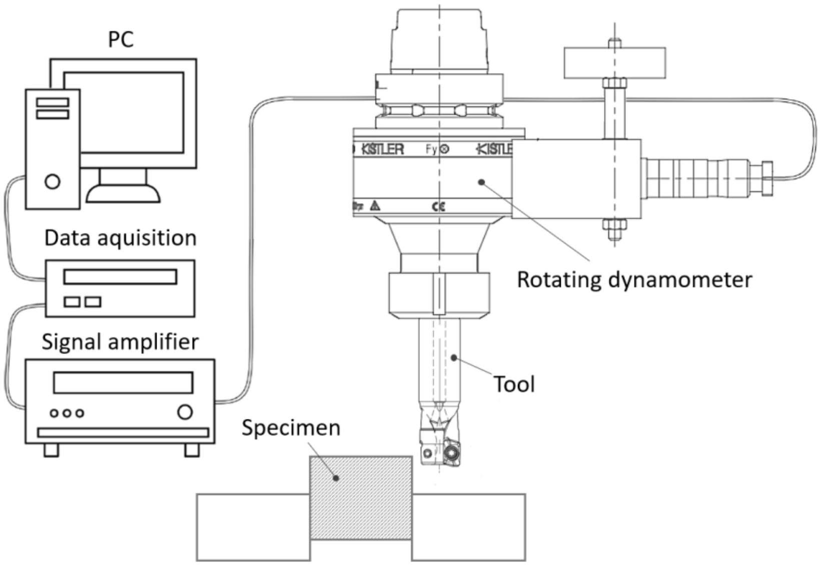

Figure 39 - Experimental setup illustration of apparatus.

In the milling tests, a similar cutting insert used in previous works on the MAMTool project was used to allow the comparison of results. This cutting insert was selected with the help and expertise of Palbit S.A. to perform the tests in the 18Ni300 steel. The selection was for a hard metal insert designed with chip-breaker (XPET 060204 PDER-LP) with AlTiN PVD coating grade (PH7920). The insert geometry and dimensions are shown in Figure 40 c) and d). The milling shank supplied by Palbit S.A. and was chosen based on the cutting insert, being a 4-insert cutter (LINE PRO 016E20090-04-04-016090). The cutting tool geometry and dimensions are shown in Figure 40 a) and b). In order to simplify the analysis of the milling operations and acquire a clear image of influences of the changes in the cutting parameters, only one cutting insert was used.

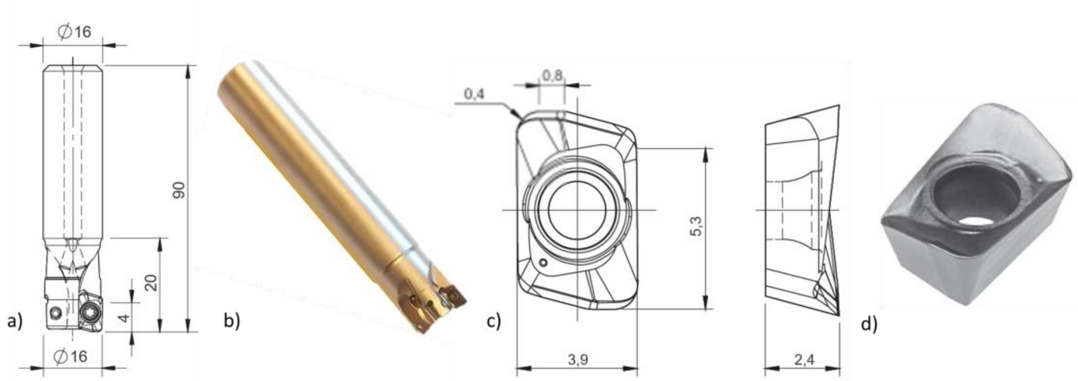

Figure 40 - a) and b) Milling shank geometry and dimensions, c) and d) cutting insert geometry and dimensions.

In Figure 41, a general scheme of the tests performed is shown, as well as the forces measured during cutting with rotating cutting force dynamometer. The forces obtained were the result of a moving referential, which rotated together with the tool, offset at an angle θ from the cutting insert.

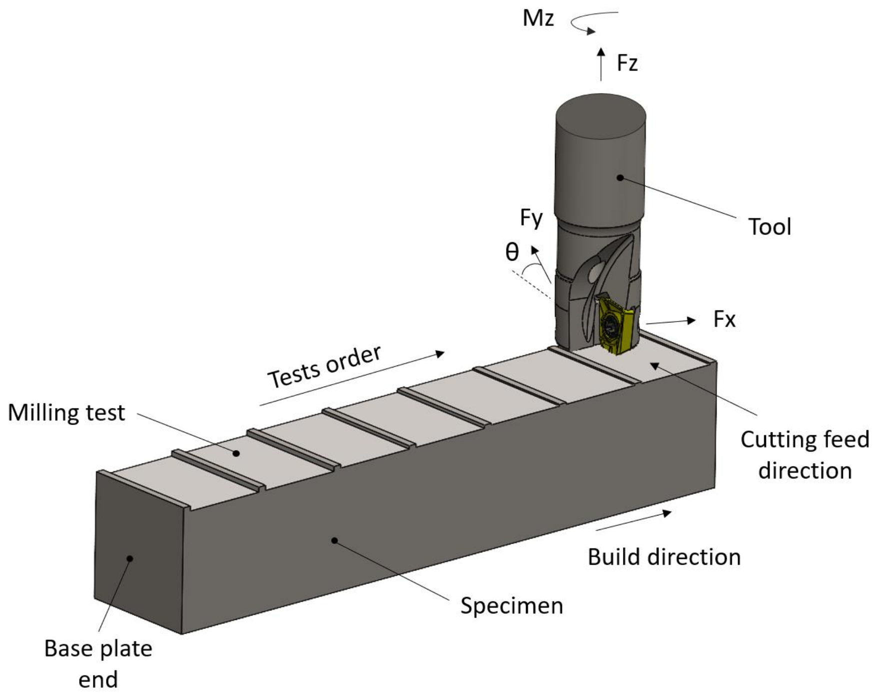

Figure 41 - Milling tests illustration setup and acquired loads labelling.

In the machinability studies of Silva et al. [78] and Laínho [79], a wide range of parameters in turning and milling tests of maraging steel was used (depths of cut between 0.1 and 0.5 mm, feeds between 0.05 and 0.2 mm/rev, and cutting speeds between 55 and 150 m/min). In machinability studies of AM maraging steel of Oliveira et al. [70, 73], feeds of 0.02 and 0.08 mm/tooth, and cutting speeds between 150 and 350 m/min were used. Other studies [59, 60, 71] covered different cutting speeds in milling of AM maraging steels, from 80 to 350 m/min. In order to attain a comprehensive set of experimental milling trials, the parameters of cutting speed, depth of cut and feed rate were varied three times each, with values of 80, 200, 320 m/min, 0.2, 0.4, 0.6 mm, and 0.05, 0.1, 0.2 mm/rev, respectively, as could be seen in Table 5. All combinations of these parameters were tested for the two chosen materials with two repetitions each. Each cutting insert was changed at each change of cutting speed (for each repetition and for each material - 9 tests in the same sequence, combinations of 3 feed values and 3 depth-of-cut values). The milling operations were spaced in order to optimise the available space in each specimen, without interfering between successive passes.

Table 5 - Cutting parameters combinations used in milling tests (3 parameters x 3 levels).

Cutting speed [m/min]	Depth of cut [mm]	Feed [mm/rev]
80	0.2	0.05
		0.1
		0.2
	0.4	0.05
		0.1
		0.2
	0.6	0.05
		0.1
		0.2
200	0.2	0.05
		0.1
		0.2
	0.4	0.05
		0.1
		0.2
	0.6	0.05
		0.1
		0.2
320	0.2	0.05
		0.1
		0.2
	0.4	0.05
		0.1
		0.2
	0.6	0.05
		0.1
		0.2

3.3. Simulation procedures

Simulations of the milling process were carried out using the DEFORM software in view to obtain a numerical model that allows for optimisation and prediction of results as well as better understanding of the process.

3.3.1. Constitutive model

The model developed by Silva [18], shown in Equation (3.1) with the respective parameters in Table 6, has been employed in this study, where the AM 18Ni300 maraging steel was properly characterised in physical, metallurgical, and mechanical terms. This model uses the Swift-Voce law with a decoupled viscoplastic term.

$$\sigma = \left[0.2\left[950\left(1+\varepsilon_p\right)^{-0.7}\right] + (1-0.2)\times 887.5 - 362.5\left(1-e^{-170\varepsilon_p}\right)\right]\left(1+0.05ln\frac{\dot{\varepsilon}}{\dot{\varepsilon}_0}\right) \quad (3.1)$$

Table 6 - Swift-Voce equation parameters for hardening curves of the AM material.

K [MPa]	ε_0	n	k_0 [MPa]	Q [MPa]	β_v	α	C
950	1	-0.7	887.5	362.5	170	0.2	0.05

This model was calibrated based on a tribo-mechanical methodology [80] in which compression tests in different conditions (from quasi-static to very high strain-rate) were performed. The force displacement response includes the overall flow stress behaviour, thus, including, the generated heat from plastic deformation. For that reason, a temperature related term was not included in this model. This concept assumes that thermal softening and visco-hardening are regarded as a coupled effect. Since the heat generated in cutting is essentially evacuated through the chip (not raising the temperature much near the shear plane), this temperature gradient is not sufficiently significant for major temperature changes in the properties of the material being cut [81]. The material properties obtained by Silva as shown in Table 7.

Table 7 - Material properties of AM 18Ni300 used in the numerical model of Silva [82].

Material properties	Value/Equation
Young's modulus [GPa]	$E = 190$
Friction	$\mu = 0.3\ (Coulomb)$
Fracture energy [mJ/mm³]	$G_f = 10$
Density [kg/m^3]	$\rho = 8033$
Conductivity [W m^{-1} C^{-1}]	$\lambda = 0.0206T + 15.4$
Specific heat [J/kg^{-1} $°C^{-1}$]	$c_p = 0.374T + 437.3$
Thermal expansion [C^{-1}]	$\alpha_{inst} = 0.0038T + 9.722$

The combined Swift-Voce model accurately described the constitutive behaviour of maraging steel for distinct pressure conditions in the plastic deformation of multiaxial fracture specimens. In Figure 42, the experimental quasi-static compression results obtained by Silva [18] are compared with the material model quasi-static flow curve, also obtained by Silva. On the one hand, Swift power law hardening is used to model the initial yielding and saturation of Voce for the higher consequent stresses. Through the tests performed, it was possible to see that the assumption of isotropic plastic behaviour in the material was plausible in AM maraging steel.

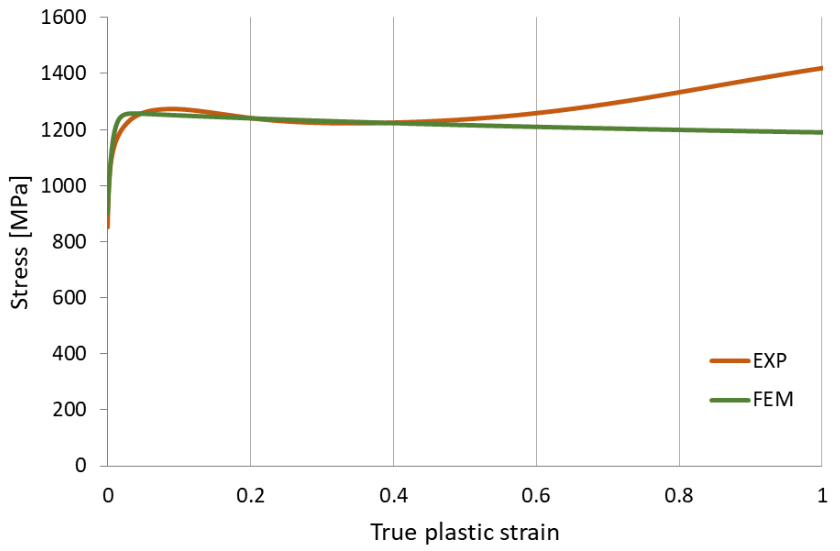

Figure 42 - Quasi-static numerical and experimental curves obtained by Silva [18].

3.3.2. Software

The software used in the milling simulations was the DEFORM software that allows the analysis and simulation of processes such as metal forming, machining, among others. This software has a discretization strategy based on the implicit Lagrangian formulation and includes an automatic remeshing routine (Automatic Mesh Generation - AMG), that generates a new FEM mesh on the workpiece whenever excessively distorted elements occur, as shown in Figure 43. Data interpolation from the old mesh to the new one is automatically performed, in order to avoid highly distorted mesh topologies, which despite the high computational cost, as mentioned in Section 2.1.4.4, allows a good description, without loss of information, of the process to be simulated. Although it also has as a possibility the use of a Eulerian approach, the proposed work aims at chip morphology prediction, which is not possible with Eulerian formulation. Still, due to the absence of a damage model, chip serration is not predicted.

3.3.3. Milling model

The milling model uses the implicit Lagrangian formulation, employed by the DEFORM software. The element size of the main mesh as well as of the secondary mesh (definition of the ratio between the two) was determined through mesh sensitivity analysis (refer to Figure 44). The same was performed for the tool's mesh. The milling model attempts to replicate the conditions of the model used by Silva [18], which was executed in Abaqus CAE software using a coupled temperature-displacement (explicit) formulation with a Lagrangian approach. The use of an automatic remeshing routine also differs from Silva's model, where the chip separation was applied through element deletion, using a damage criterion.

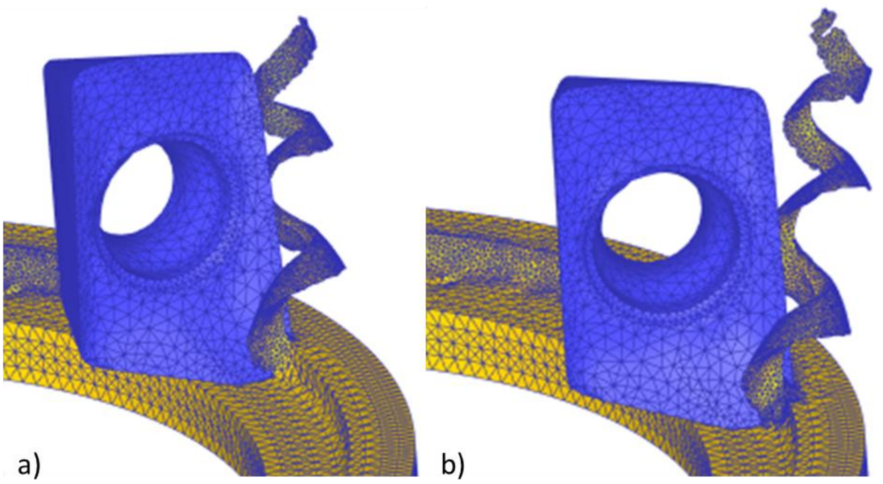

Figure 43 - Example of the remeshing procedure during the executed simulations.

In addition, a study of the influence of friction on the simulations performed in the software was carried out. The flow curves of the model were defined in order to be compatible with the experimental studies and the turning simulations performed in the Abaqus CAE software by Silva [18]. The boundary conditions were defined according to the default settings of the software that incorporates a pre-established model for milling simulations. The tool material, tungsten carbide (WC), was chosen through the library provided by the software.

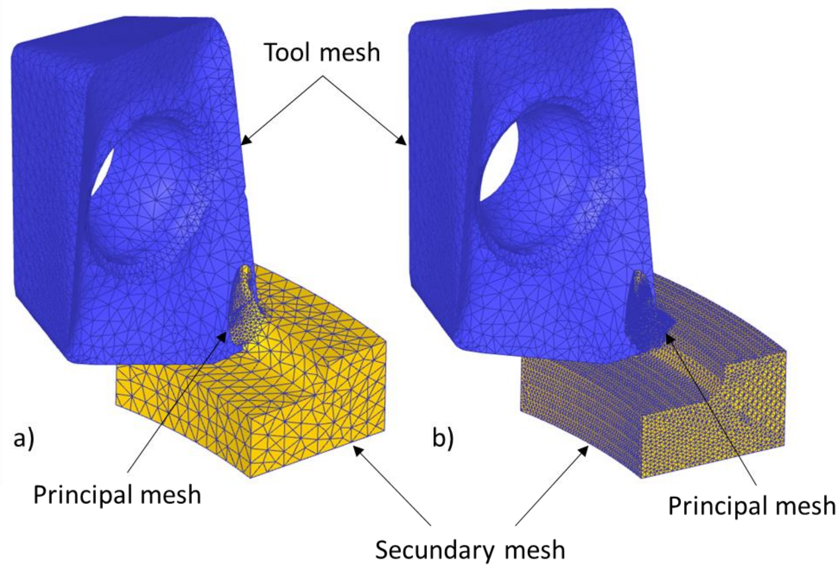

Figure 44 - Different tested less (a) and more (b) refined meshes.

4. Results and discussion

In the present chapter, the results obtained from the previously described experimental tests are shown. A detailed analysis of the measured loads, chip morphology, residual stresses, and characteristics of the cut material, such as the surface roughness and hardness is provided in order to show the influences of the cutting parameters. In addition, an analysis of the milling simulations conducted is also provided. Whenever possible, the results have been compared with those of other works in literature in an attempt to obtain a better analysis.

4.1. Material characterisation

Regarding the characterisation of the material, the chemical composition, microstructure, hardness, and roughness analyses allowed a better understanding of the materials to be tested, as shown in the following sections.

4.1.1. Chemical analysis

The measured chemical compositions of the two materials (AM vs. CM) are shown in Table 8, where a comparison with the respective standard is also made.

Table 8 - Chemical composition (wt%) of 18Ni300 steels with respective reference values.

		Ni	**Co**	**Mo**	**Ti**	**Si**	**Mn**	**C**	**P**	**S**
MIL-S-46850D (1986)	min	18.0	8.5	4.6	0.5	-	-	-	-	-
	max	19.0	9.5	5.2	0.8	0.10	0.10	0.03	0.01	0.01
AM material		18.80	8.84	5.15	0.65	0.05	0.03	0.02	<0.001	<0.001
CM material		18.93	8.92	4.88	0.77	0.02	0.03	0.01	<0.001	<0.001

Both materials comply with the respective standard and show no significant differences between them. The low carbon content of the steels presented is highlighted, which favours their good weldability, which is a good attribute for additive manufacturing. The high percentage of nickel is one of the distinctive characteristics of these materials which influences their microstructure. The martensite in these alloys is a solid solution of Ni and martensitic iron. The structure of the martensite formed by Ni is practically the same as that of martensitic steels obtained during classical quenching [83].

4.1.2. Metallographic analysis and relative density

The microstructure of the additively manufactured 18Ni300 maraging steel is revealed through chemically etched samples and presented in Figure 45 a) and b) for parallel and perpendicular to build directions, respectively. These results are very much in line with the metallographic samples found in literature, showing a cross section of the molten pools with a curved structure in the parallel direction and laser tracks in the perpendicular to the build direction, as is the case of the work developed by Mutua et al. [58] shown in Figure 28.

It is important to note that while chemical etching seems to emphasize grain morphology, electrolytical etching highlights the typical macrostructure of AM, such as the melt pools and laser tracks. Further microstructural defects typical of AM technology could be observed in the micrographs. The presence of small spherical porosity and irregular shaped voids, preferentially located between molten pools, (refer to Figure 45 a) and b)) that appears to be related to gas entrapment during layer building, and cracks across a crystallized grain could be observed [58, 60]. In Figure 45 c), it is possible to observe the microstructure of maraging steel produced by the conventional process, where the characteristic lath and plate martensite is observed [84]. Regarding the relative density measured, after the various measurements, an average of 99.3% was obtained, which is in line with that specified by the manufacturer. This high value is in line with the literature for parts with better mechanical properties. In Figure 45 d), it is presented a metallographic image sample of the AM steel without etching for a simpler porosity measurement. The voids do not seem to have any associated pattern.

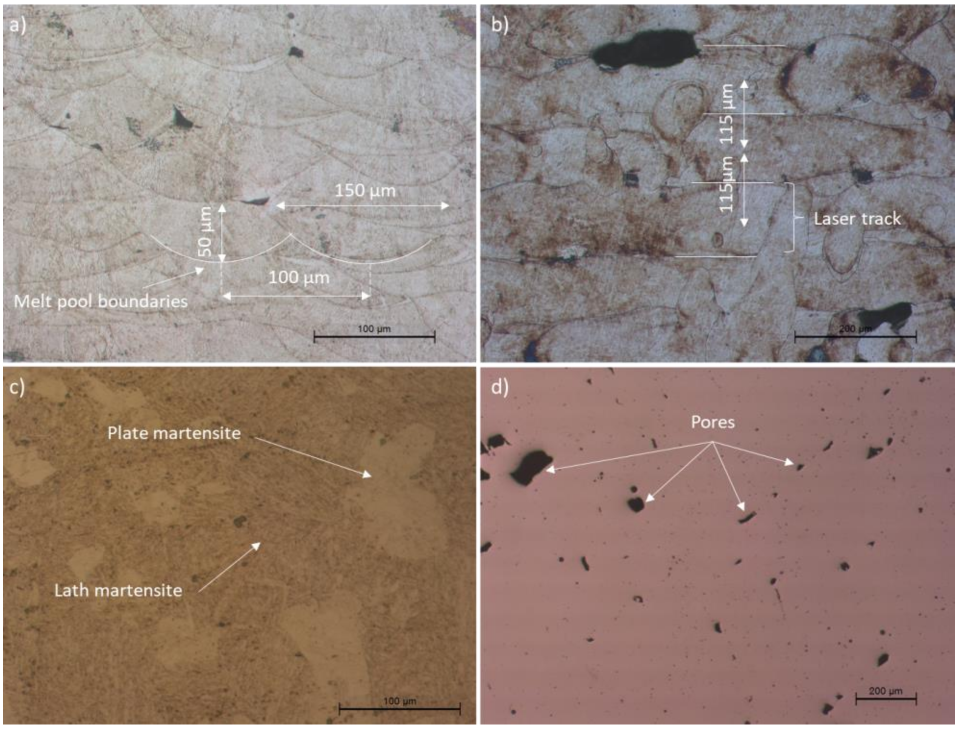

Figure 45 - Electrolytically etched metallographic samples of AM 18Ni300 in parallel (a) and in perpendicular to build direction (b); chemically etched samples of CM 18Ni300 (c); unetched metallographic sample showing voids occurrence in AM 18Ni300 (d).

4.1.3. Surface and hardness analysis

Regarding the measured roughness (refer to Table 9), the material produced by additive manufacturing presents typical roughness values of AM, as observed in the literature [58-60] for maraging steels. The high roughness, apart from being caused by the interface between different layers along the specimen, is a result of the non-complete melting of powders of the additive material that are trapped on the surface, as shown in Figure 46. The conventional material has a low roughness due to the grinding operation that the specimens were subjected to before the machining tests in order to have the same dimensions as the AM specimens.

Table 9 - Roughness measurements averages ($\bar{x}$) and standard deviation (σ) of Ra, Rz, and Rz max parameters in as-built AM condition and CM after grinding (values in µm).

	Ra		**Rz**		**Rz max**	
	$\bar{x}$	σ	$\bar{x}$	σ	$\bar{x}$	σ
AM	3.905	0.547	25.920	4.087	33.517	5.291
CM	0.417	0.006	3.353	0.663	3.922	0.712

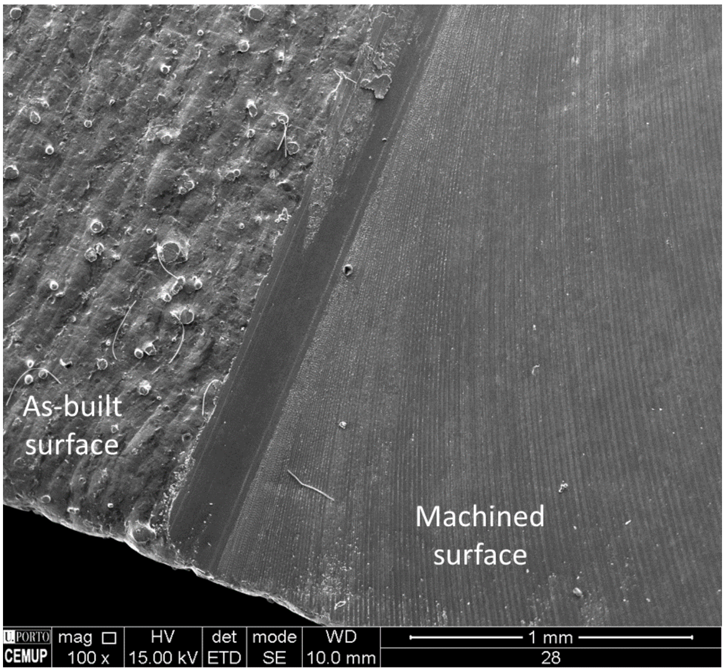

Figure 46 - SEM image highlighting the difference between an AM and a machined surface.

With regards to the hardness measured in the two materials (refer to Table 10), a higher value is observed in the AM material (to 16%), which agrees with the literature reviewed. Since hardness is an indirect measure of a material's strength, the finer microstructure of additive manufacturing materials due to high cooling rates leads to higher mechanical strength and consequently higher hardness. This higher strength was also observed by Silva [18] when performing compression tests on AM and CM maraging steels.

Table 10 - Hardness measurements (HV) of 18Ni300 steel in both CM and AM metallurgical conditions

Measurement	**1**	**2**	**3**	$\bar{x}$
AM	374	384	372	377
CM	325	323	325	324

4.2. Experimental milling tests results

After the execution of the experimental milling tests and consequent data collection, the forces involved, specific cutting pressures, roughness, surface states, hardness and residual stresses were analysed and discussed as shown in subsections below.

4.2.1. Cutting forces

The forces measurements shown a clear pattern, characteristic of a milling operation, as shown in Figure 47. The analysis was focused on the tool full engagement zone since it represents a more realistic view of an industrial and longer operation. The main force analysed was the cutting force as it is the main parameter influencing the power required by the cutting process. It is possible to observe an oscillatory load pattern resulting from the fact that cutting is performed with only one insert, and therefore only half of each cutter revolution cuts material. The values of the analysed forces resulted from an average of maximum points in the full engagement zone.

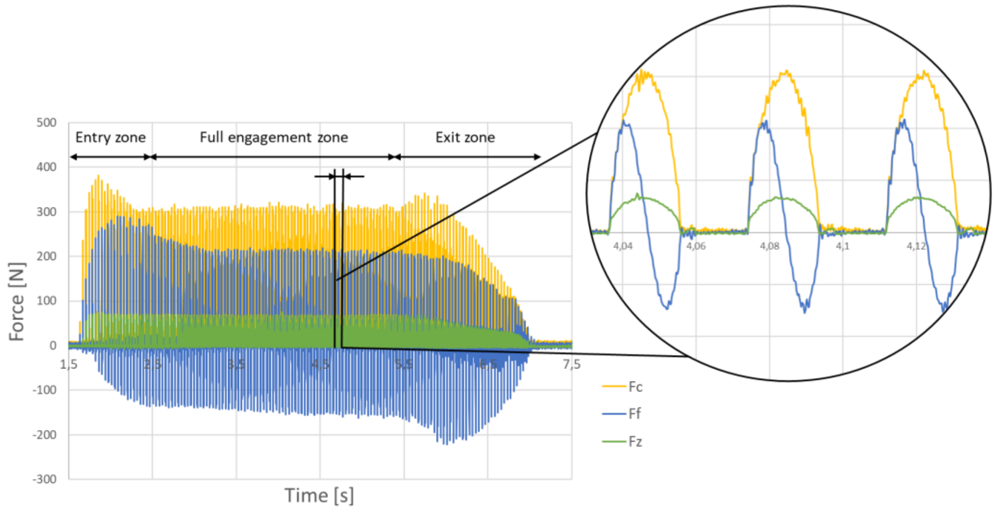

Figure 47 - Overview of the conducted milling tests.

Experimental correlations between the feed force (F_f) and the force on the z-axis (F_z) with the cutting force (F_c) are shown in Figure 48 a) for both CM and AM 18Ni300 stainless steels. Maximum values for the maximum chip thickness are plotted in that graph. It is clear that there is a linear increase with increasing cutting force of the force components F_f and F_z, which is in line with the geometric relationship between the operational parameters of the machining process and the vector components of the cutting loads. A good similarity between the two materials is also observed. These results allow a more simplified and focused analysis of the cutting force, and the influences of the cutting parameters will have similar trends in all the forces presented.

In Figure 48 b), the influence of the feed rate and depth of cut in the cutting force, for the two materials is shown. An increase in force is observed for both feed increase and depth of cut increase, which is in line with the results works of other authors [50, 78]. This effect is associated with the increase of the undeformed chip thickness and width, which represents more material to be removed during a single rotation of the mill, resulting in a larger energy requirement for the plastic deformation of the material.

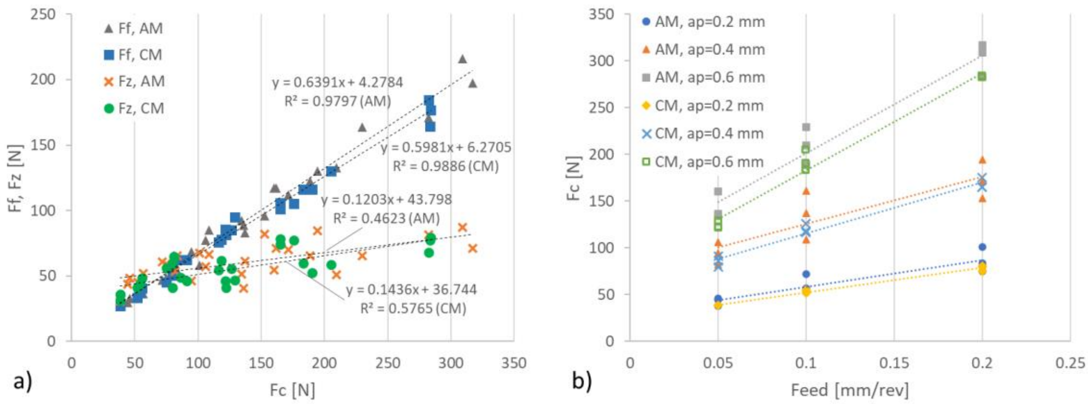

Figure 48 - a) Experimental correlation between Fc and Ff, Fz; b) Cutting force in function of feed, for different depths of cut and materials.

4.2.2. Specific cutting pressure

By observing the collected data (refe, it was possible to immediately observe a greater influence of the feed in the specific cutting pressure (Kc) when compared with the other parameters. Figure 49 a) shows the overall evolution of the specific cutting pressure, as a function of the feed, *f*. The exponential increase in Kc for small feeds agrees with machining studies performed by other authors [85, 86]. Since for the smallest feeds, the chip thickness is greatly reduced (≈ 0.04 mm), as observed in Figure 50, there is a significant compression effect on the workpiece, known as ploughing effect, that does not contribute to cutting. In the tool cutting edge radius area (refer to Figure 50), there is an action of a constant force responsible only for deforming workpiece material and does not contribute to chip removal. For large magnitudes of uncut chip thickness, this force is proportionally small compared to the total shear force, however, for small uncut chip thickness, the forces resulting from the ploughing effect could be of the same magnitude as the shear forces, and cannot be neglected, causing the specific cutting pressure to increase in a non-linear way [85, 87]. In theory, in the limit where the tool action does not produce any chips, a force resulting from size effects would continue to be recorded, which would result in the specific cutting pressure recorded being infinite.

In Figure 49 b), a comparison of the two machined materials is shown and it could be observed that the steel produced by additive manufacturing presents in general a higher specific cutting pressure for the same feeds. This difference is more noticeable for the smaller feeds, although in terms of tendency, this does not exceed 10%. These results are in line with those found by Silva [18] and reflect a higher mechanical strength of the AM materials, which was observed in the uniaxial compression tests hardness measurements (around 16%) conducted.

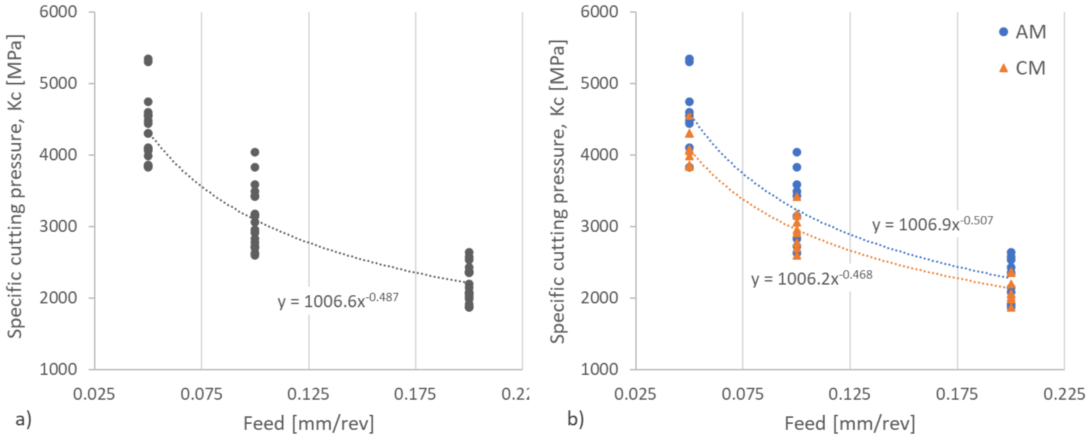

Figure 49 - Specific cutting pressure, Kc, in function of feed, f, for: a) all the tests, b) comparison of AM and CM 18Ni300 steel.

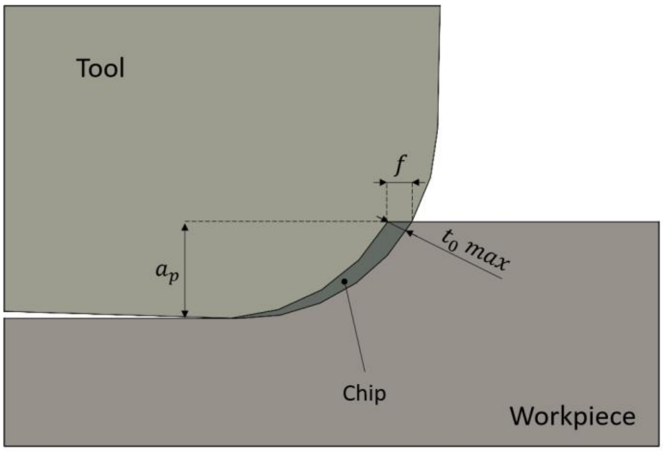

Figure 50 - Chip geometry for ap = 0.2 mm and f = 0.05 mm/rev.

Figure 51 shows the evolution of specific cutting pressure in function of feed for the different depths of cut (a) and cutting speeds (b) for the two machined materials. It is possible to observe an increase in the specific cutting pressure when higher depths of cut were used. This increase is more noticeable in Figure 52, where only one material is compared each time for a clear analysis. This increase could also be result of size effects since as the area of the chip increases, more material is subjected to ploughing phenomenon [88].

When a closer look is taken in Figure 53, it seems that a higher cutting speed favours higher specific cutting pressures, however, this effect is of minimal significance. With the increase in cutting speed, the material is subjected to an increase in thermal softening during milling, outer balancing the strain rate hardening effects, which could answer this trend, as registered by Fortunato et al. [59].

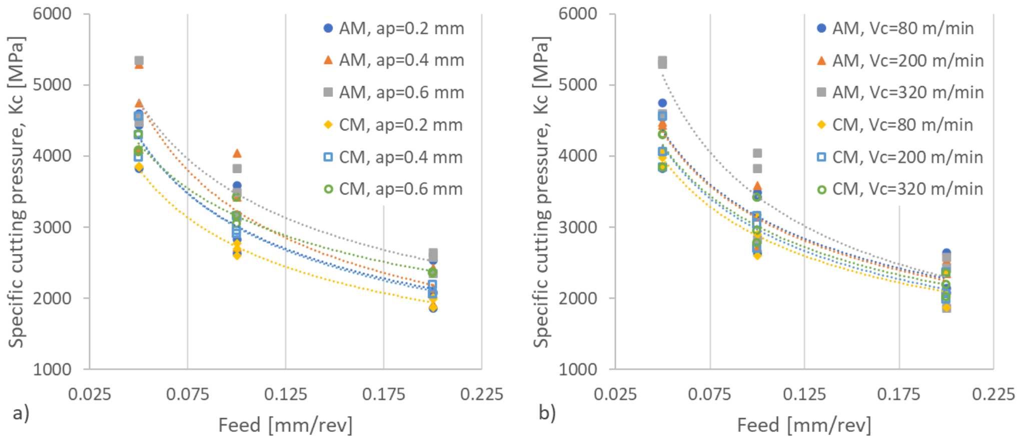

Figure 51 - Specific cutting pressure, Kc, in function of feed, f, for: a) different depths of cut, ap, and b) cutting speeds, vc.

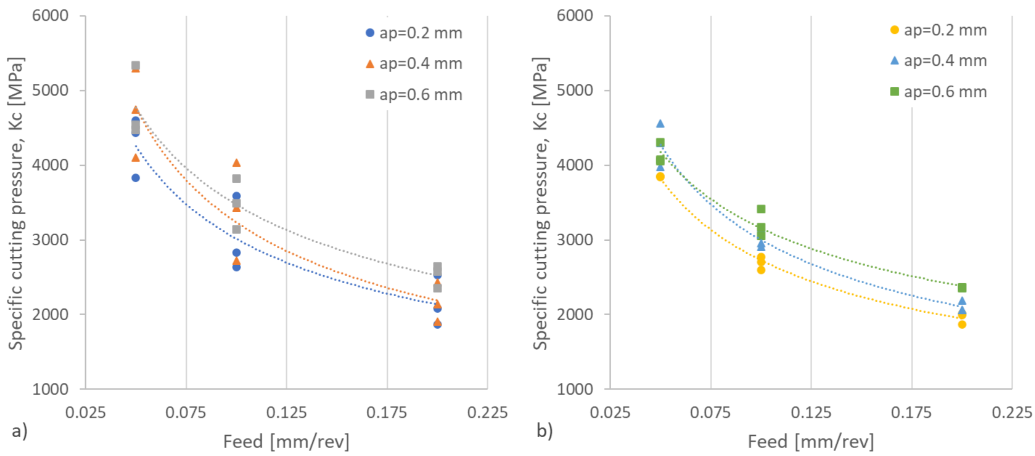

Figure 52 - Specific cutting pressure, Kc, in function of feed, f, for different depths of cut, ap, for: a) AM, b) CM.

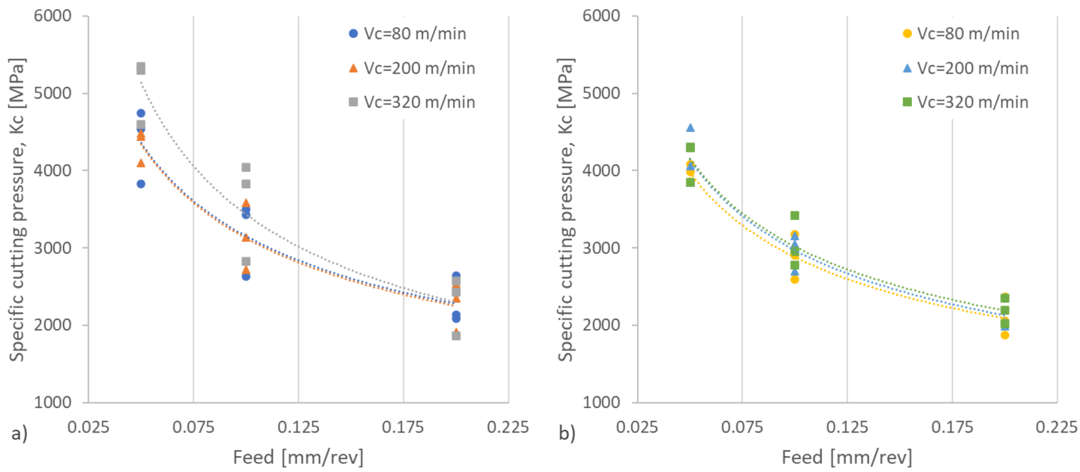

Figure 53 - Specific cutting pressure, Kc, in function of feed, f, for different cutting speeds, vc, for: a) AM, b) CM.

In an attempt to clarify the influence of every parameter in the specific cutting pressure of this experimental tests, an average Kc was calculated for every cutting parameter. The results are shown in Figure 54 a), b), c) and d) and corroborate the previous conclusions. In Figure 54 e) is shown the relative weight of influence of each parameter calculated from the difference between the extreme values of the mean values for each parameter (Note: When the influence of one parameter is investigated the Kc is computed as the average value of all other parameters). As expected, the feed is the parameter that most influences the specific cutting pressures and its influence is five times greater than that recorded for the second most influential parameter, the depth of cut.

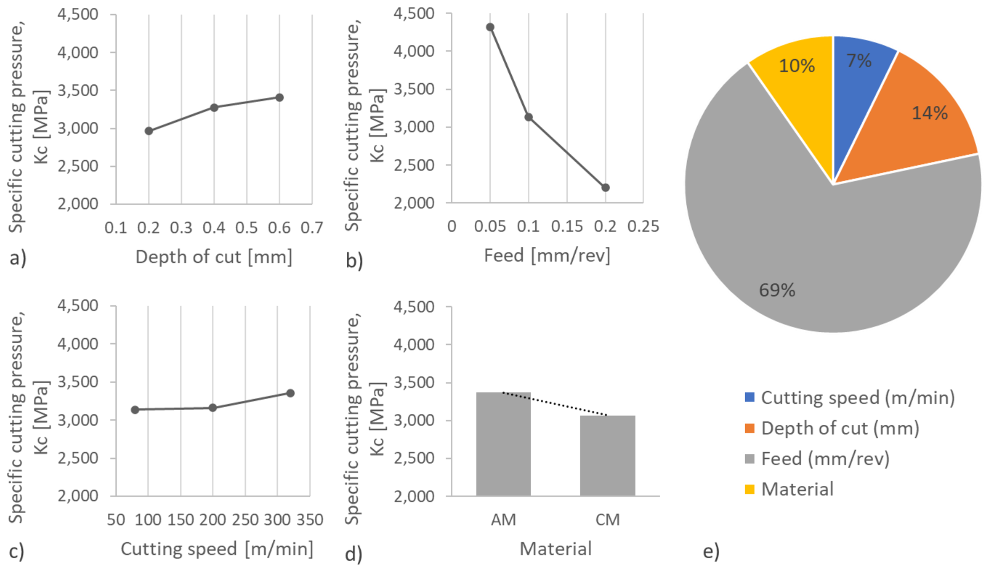

Figure 54 - Variation of specific cutting pressure, Kc, in function of: a) depth of cut, b) feed, c) cutting speed, d) material; e) influence of the different parameters in the specific cutting pressure.

Figure 55 shows a comparison between different specific cutting pressure values of maraging steel [78, 79]. It should be noted that all studies used the same cutting insert and WC grade. Although Laínho [79], Couto and Silva et al. [78] focused on turning tests, the estimated specific cutting pressures presents a good agreement with the obtained results (milling operations). The relative differences may be the result of natural differences between different material batch and different setups used in the experimental tests.

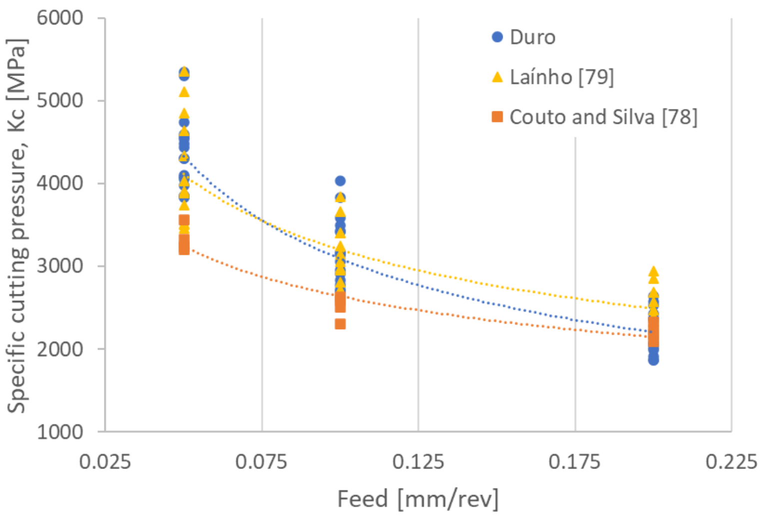

Figure 55 - Comparison between the results of specific cutting pressure of this work and the work of Laínho [79], Couto and Silva et al. [78].

4.2.3. Surface roughness

As mentioned in Section 3.1.2, measurements of Ra, Rz and Rz max were carried out. In order to simplify the analysis, the relationship between the Ra parameter and the other two was observed. In Figure 56, it is possible to observe a linear variation of the parameters Rz and Rz max with Ra, as expected. The Rz max parameter presents results with greater dispersion, which arise from the Rz roughness parameter definition. In this way, emphasis will be given to the Ra parameter, since the others seem to present similar tendencies with the variation of that (Ra) parameter.

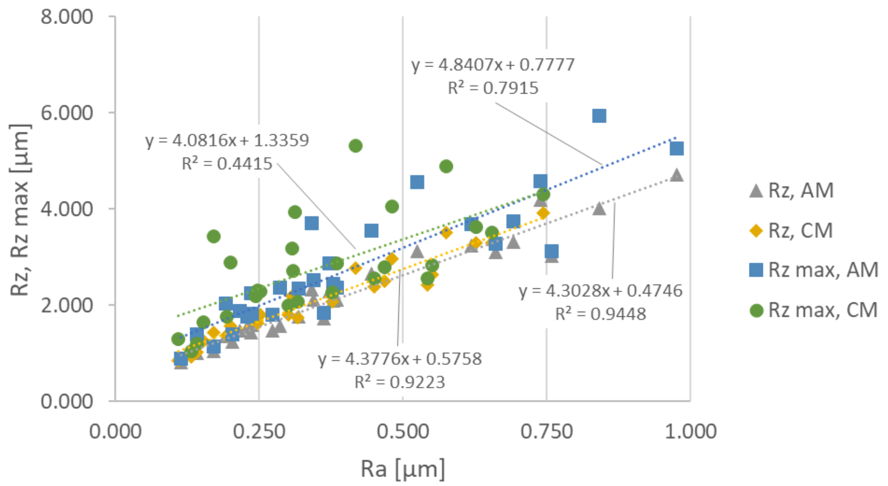

Figure 56 - Experimental correlation between Ra and Rz, Rz max.

When the influence of the different parameters on the roughness, Ra, is analysed, the greatest and strongest influence of the feed is evident, although it is not as decisive as what as verified for the specific cutting pressure. The surface roughness of the machined samples shows considerable improvement, when compared with the as-built AM surfaces. In Figure 57, a linear increase in Ra with feed is observable. This effect is mainly due to the geometry of the various insert passages. Since the tool always has a clearance angle greater than 0°, the contact between the tool and workpiece will not correspond to a flat surface, as shown in Figure 58. The radius between frontal and lateral cutting edges will also influence.

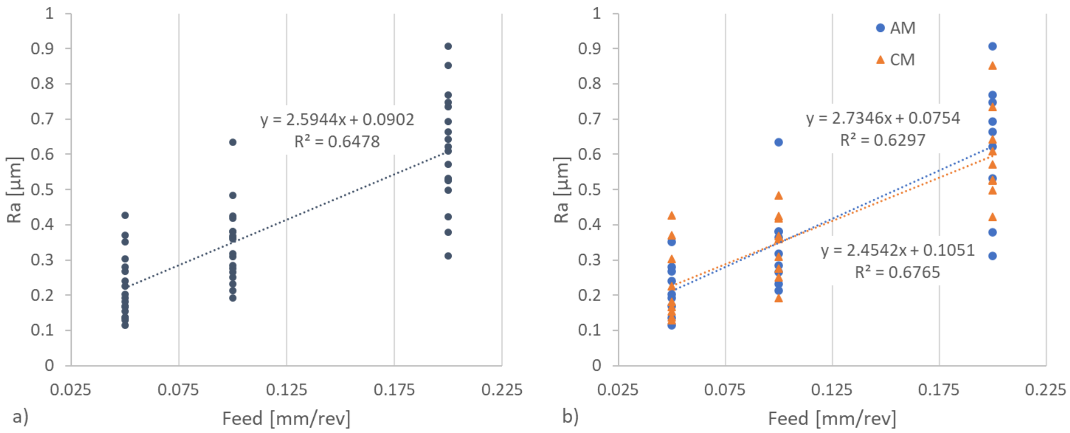

Figure 57 - Roughness, Ra, in function of feed, f, for: a) all the tests, b) the AM and CM 18Ni300 steel.

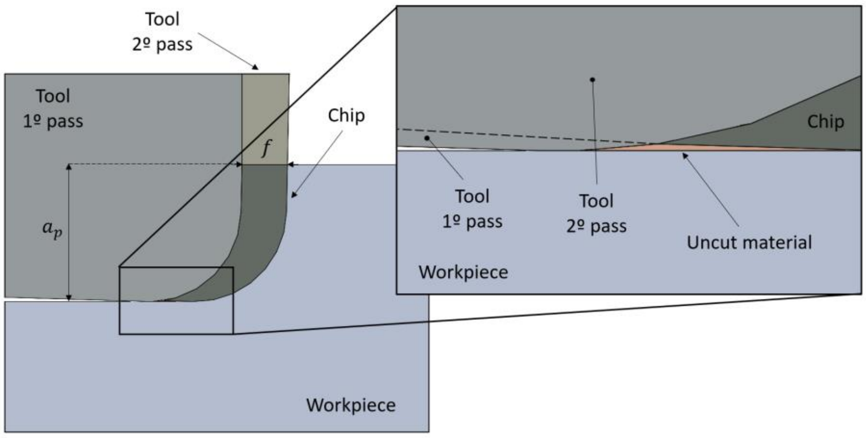

Figure 58 - Diagram of two successive passages of the cutting tool, for a_p = 0.6 mm and f = 0.2 mm/rev.

In Figure 59, the variation of roughness with feed for the different depths of cut (a) and cutting speeds (b) is shown. An increase of Ra with a_p is noted, being notorious when observing Figure 60. As stated by Subramanian et al. [89], the increase in depth of cut leads to an increase in volume of metal removed and an increase in contact area of workpiece which will favour the increase of vibration in cutting and wear of the tool. These effects lead to a coarser cut and consequently a higher roughness. Regarding the variation of the cutting speed, no significant influence is registered, as shown in Figure 61 for the two materials.

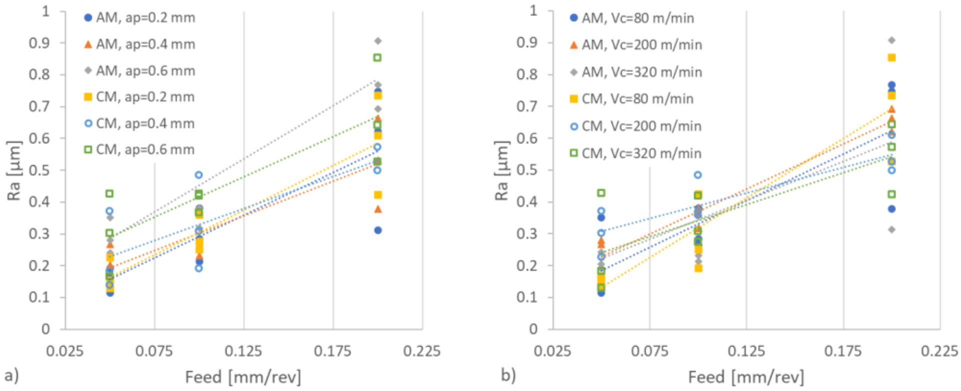

Figure 59 - Roughness, Ra, in function of feed, f, for: a) different depths of cut, a_p, and b) cutting speeds, v_c.

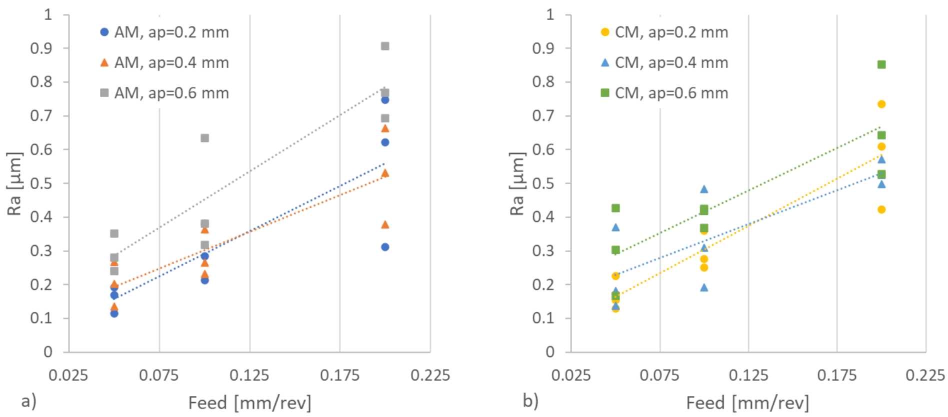

Figure 60 - Roughness, Ra, in function of feed, f, for different depths of cut, a_p, for: a) AM, b) CM.

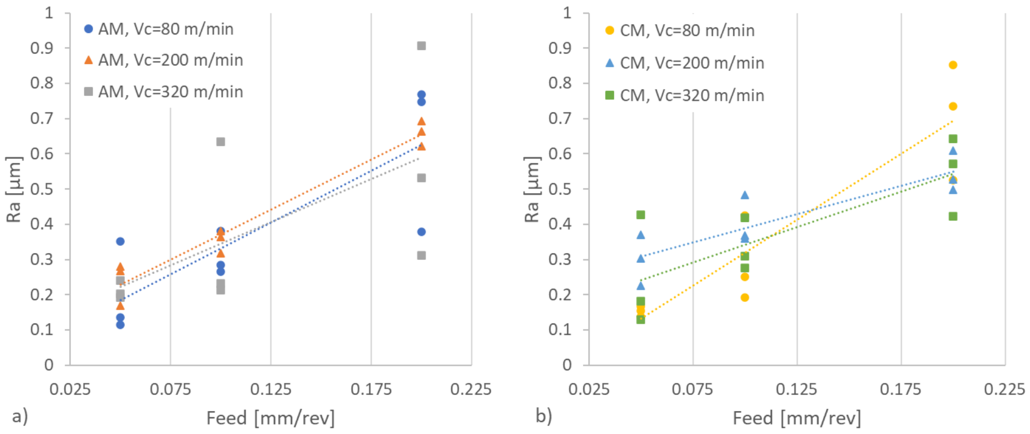

Figure 61 - Roughness, Ra, in function of feed, f, for different cutting speeds, v_c, for: a) AM, b) CM.

A similar analysis about the weight of each parameter as purposed for specific cutting pressure, was also conducted for surface roughness. The results are shown in Figure 62 a), b), c) and d) and corroborate the previous conclusions. In Figure 62 e) the relative weight of influence of each parameter is shown. This relative weight was calculated from the difference between the extreme average values, for each parameter. As expected, the feed is the parameter that most influences roughness, although the difference for the second most influential parameter, depth of cut, is not as pronounced as for the specific cutting pressure.

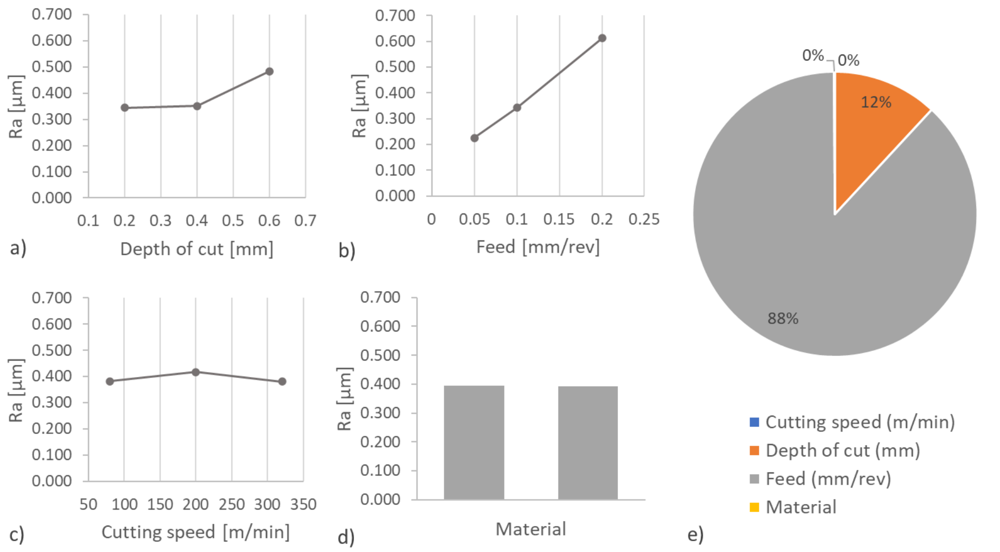

Figure 62 - Variation of roughness, Ra, in function of: a) depth of cut, b) feed, c) cutting speed, d) material; e) influence of the different parameters in the specific cutting pressure.

In Figure 63, a comparison of SEM images for the different feeds are shown. As expected, the surfaces show the characteristic pattern of milled surfaces, with arcs resulting from successive passes of the tool insert. Measurements made using ImageJ software evidence the feed values used in the experiments. When comparing Figure 63 c) and d), no significant differences were recorded between the surfaces of the additive and conventional manufactured materials, with the exception of the cross marks in (c) resulting from overlapping passes of the cutting insert.

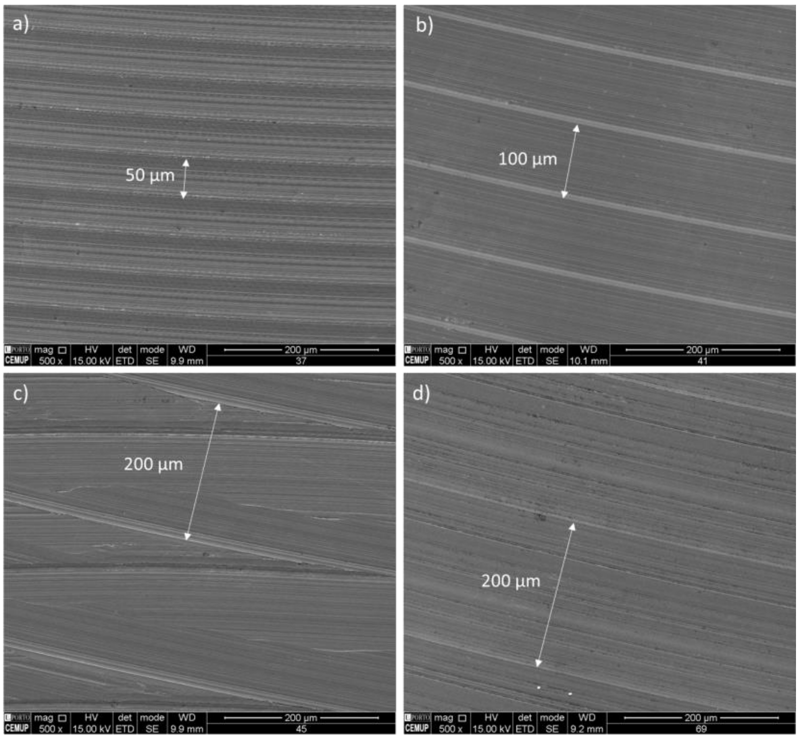

Figure 63 - Comparison of machined surfaces for different feeds and materials: a) f=0.05 mm/rev, AM; b) f=0.1 mm/rev, AM; c) f=0.2 mm/rev, AM; d) f=0.2 mm/rev, CM, for a cutting speed of 200 m/min.

In Figure 64 a), SEM images allow a closer look of the difference between an additive manufacturing surface in an as-built state and after machining. In Figure 64 b), the pattern shown results from the cutting insert passing first when cutting material (0º-180º) and then on a second pass, in the unused range (180º-360º).

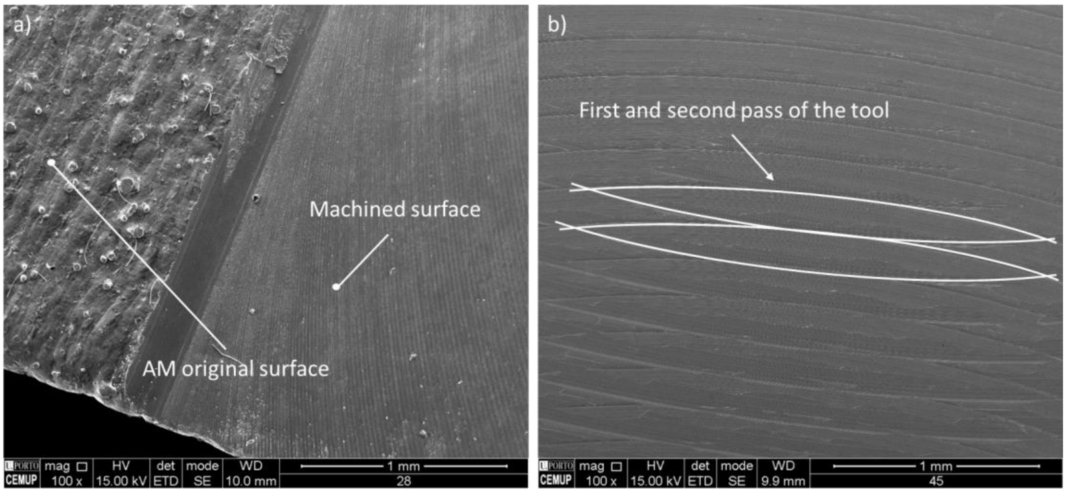

Figure 64 - a) Difference between a machined and an original AM surface, b) first and second pass of the tool registered on the surface.

The observation of the machined samples in SEM (refer to Figure 65) enabled a characterisation of the surface defects. In AM surfaces (a) some discontinuities were observed on the surfaces that result from the existence of porosity in this material. Another defect found was scratched surfaces (b), which may be a consequence of the tool-dragging of chips material formed during cutting. The existence of material adhered to the surface, either in the form of wider bands, or small fragments was also observed. Bands of adhered material reveal the formation of BUE in the cutting, which negatively affect surface roughness. Excess BUE melts into the surface material as the cutter passes through, giving rise to these bands.

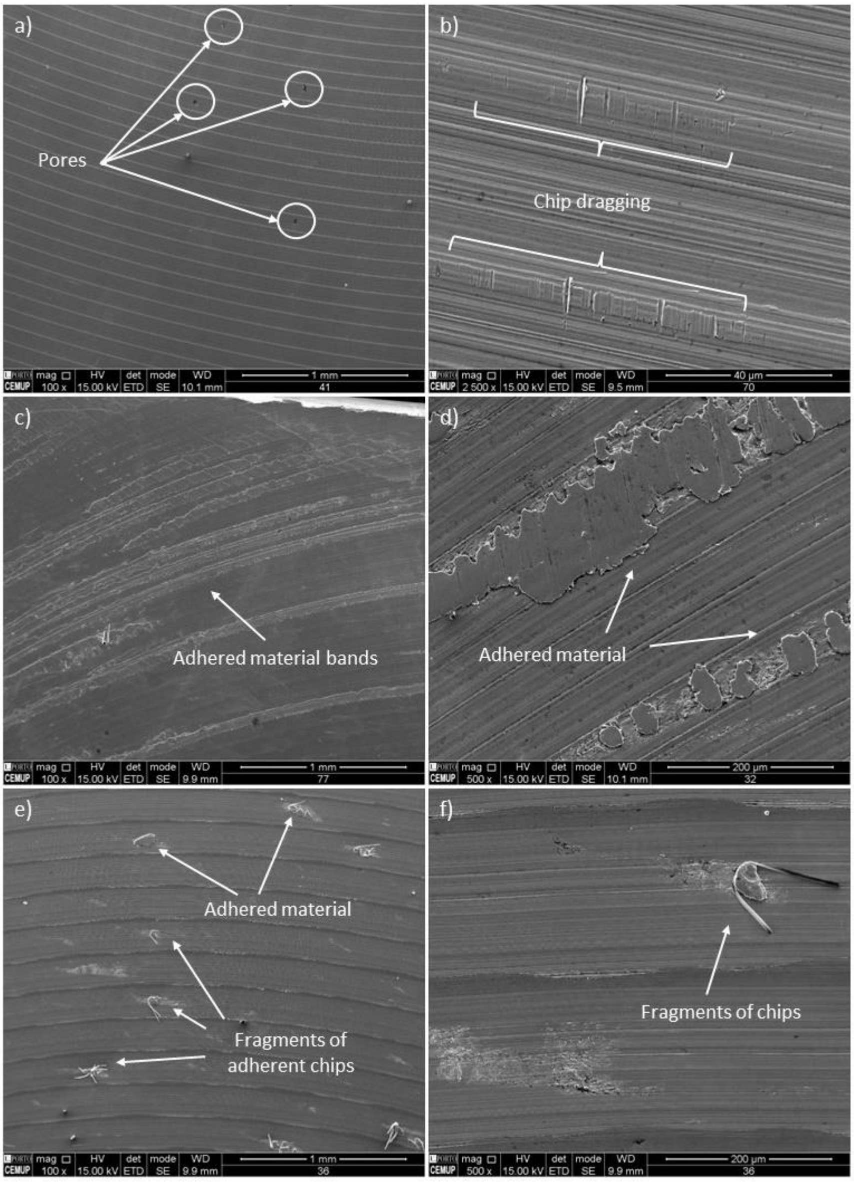

Figure 65 - Defects of the machined surfaces: a) pores, b) chip dragging, c) and d) adhered material, e) and f) fragments of chips.

4.2.4. Cutting insert wear tendencies

As described previously, each cutting insert was used for the single-speed tests (9 tests in the same sequence - combinations of 3 feed values and 3 depth-of-cut values). After observation at the SEM (refer to Figure 66), it is possible identify BUE and a coating deterioration at the insert tip. With a close observation and analysis using Energy-Dispersive X-ray Spectroscopy (EDS), the chemical compositions of the different zones were revealed, as shown in Figure 66. The Z3 zone correspond to the substrate material, which indicates a detachment (delamination) of the coating layer as a consequence of the abrasion between the workpiece material on the cutting edge region. The chemical composition of the Z2 zone revealed the presence of the 18Ni300 steel, indicating material adhesion of the workpiece to the tool rake surface forming the so-called BUE.

The Z1 zone and consequently the darkest area that can be observed corresponds to the rest of the insert that had not been altered either by BUE formation or by coating deterioration.

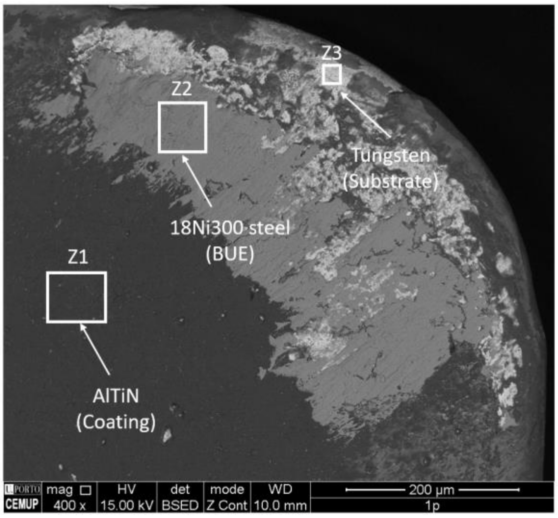

Figure 66 - Identification of different chemical compositions at the insert tip surface with EDS analysis, for v_c = 80 m/min, and AM material.

The cutting insert edges were observed for the different cutting speeds and for the different materials, as can be seen in the Figure 67, and the extent of change of the tip of the insert was measured. A decrease in BUE formation is observed with the increase of the cutting speed. These results are in accordance with the literature, as low cutting speeds promote adhesion of the workpiece material to the tool and compromise cutting efficiency due to insufficient heat generation and inefficient chip removal [5, 6]. Another effect registered is the greater extent of tool wear for higher cutting speeds, which could be the result of higher tool impact, thus leading to higher coating deterioration. Regarding the two machined materials, a more severe tool wear is registered when machining the conventional maraging steel for the same cutting conditions, which may be a result of softness of CM material which can lead to more BUE formation and consequent coating deterioration.

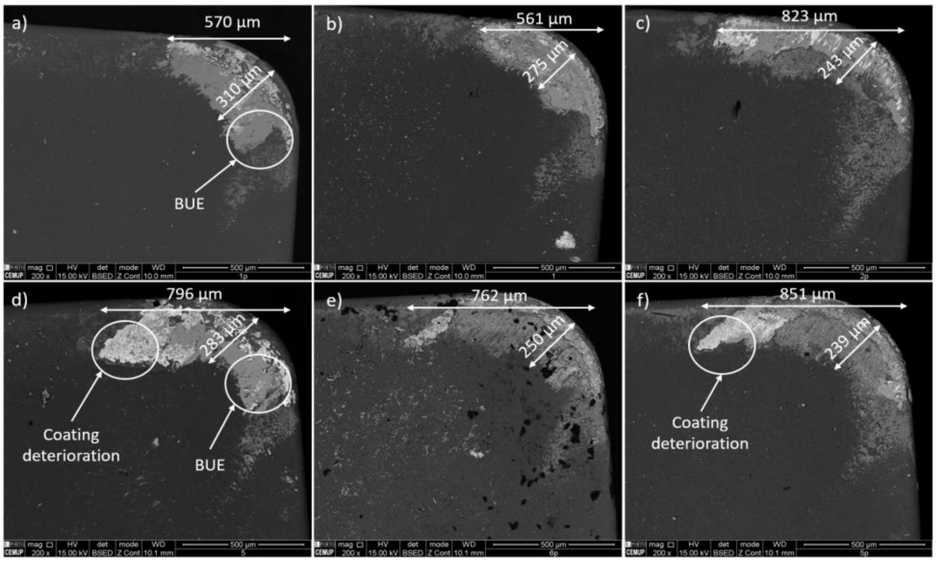

Figure 67 - SEM observations of the cutting insert tips used with different conditions - AM: a) v_c = 80 m/min, b) v_c = 200 m/min c) v_c = 320 m/min; CM: d) v_c = 80 m/min, e) v_c = 200 m/min f) v_c = 320 m/min.

4.2.5. Taguchi method analyses

The Taguchi method was used to reduce the number of samples to be analysed in the remaining analyses. After the experimental campaign with a full factorial, the Taguchi method was tested, choosing an orthogonal L_{18} matrix. After the analysis of variance, an excellent correlation is observed between the results obtained by the method and the results produced with the total data both in terms of roughness and specific cutting pressure, as shown in Figure 68. In Figure 68 c) and d), it is also possible to see that the method reproduces the difference found between the two materials and between the different cutting depths. In this way, it is concluded that the study of the remaining parameters using only the samples indicated by the Taguchi method will reproduce satisfactory results.

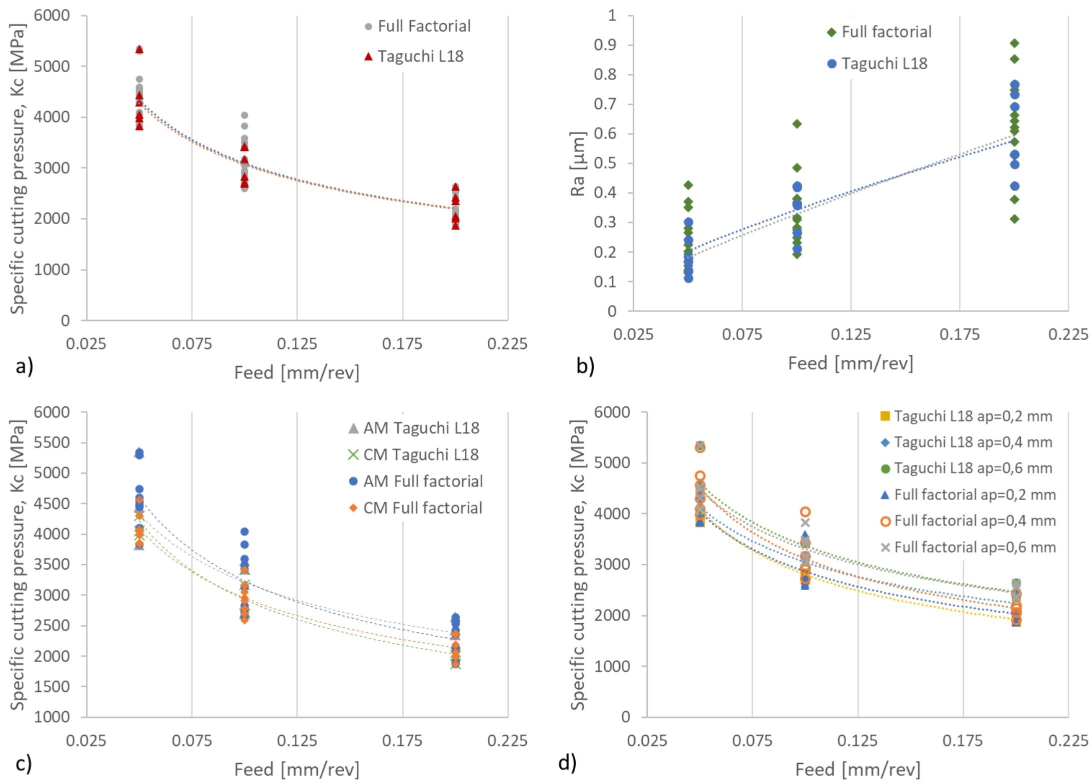

Figure 68 - Comparison of the results between the total data and the Taguchi method in function of feed: a) comparison of global Kc, b) comparison of Ra, c) difference in Kc between materials, d) differences in Kc between different depths of cut.

4.2.6. Hardness results on machined surfaces

Hardness measurements were carried out on the machined surfaces in order to study the degree of influence of milling parameters. The Taguchi method was used to reduce the number of milling tests to be analysed as referenced before in order to optimize the available laboratory time.

When analysing the influence of cutting parameters in Figure 69, once again, for the additive manufactured material, a clear major influence of the feed parameter over the other parameters on the hardness of the machined surface could be noted. Increasing the feed led to an increase in hardness of the machined surface in both materials. Increasing the depth of cut also resulted in an increase in hardness but this was not so significant. Similarly to the results observed in the specific cutting pressures, the cutting speed does not show a significant influence on the surface hardness. When compared with the originally hardness value, practically all the tests recorded an increase of hardness, which is result of the associated plastic deformation (strain hardening). The same observation was registered by Fortunato et al. [59] when milling an AM 18Ni300 maraging steel. Regarding the CM maraging steel, although there is also an increase compared to the original value, there are no variations in hardness for the different cutting parameters. It should be noted that the initial hardness measurements were carried out on polished samples of the materials in order not to be influenced by surface states.

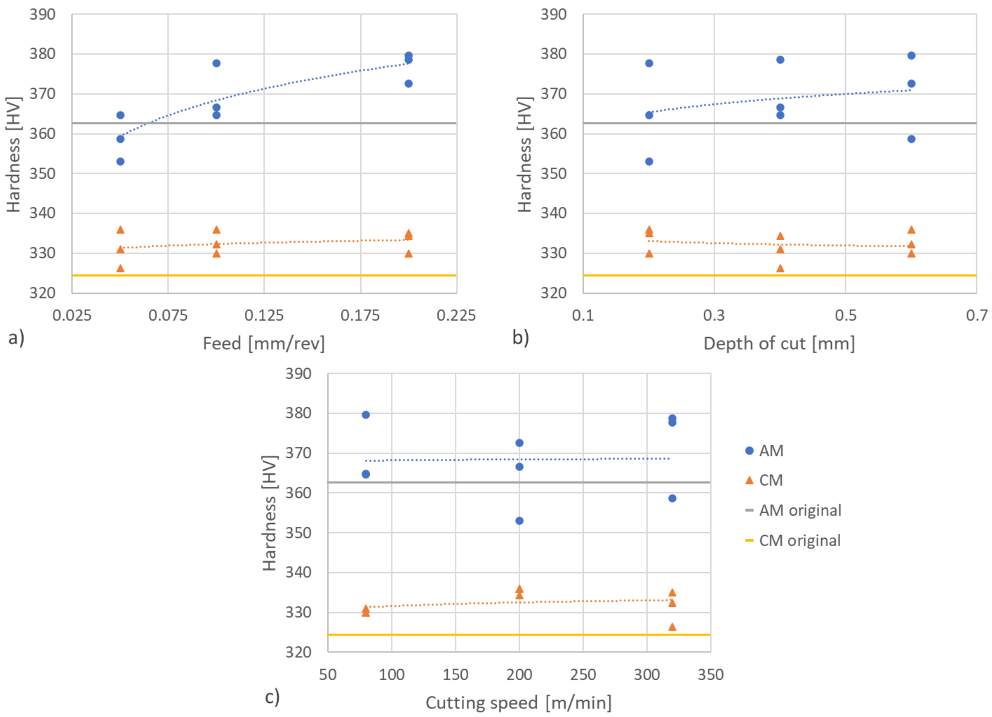

Figure 69 - Variation of surface hardness with: a) feed, b) depth of cut, c) cutting speed and comparison with hardness measurements in non milled surfaces.

Regarding the microhardness measurements in the sample profile (refer to Figure 36 c)), it is possible to observe in Figure 70 a) a decrease in microhardness along the sample depth. A clear tendency towards the initially measured hardness values is observed and explained by the plastic deformation suffered by the surface when machined. This layer is very small, not reaching more than 200 μm. In Figure 70 b), the marks of the microhardness measurements along a sample cross-section are visible.

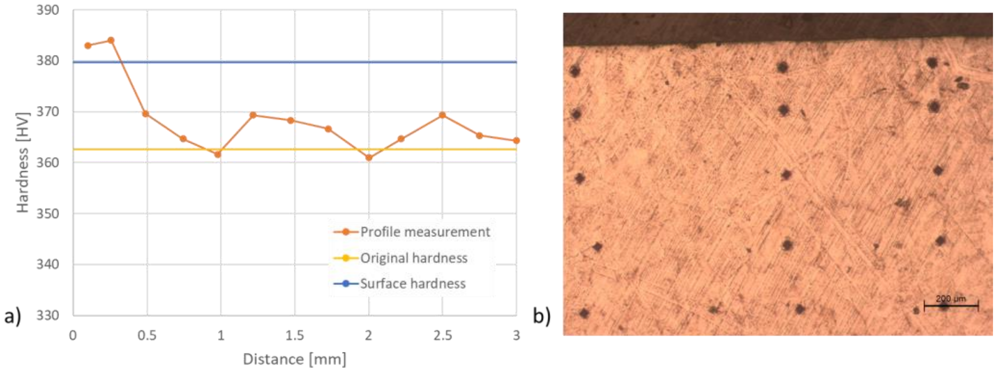

Figure 70 - Microhardness measurement: a) comparison with surface and original hardness, b) microhardness measurement marks, for v_c = 80 m/min, a_p = 0.6 mm, f = 0.2 mm/rev, AM.

After microhardness measurement, the samples were observed under the optical microscope. As shown in Figure 71, no microstructure changes could be observed near the cut zone for both the conventional material and the material produced by additive manufacturing. Although no crushing deformation of the surface layers is observed at this magnification (75x), a closer examination at higher magnifications may reveal an orientation of the grains in the direction of the mill rotation [11].

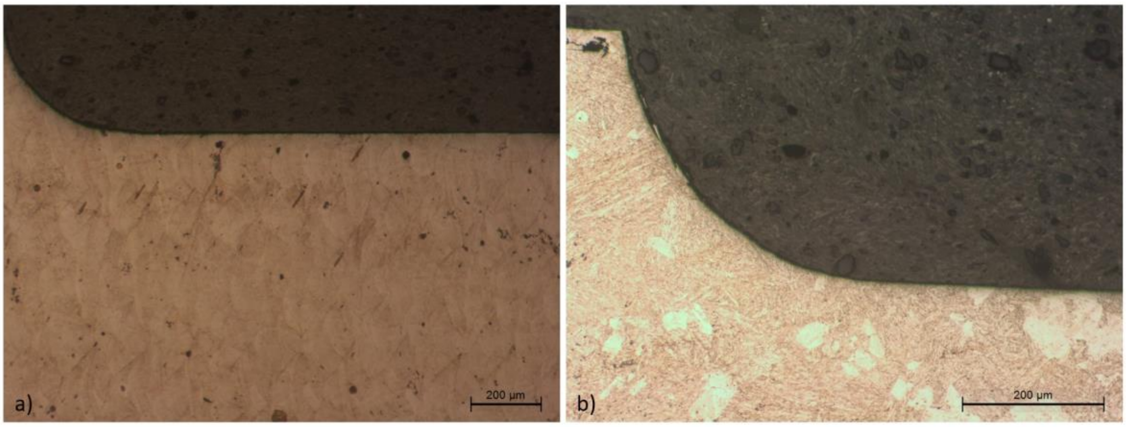

Figure 71 - Microstructures of the profile cut samples: a) AM, b) CM.

4.2.7. Residual stresses

Measurements before and after machining allowed the observation of an evolution of the residual stresses in the samples. Unlike the conventionally manufactured specimens that showed a consistent state of compression before machining, the additively manufactured specimens showed tensile stresses (refer to Figure 72). Moreover, the AM specimens exhibited a decrease in residual stresses along the specimen in the construction direction, as could be seen in Figure 72 a). During the cooldown of the molten layers in the production of this materials, thermal contraction causes shrinkage and leads to the creation of tensile stresses. The decrease in tensile stresses along the specimen is due to the fact that, as these specimens were vertically manufactured, the base of the specimen was subjected to greater thermal gradients because at the time of cooling, the specimen was still being built [90].

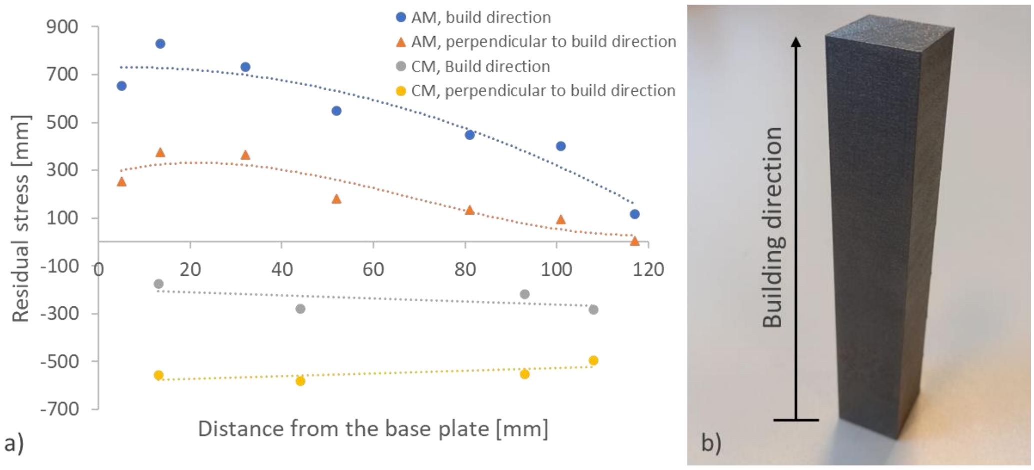

Figure 72 - a) Evolution of residual stress along the AM and CM specimens, b) AM specimen.

When the residual stress results were observed with varying cutting parameters, no significant trends were found. However, it could be observed that, regardless of the initial state and the material, the residual stresses evolved to a slightly compressed state in the machining direction (transverse to build direction) and to a nearly neutral state in the direction perpendicular to the machining direction (parallel to build direction). Thus, an opposite evolution was observed for each of the materials: in the conventional material there was a relaxation of compressive stresses while in the additive manufactured material there was a relaxation of tensile stresses. Compressive stresses after machining were also observed in the studies of Oliveira et al. [70, 73], when milling AM maraging steel. The generality of the final states also presents an opposite and apparently symmetrical trend between the two materials, as is most easily seen in Figure 73 a). Compressive behaviour is typical after milling because of a stress redistribution induced by machining and is beneficial to mechanical properties, mainly to reduce the probability of crack open, thus improving fatigue behaviour [70].

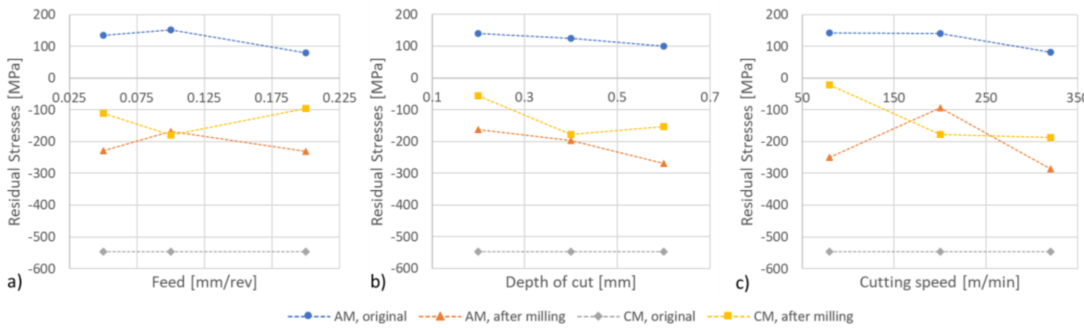

Figure 73 - Variation of residual stress in the machining direction (perpendicular to build direction) for different: a) feeds, b) depths of cut), c) cutting speeds, for the two materials.

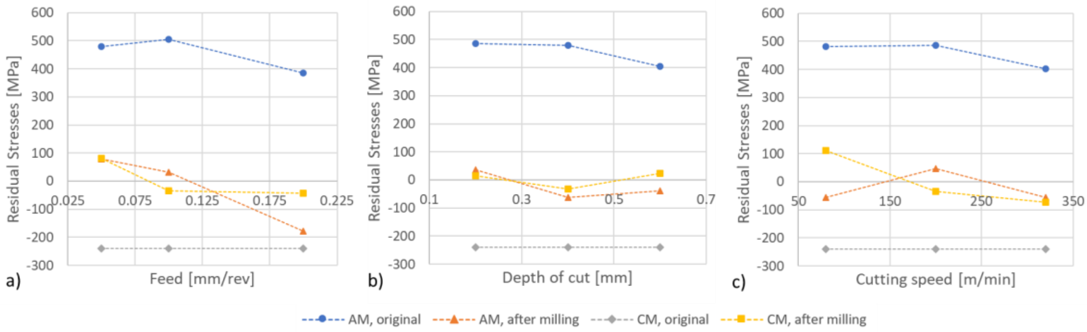

Figure 74 - Variation of residual stress in the direction perpendicular to the machining direction (parallel to build direction) for different: a) feeds, b) depths of cut), c) cutting speeds, for the two materials.

4.2.8. Chip morphology

In Figure 75, the chip morphology evolution with the variation of the different cutting parameters is presented for the AM 18Ni300 steel. It is possible to observe a higher influence of the feed per revolution in the chip morphology, which is in accordance with the analysis of the loads results. On one hand, the chip tends to assume a more defined helical/sting shape with the increase in feed per revolution and on the other hand, for smaller feeds, the pitch tends to be higher, and diameter of the helical shape tends to be smaller, resulting in a more elongated chip. As expected, the increase in uncut chip cross sectional area is visible for all cutting speeds with more robust chips being generated.

When cutting the specimens with higher depths of cut, it seems that a more conical/helical shape is obtained, which could be result of higher elastic deformation capacity with thicker chips. Regarding cutting speed, there were no significant differences in the morphology of the chip.

In Figure 76, a comparison between the resulting chips of the two manufacturing processes used in this work, for a cutting speed of 320 m/min, is shown. As observed, no notorious differences were found, which is also true for the other cutting speeds used. These results corroborate the low porosity and high ductility of the tested AM 18Ni300 steel, being very similar to the conventional manufactured 18Ni300 steel.

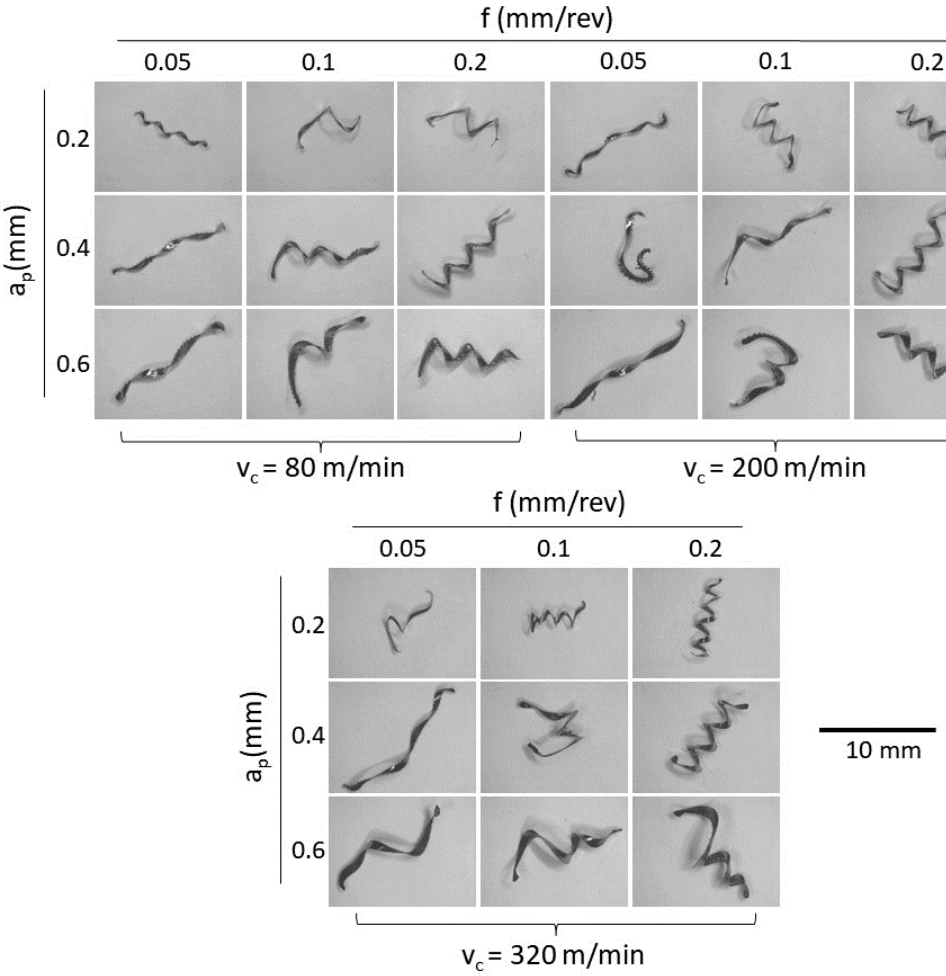

Figure 75 - Chip evolution with the variation of the feed per revolution, f, and depth of cut, a_p, and the cutting speed, v_c, for the additive manufactured 18Ni300 steel.

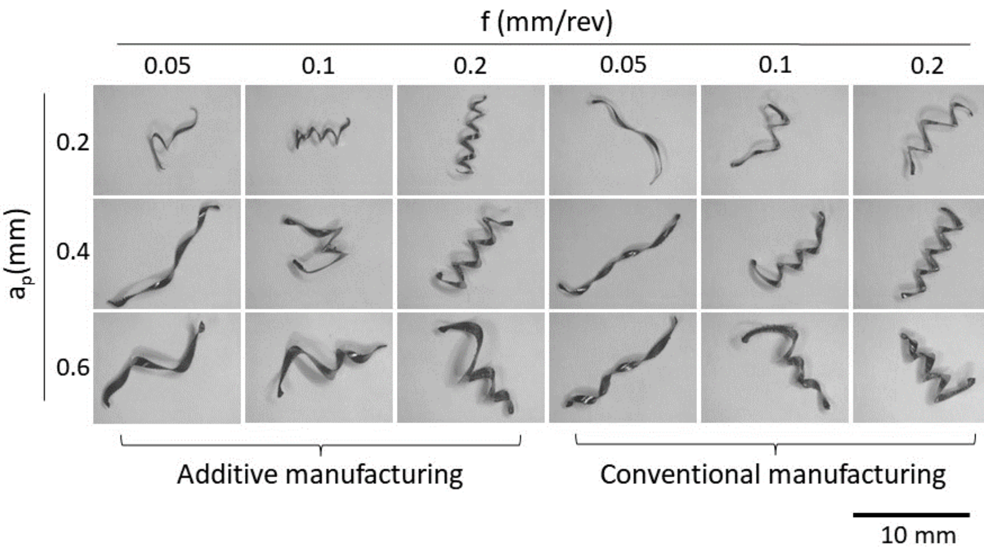

Figure 76 - Chip evolution comparison between additive and conventional manufactured 18Ni300 steel with the variation of the feed per revolution, f, and depth of cut, a_p , for a cutting speed of 320 m/min.

The visualization of chips in SEM allowed to observe an accentuation of the serration of the chip with increasing feed, as could be seen in Figure 77. This continuous breaking effect also leads to greater chip coiling. For different depths of cut, except for the increase in chip width, there were no significant differences, as shown in Figure 78. Regarding the cutting speed, increasing it led to a greater presence of deformation bands, as could be seen in Figure 79, which results from the higher deformation rates of the material when the speed increases.

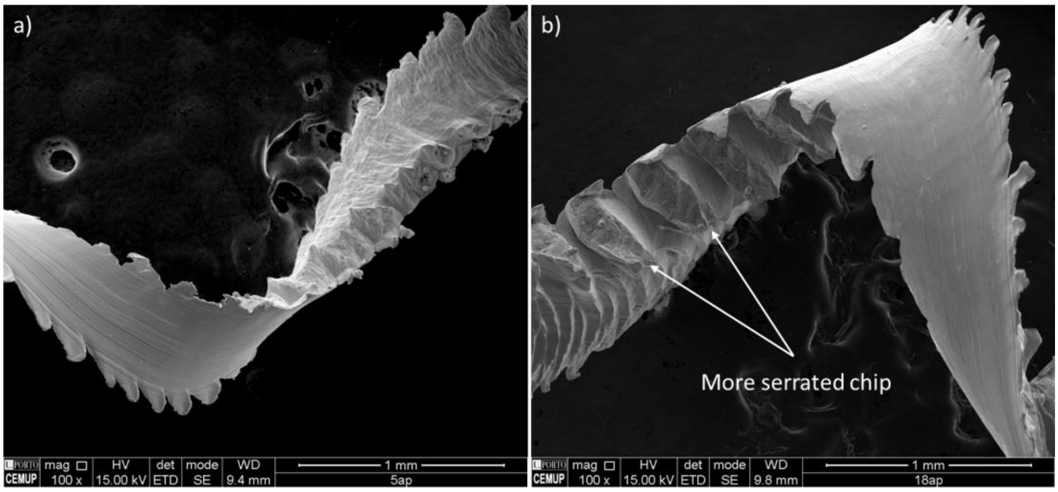

Figure 77 - Influence of feed in the morphology of the chips: a) f = 0.4 mm/rev, b) f = 0.6 mm/rev.

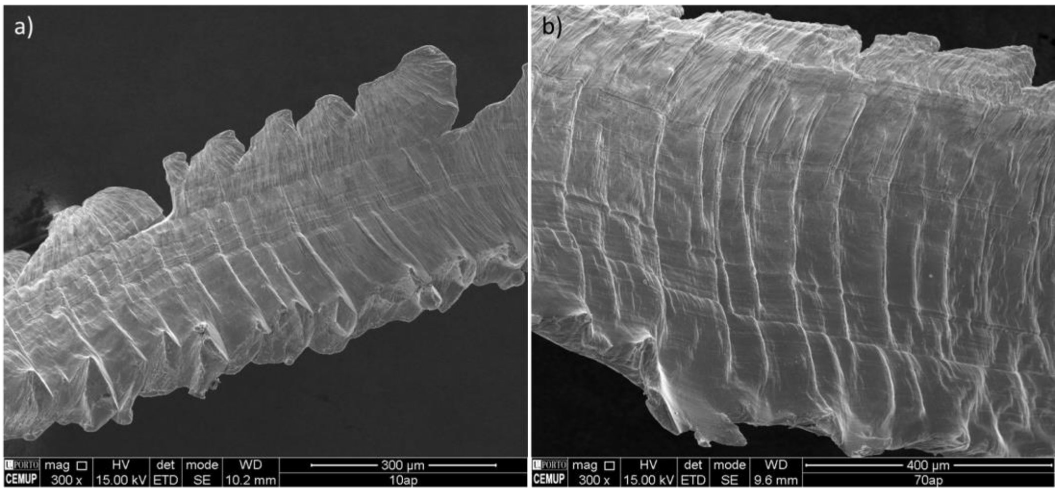

Figure 78 - Influence of depth of cut in the morphology of the chips: a) a_p = 0.2 mm, b) a_p = 0.6 mm, for a v_c=200 m/min and f=0.05 mm/rev.

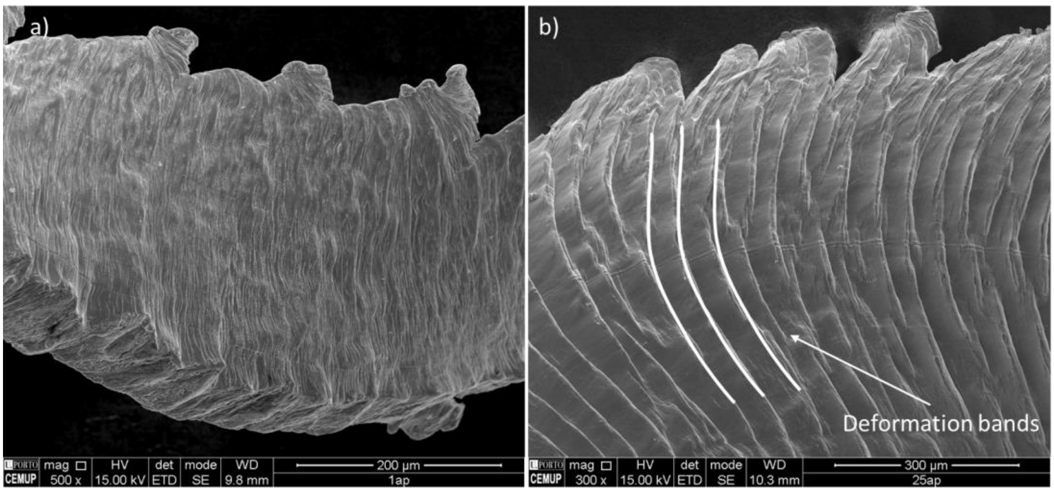

Figure 79 - Influence of cutting speed in the morphology of the chips: a) v_c = 80 m/min, b) v_c = 320 m/min, for f=0.05 mm/rev and AM material.

In Figure 80, differences between the different chip surfaces can be observed: chip surfaces of additive (c) and conventional (a) manufacturing, and the chip back-side (chip surface generated by the tool (b)). The differences between the serrated chip surface of the two materials result from the initial surface states: ground for conventional and as-built for additive.

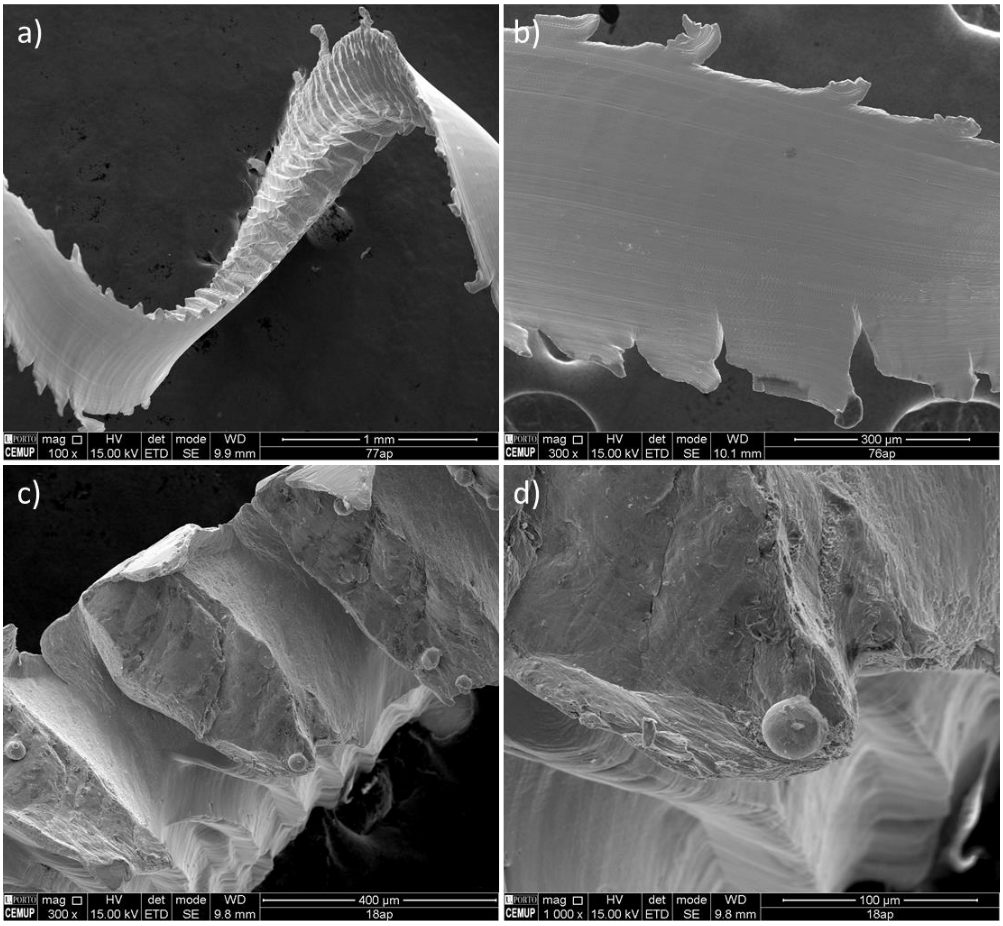

Figure 80 - a) CM chip, b) surface generated by the cutting tool, c) AM chip, d) detail of powder particle.

4.3. Numerical simulation results

4.3.1. Cutting length calibration

The numerical model of milling simulation consists of half rotation of the milling tool, corresponding to one chip removal (one teeth cutting length). The full tooth engagement (180º) simulation was performed, and a good overall trend of the obtained forces compared to the experimental data was attained, as shown in Figure 81 a). However, the simulation of the 180º of cut represents an extremely high computational cost, and for this reason the workpiece cutting length was reduced. The cutting length was simulated within a selected range of engagement in order to portray the region at which the maximum cutting forces are reached. For this purpose, simulations of different workpiece engagement range were performed.

The choice fell on the simulation of the central 20º of tool engagement (80º to 100º) (refer to Figure 82 b)) that incorporated the place of maximum force in the process and at the same time allowed a stabilization of the results, as shown in Figure 82 a). This cutting length reduction allowed to obtain a simulation time 22 times less than the full cut. For feeds smaller than 0.1 and 0.05 a cutting length of 17° and 12°, respectively, was used.

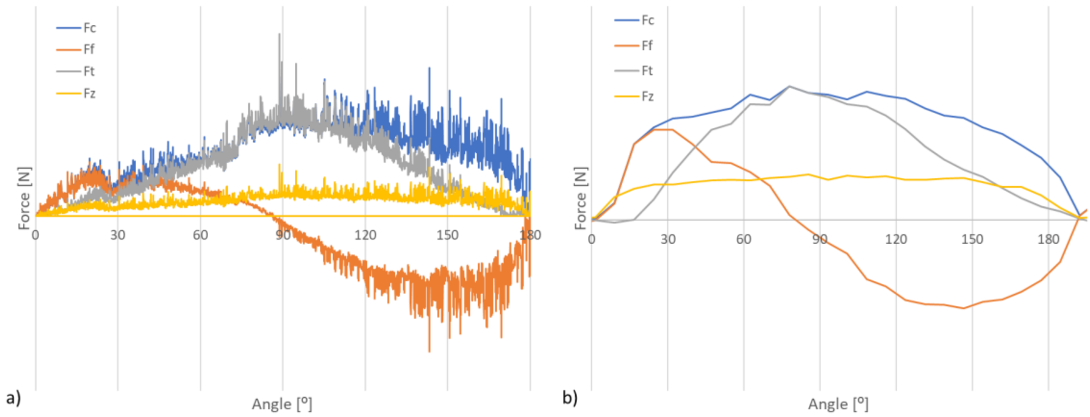

Figure 81 - Geometry of forces obtained by: a) simulation, b) experimental tests.

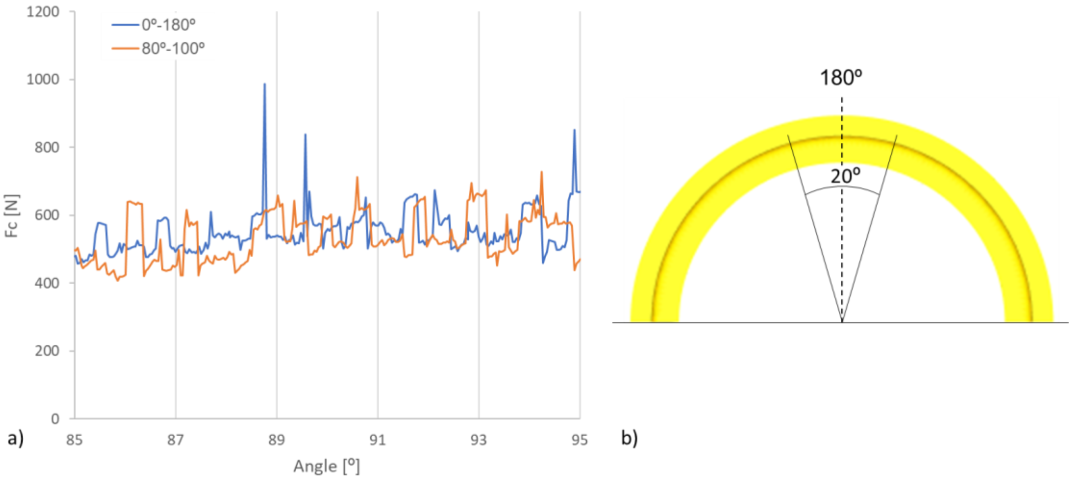

Figure 82 - a) Comparison of results of different engagement ranges of cut between 85° and 95°, b) cutting length of 80°-100°.

4.3.2. FEM mesh sensitivity analysis

The mesh calibration had three fundamental steps: finding the best compromise between element size and computational cost for the main mesh, secondary mesh, and tool mesh. In relation to the main mesh of the piece (the mesh that is subjected to remeshing) it was defined as a function of the feed rate parameter, which is the most influential parameter, as seen in Section 4.2.

In Figure 83 a), it is possible to observe the progress of the simulations with the reduction of the minimum mesh element. Besides a higher stability of the results, with a decrease of the associated leads scatter, the mesh refinement allowed a higher precision and compatibility of the results with the experimental data (no significant changes in the numerical load were observed for smaller element size). The mesh reaches a plateau of stability by values of about 12% of the feed. However, this mesh refinement is accompanied by an non-exponential increase in simulation time, as shown in Figure 83 b).

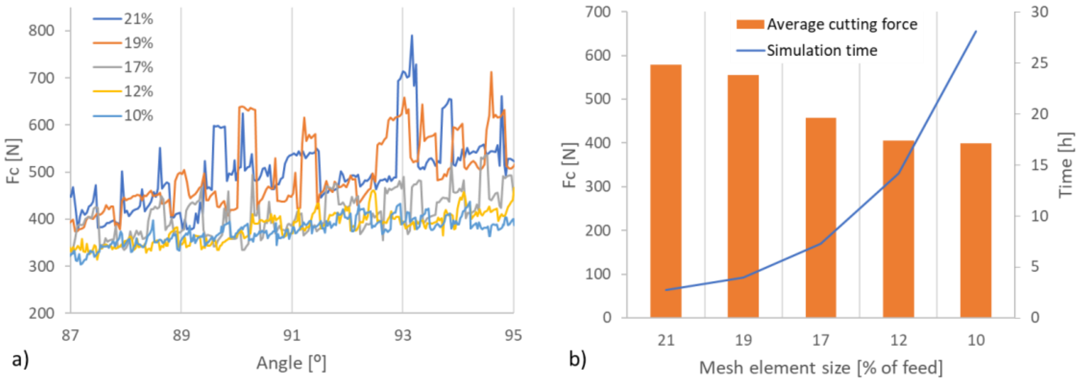

Figure 83 - Simulated cutting force comparison between different principal meshes: a) simulations b) comparison with simulation time.

The secondary mesh was defined as a function of the main mesh by a minimum element size ratio. The comparison of different ratios (refer to Figure 84 a)) showed a stability of results for ratios lower than 4, so this was the value chosen for the simulations. The tool mesh was defined as a function of the total number of elements. When comparing the results for different meshes (refer to Figure 84 b)), it is observed that the influence of this mesh is not as significant as the others because the tool behaves almost like a rigid body.

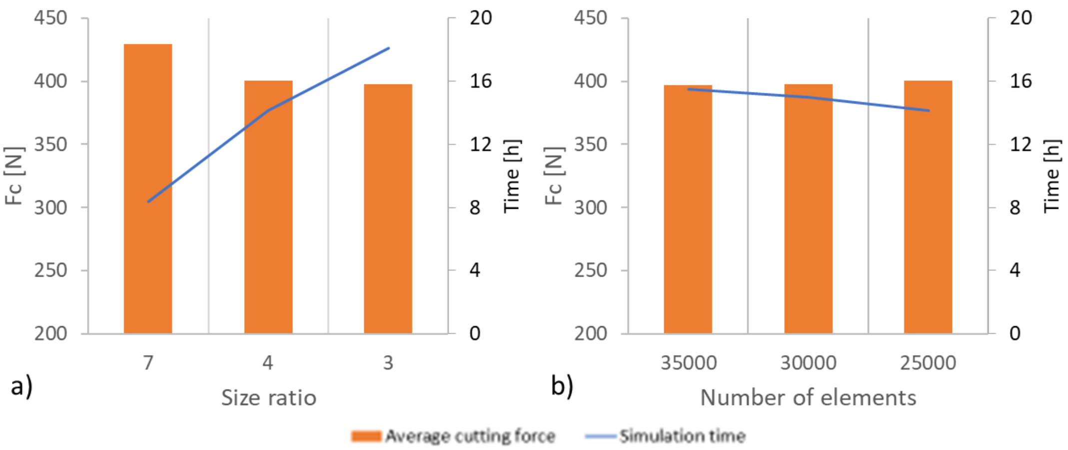

Figure 84 - a) Comparison of different mesh size ratios for the secondary part mesh and b) comparison of different number of elements in tool mesh in simulation.

In general, it was decided to keep the chosen values of mesh parameters for all simulations. The reduction in cutting length was not enough to equalize the simulation times. The reduction of the feed rate and consequent reduction of the mesh led to an increase of the computational cost necessary for these simulations, as shown in Figure 85 a).

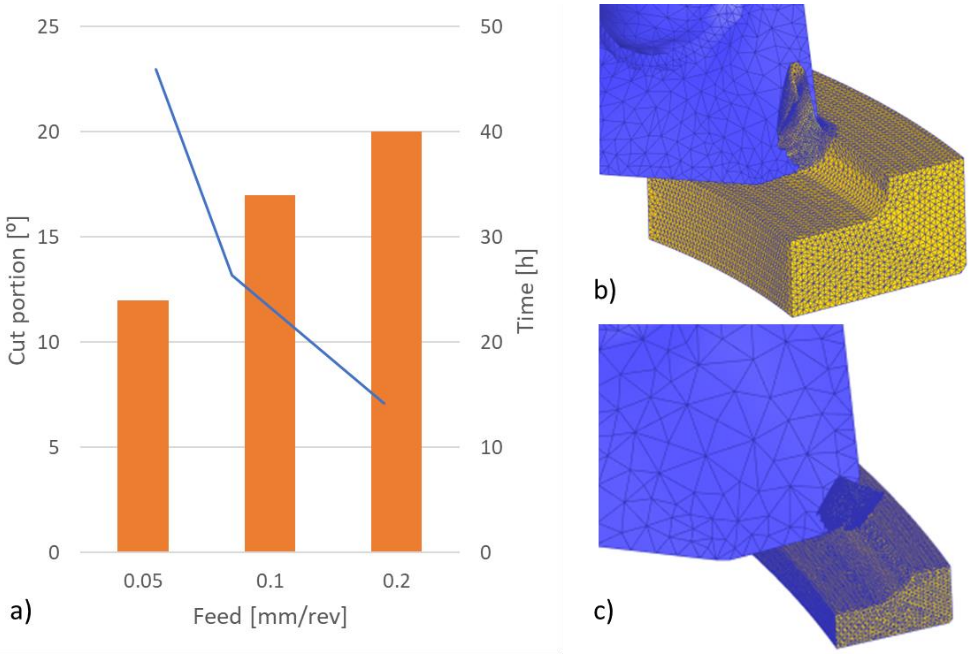

Figure 85 - a) Cutting length and computational cost of simulations for different feeds, b) mesh for f = 0.2 mm/rev, c) mesh for f = 0.05 mm/rev.

4.3.3. Material model definition

Due to the differences between the Abaqus CAE and DEFORM software, a definition of the model had to be done, with parameter C of the model (refer to Table 6) set to 0.02. The model used by Silva [18] for turning modelling was used to model the milling process. In Figure 86, a comparison between the flow curves of the material obtained experimentally and using the numerical model is shown.

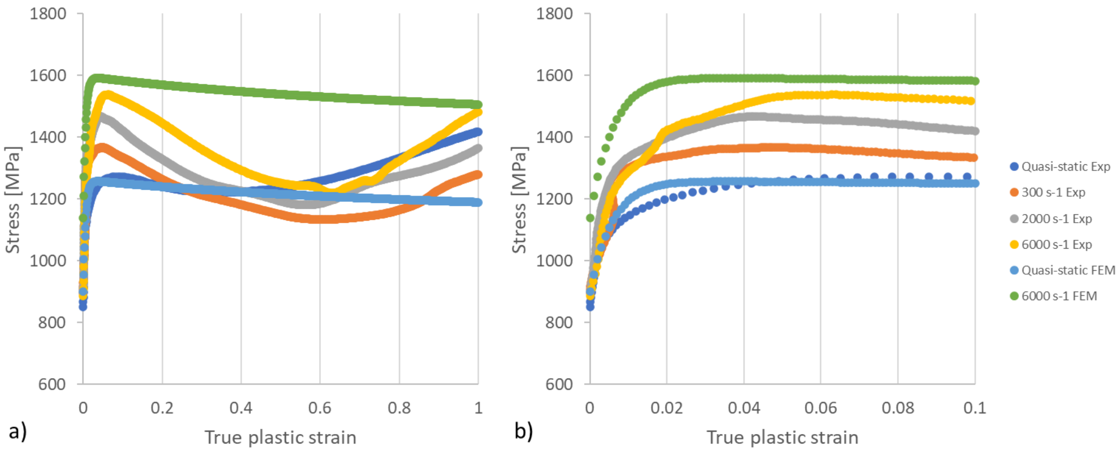

Figure 86 - Flow curves of AM maraging steel experimentally and numerically obtained by Silva [18], for different ranges of true plastic strain.

4.3.4. Friction calibration

Although Silva [18] has used the Coulomb model in his studies, in this dissertation only the shear model was studied. The obtained results (refer to Figure 87) do not show a great variability between them, so a conservative value in numerical terms of 0.6 (shear model) was chosen.

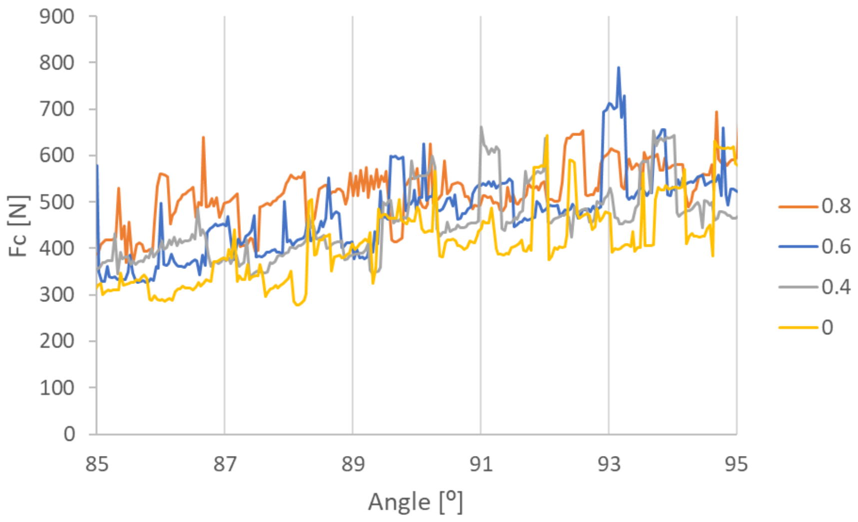

Figure 87 - Comparison of different friction coefficients in simulation results (vc = 320 m/min, ap = 0.6 mm, f = 0.2 mm/rev).

4.3.5. Cutting forces and specific cutting pressures analysis

Due to the high computational cost of each simulation, only the test conditions described in Figure 88 b) were performed. Regarding the cutting forces, they present a reasonable compatibility when compared with the experimental data. The lower capacity of load prediction for lower feed rates is due to the fact that the simulation does not consider size effects. This effect becomes more visible when the specific cutting pressure is calculated. This suboptimal prediction of cutting forces may also be due to the fact that the simulation is not very accurate in the way each force component is calculated, resulting in the cutting force being the sum of these forces and associated errors. The Kc values, since they do not consider size effects, present a stable plateau, as shown in Figure 88 a), capable of predicting by overestimation, the Kc value when higher feeds are used.

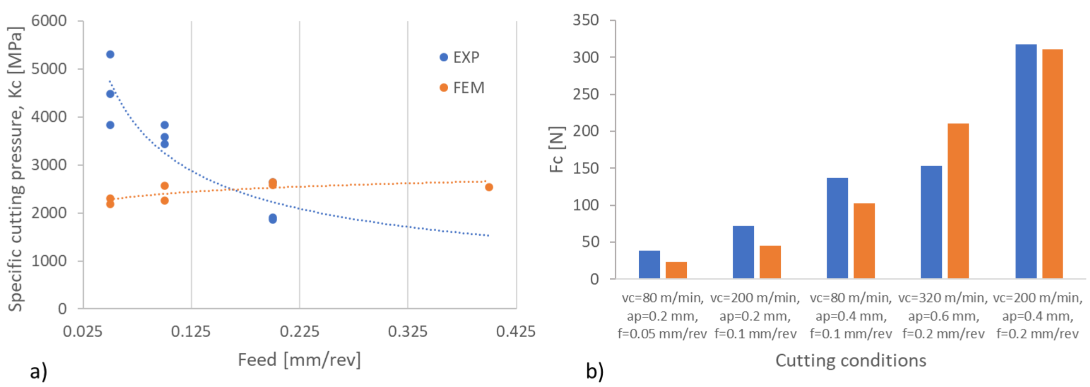

Figure 88 - Comparison of FEM and experimental results in terms of: a) specific cutting pressure, b) cutting force.

4.3.6. Chip modelling

The full cut simulation was only performed for the maximum parameters set of the parameters analysed due to the high computational cost. With the full cut simulation, it was possible to model the chip. The morphology obtained is qualitatively very close to that observed in the experimental tests, as shown in Figure 89.

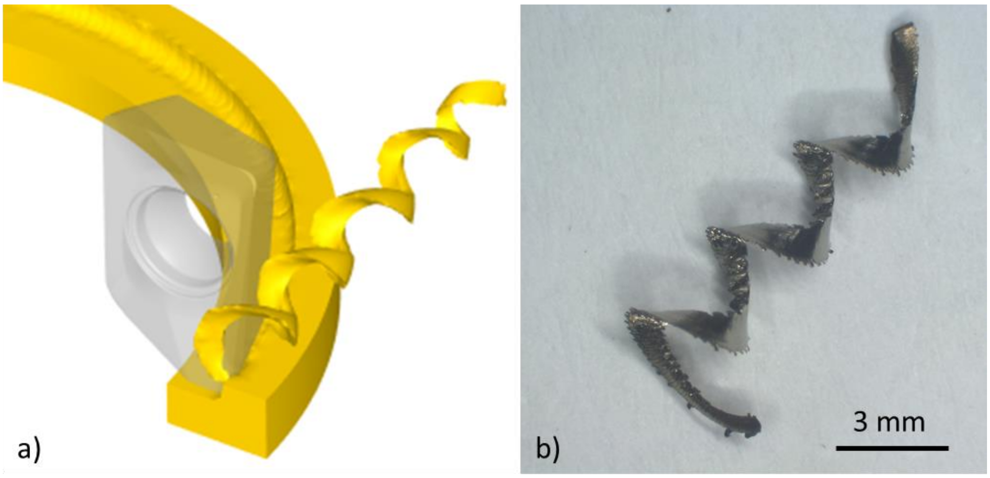

Figure 89 - Chip morphology: a) FEM, b) experimental tests, for f = 0.2 mm/rev and a_p *= 0.6 mm.*

5. Conclusions and future work

5.1. Conclusions

In this section, the conclusions drawn from the experimental procedures, in terms of material characterisation, cutting forces, chip morphology, surface finish, among others are presented, as well as conclusions derived from the milling simulations.

Experimental tests:

- The cutting forces are mainly influenced by the thickness of the uncut chip, i.e. with increasing feed and depth of cut they increase due to the larger volume of material to be cut with each pass of the cutting insert.
- The feed is the parameter with the greatest influence on the specific cutting pressure, with an exponential growth of this pressure for small feeds. This growth is due to size effects, which although not significant for large feeds, for small ones they present similar magnitude causing the specific cutting pressure to increase in a non-linear way.
- With regards to the AM as-built surface, there was on average a 1000% improvement in surface roughness. These values were achieved with just one milling operation, which shows the advantage of process hybridization (combining additive with subtractive manufacturing).
- The roughness was mainly affected by changing the feed parameter, having a linear increase with the increase in feed. As the feed increases, the uncut chip area not cut by the tool increases, resulting in the typical more prominent pattern of the milling process.
- More pronounced wear tendencies were observed on tools used at higher cutting speeds, which results from the higher impact suffered by the tool. On the other hand, there was a reduction of BUE, which is in agreement with the revised literature.
- The Taguchi method proved to be an extremely valuable tool, as it allowed for a significant reduction in the number of samples to be analysed for some parameters.
- There is an increase in hardness with feed in the AM material, a result of the greater plastic deformation suffered. In the CM material this increase was not so significant, which may be a result of the higher strain-hardening of the material.
- The measurement of residual stresses showed that regardless of the initial state of the surface, after machining the surfaces had similar stress values. Also, surface tensile residual stresses from AM process will go to compressive due to machining which is a very beneficial effect if one intends to increase the component fatigue resistance.
- In terms of chip morphology, the increase in feed led to more material curling and more serrated chips.

- A good compatibility of specific cutting pressure was achieved between different literature studies and this research study, even though different machining operations were considered. This is a good indicator of the developed methodologies and procedures.

Numerical simulation

- The model developed by Silva [18] proved to be suitable for milling simulations in DEFORM software.
- In order to reach stability levels, the remeshing technique, with refined meshes, presents an extremely high computational time.
- The developed numerical model allowed to successfully simulate with good numerical-experimental correlation both cutting force and chip morphology.
- Since the model and the software used do not take into account the occurrence of size effects for smaller feed rates, the forces obtained for those conditions may be underestimated.
- The model allowed to define a plateau of stability by over estimation of the specific cutting pressure for higher values of feed.

5.2. Future works

- The quantification of the percentage of austenite and martensite phases (through X-ray diffraction, for example) according to the metallurgical state of 18Ni300 maraging steel will allow a better understanding of its microstructural state.
- Machinability studies with drilling tests on AM maraging steel can complete this study that has been carried out over the years.
- Instrumented vibration testing can give another point of view on the milling process, complementing the analysis.
- In addition to vibration measurement, temperature measurement during cutting can bring new data to the discussion.
- As far as residual stress analysis is concerned, in-depth analysis will give a more accurate idea of the influence of machining on the surface integrity.
- The development of a more sophisticated model that incorporates size effects in machining can bring interesting discussions.

Bibliography

1. Verma, R. and Kaushal, G., *State of the Art of Powder Bed Fusion Additive Manufacturing: A Review*, in *3D Printing and Additive Manufacturing Technologies*, L.J. Kumar, P.M. Pandey, and D.I. Wimpenny, Editors. 2019, Springer Singapore: Singapore. p. 269-279.
2. Bugatti Automobiles S.A.S. *World Premiere: Brake Caliper From 3-D Printer*. 2018 [Access date: 02/06/2022]; Available from: https://www.bugatti.com/media/news/2018/world-premiere-brake-caliper-from-3-d-printer/.
3. Minguella-Canela, J., Morales Planas, S., and De los Santos-López, M.A., *SLM Manufacturing Redesign of Cooling Inserts for High Production Steel Moulds and Benchmarking with Other Industrial Additive Manufacturing Strategies.* Materials, 2020. **13**(21): p. 4843.
4. Milacron S.A. *Milacron's dme product brand announces partnership with 3d additive leader linear ams to provide revolutionary conformal cooling solutions under its new trucool product line.* 2017 [Access date: 03/06/2022]; Available from: https://www.milacron.com/pt-pt/news_and_events/milacrons-dme-product-brand-announces-partnership-with-3d-additive-leader-linear-ams-to-provide-revolutionary-conformal-cooling-solutions-under-its-new-trucool-product-line/.
5. Groover, M.P., *Fundamentals of modern manufacturing : materials, processes, and systems*. 3 ed. 2007: John Wiley & Sons, 2010.
6. Jesus, A.M.P.d., *Fundamentos do Corte: Teoria e Exercícios*. 2019.
7. Geoffrey Boothroyd, W.A.K., *Mechanics of Metal Cutting*, in *Fundamentals of Machining and Machine Tools*, I. Marcel Dekker, Editor. 1989: United States of America. p. 531.
8. Markopoulos, A., *Finite Element Method in Machining Processes*. 1 ed. SpringerBriefs in Applied Sciences and Technology. 2012: Springer London.
9. Toenshoff, H.K. and Denkena, B., *Basics of Cutting and Abrasive Processes*. 2013: Springer Berlin Heidelberg.
10. Mendanha, B., et al., *Cutting performance and wear behavior of coated cermet and coated carbide tools when turning AISI 4340 steel.* The International Journal of Advanced Manufacturing Technology, 2019. **105**: p. 1655–1663.
11. Böllinghaus, T., et al., *Manufacturing Engineering*, in *Springer Handbook of Mechanical Engineering*, K.-H. Grote and E.K. Antonsson, Editors. 2009, Springer Berlin Heidelberg: Berlin, Heidelberg. p. 523-785.
12. San-Juan, M., et al., *Study of Cutting Forces and Temperatures in Milling of AISI 316L.* Procedia Engineering, 2015. **132**: p. 500-506.
13. Soo, S.L. and Aspinwall, D.K., *Developments in modelling of metal cutting processes.* Proceedings of the Institution of Mechanical Engineers, Part L: Journal of Materials: Design and Applications, 2007. **221**(4): p. 197-211.
14. Merchant, H.E.M. and Ernst, H., *Chip formation, friction and high quality machined surfaces.* Surface Treatment of Metals, 1941. **29**: p. 299–378.
15. David A. Stephenson, J.S.A., *Metal Cutting Theory And Practice*. 3 ed. 2016, Boca Raton.
16. Lee, E.H. and Shaffer, B.W., *The theory of plasticity applied to a problem of machining.* Trans ASME - J Appl Mech, 1951. **18**: p. 405–413
17. Oxley, P.L.B., *The mechanics of machining: an analytical approach to assessing machinability*, E. Horwood, Editor. 1989: Chichester.
18. Silva, T.E.F., *Machinability of Maraging Steel Manufactured by Laser Powder Bed Fusion*. 2021, PhD Thesis, University of Porto: Porto.
19. Zorev, N.N., *Interrelationship between shear processes occurring along tool face and on shear plane in metal cutting*, in *Proceedings of the international research in production engineering conference*. 1963, ASME. p. 42-49.

20. Usui, E., Hirota, A., and Masuko, M., *Analytical prediction of three dimensional cutting process. Part 1. Basic cutting model and energy approach.* Trans ASME—J Eng, 1978. **100**: p. 222–228.
21. Childs, T.H.C. and Maekawa, K., *Computer-aided simulation and experimental studies of chip flow and tool wear in the turning of low alloy steels by cemented carbide tools.* Wear, 1990. **139**: p. 235–250.
22. Özel, T., *The influence of friction models on finite element simulations of machining.* International Journal of Machine Tools and Manufacture, 2006. **46**(5): p. 518-530.
23. Filice, L., et al., *A critical analysis on the friction modelling in orthogonal machining.* International Journal of Machine Tools and Manufacture, 2007. **47**(3): p. 709-714.
24. Arrazola, P.J. and Özel, T.r., *Investigations on the effects of friction modeling in finite element simulation of machining.* International Journal of Mechanical Sciences, 2010. **52**(1): p. 31-42.
25. Arrazola, P., et al., *Recent advances in modelling of metal machining processes.* CIRP Annals - Manufacturing Technology, 2013. **62**: p. 695–718.
26. Özel, T. and Zeren, E., *Finite element modeling the influence of edge roundness on the stress and temperature fields induced by high-speed machining.* The International Journal of Advanced Manufacturing Technology, 2007. **35**(3): p. 255-267.
27. Gurusamy, M.M. and Rao, B.C., *On the performance of modified Zerilli-Armstrong constitutive model in simulating the metal-cutting process.* Journal of Manufacturing Processes, 2017. **28**: p. 253-265.
28. Quiza, R., López-Armas, O., and Davim, J.P., *Finite element in manufacturing processes*, in *SpringerBriefs in Applied Sciences and Technology*. 2012, Springer London. p. 13-37.
29. Dixit, U.S., Joshi, S.N., and Davim, J.P., *Incorporation of material behavior in modeling of metal forming and machining processes: A review.* Materials & Design, 2011. **32**(7): p. 3655-3670.
30. Johnson, G.R. and Cook, W.H., *Fracture characteristics of three metals subjected to various strains, strain rates, temperatures and pressures.* Engineering Fracture Mechanics, 1985. **21**: p. 31–48.
31. Umbrello, D., M'Saoubi, R., and Outeiro, J.C., *The influence of Johnson-Cook material constants on finite element simulation of machining of AISI 316L steel.* International Journal of Machine Tools and Manufacture, 2007. **47**(3-4): p. 462-470.
32. Tounsi, N., et al., *From the basic mechanics of orthogonal metal cutting toward the identification of the constitutive equation.* International Journal of Machine Tools and Manufacture, 2002. **42**: p. 1373-1383.
33. Chandrasekaran, H., Msaoubi, R., and Chazal, H., *Modelling of material flow stress in chip formation process from orthogonal milling and split Hopkinson bar tests.* Machining Science and Technology, 2005. **9**: p. 131-145.
34. Calamaz, M., Coupard, D., and Girot, F., *A new material model for 2D numerical simulation of serrated chip formation when machining titanium alloy Ti–6Al–4V.* International Journal of Machine Tools and Manufacture, 2008. **48**(3): p. 275-288.
35. Sima, M. and Özel, T., *Modified material constitutive models for serrated chip formation simulations and experimental validation in machining of titanium alloy Ti–6Al–4V.* International Journal of Machine Tools and Manufacture, 2010. **50**(11): p. 943-960.
36. Zerilli, F.J. and RW, R.W.A., *Dislocation-mechanics-based constitutive relations for material dynamics calculations.* J Appl Phys, 1987. **61**: p. 1816–1825.
37. Samantaray, D., Mandal, S., and Bhaduri, A.K., *A comparative study on Johnson Cook, modified Zerilli–Armstrong and Arrhenius-type constitutive models to predict elevated temperature flow behaviour in modified 9Cr–1Mo steel.* Computational Materials Science, 2009. **47**(2): p. 568-576.
38. Stevenson, M.G., Wright, P.K., and Chow, J.G., *Further Developments in Applying the Finite Element Method to the Calculation of Temperature Distributions in Machining and Comparisons With Experiment.* Journal of Engineering for Industry, 1983. **105**(3): p. 149-154.
39. Davies, M.A., et al., *On the measurement and prediction of temperature fields In machining AISI 1045 steel.* CIRP Annals, 2003. **52**(1): p. 77-80.

40. Grzesik, W., Bartoszuk, M., and Nieslony, P., *Finite difference analysis of the thermal behaviour of coated tools in orthogonal cutting of steels.* International Journal of Machine Tools and Manufacture, 2004. **44**(14): p. 1451-1462.
41. Usui, E., Shirakashi, T., and Kitagawa, T., *Analytical Prediction of Three Dimensional Cutting Process—Part 3: Cutting Temperature and Crater Wear of Carbide Tool.* Journal of Engineering for Industry, 1978. **100**(2): p. 236-243.
42. Zetterberg, M., *A critical overview of machining simulations in ABAQUS*. 2014, MSc Thesis, KTH Royal Institute Of Technology: Stockholm, Sweden.
43. Markopoulos, A., Karkalos, N., and Papazoglou, E.-L., *Meshless Methods for the Simulation of Machining and Micro-machining: A Review.* Archives of Computational Methods in Engineering, 2019. **27**: p. 831-853.
44. Uhlmann, E., Gerstenberger, R., and Kuhnert, J., *Cutting Simulation with the Meshfree Finite Pointset Method.* Procedia CIRP, 2013. **8**: p. 391-396.
45. Redwood, B., Schffer, F., and Garret, B., *The 3D Printing Handbook: Technologies, design and applications*. 2017.
46. Sing, S.L., et al., *3D printing of metals in rapid prototyping of biomaterials: Techniques in additive manufacturing*, in *Rapid Prototyping of Biomaterials*, R. Narayan, Editor. 2020. p. 17-40.
47. Thompson, S.M., et al., *An overview of Direct Laser Deposition for additive manufacturing; Part I: Transport phenomena, modeling and diagnostics.* Additive Manufacturing, 2015. **8**: p. 36-62.
48. Arias-González, F., et al., *Chapter 4 - Laser-directed energy deposition: principles and applications*, in *Additive Manufacturing*, J. Pou, A. Riveiro, and J.P. Davim, Editors. 2021, Elsevier. p. 121-157.
49. Ladani, L. and Sadeghilaridjani, M., *Review of Powder Bed Fusion Additive Manufacturing for Metals.* Metals, 2021. **11**(9): p. 1391.
50. Zimmermann, M., et al., *Analysis of the machinability when milling AlSi10Mg additively manufactured via laser-based powder bed fusion.* The International Journal of Advanced Manufacturing Technology, 2021. **112**: p. 1-17.
51. Yap, C.Y., et al., *Review of selective laser melting: Materials and applications.* Applied Physics Reviews, 2015. **2**: p. 041101.
52. Ali, H., Ghadbeigi, H., and Mumtaz, K., *Effect of scanning strategies on residual stress and mechanical properties of Selective Laser Melted Ti6Al4V.* Materials Science and Engineering: A, 2018. **712**: p. 175-187.
53. Sames, W., et al., *The metallurgy and processing science of metal additive manufacturing.* International Materials Reviews, 2016. **61**: p. 1-46.
54. Dev Singh, D., Mahender, T., and Raji Reddy, A., *Powder bed fusion process: A brief review.* Materials Today: Proceedings, 2021. **46**: p. 350-355.
55. Singh, R., et al., *Powder bed fusion process in additive manufacturing: An overview.* Materials Today: Proceedings, 2020. **26**: p. 3058-3070.
56. Casalino, G., et al., *Experimental investigation and statistical optimisation of the selective laser melting process of a maraging steel.* Optics and Laser Technology, 2015. **65**: p. 151-158.
57. Bai, Y., et al., *Influence mechanism of parameters process and mechanical properties evolution mechanism of maraging steel 300 by selective laser melting.* Materials Science and Engineering A, 2017. **703**: p. 116-123.
58. Mutua, J., et al., *Optimization of selective laser melting parameters and influence of post heat treatment on microstructure and mechanical properties of maraging steel.* Materials and Design, 2018. **139**: p. 486-497.
59. Fortunato, A., et al., *Milling of maraging steel components produced by selective laser melting.* The International Journal of Advanced Manufacturing Technology, 2018. **94**: p. 1895–1902.
60. Bai, Y., et al., *Microstructure and machinability of selective laser melted high-strength maraging steel with heat treatment.* Journal of Materials Processing Technology, 2021. **288**: p. 116906.
61. Turk, C., et al., *Advances in Maraging Steels for Additive Manufacturing.* BHM Berg- und Hüttenmännische Monatshefte, 2019. **164**(3): p. 112-116.

62. Bai, Y., Chaudhari, A., and Wang, H., *Investigation on the microstructure and machinability of ASTM A131 steel manufactured by directed energy deposition.* Journal of Materials Processing Technology, 2020. **276**: p. 116410.
63. Kempen, K., et al., *Microstructure and mechanical properties of selective laser melted 18Ni-300 steel.* Physics Procedia, 2011. **12**: p. 255-263.
64. Demir, A.G. and Previtali, B., *Investigation of remelting and preheating in SLM of 18Ni300 maraging steel as corrective and preventive measures for porosity reduction.* International Journal of Advanced Manufacturing Technology, 2017. **93**(5-8): p. 2697-2709.
65. Manfredi, D., et al., *From Powders to Dense Metal Parts: Characterization of a Commercial AlSiMg Alloy Processed through Direct Metal Laser Sintering.* Materials, 2013. **6**(3): p. 856-869.
66. Al-Rubaie, K.S., et al., *Machinability of SLM-produced Ti6Al4V titanium alloy parts.* Journal of Manufacturing Processes, 2020. **57**: p. 768-786.
67. 3D Systems, I. *LaserForm Maraging Steel*. 2022 [Access date: 25/05/2022]; Available from: https://www.3dsystems.com/materials/laserform-maraging-steel.
68. Guo, P., et al., *Study on microstructure, mechanical properties and machinability of efficiently additive manufactured AISI 316L stainless steel by high-power direct laser deposition.* Journal of Materials Processing Technology, 2017. **240**: p. 12-22.
69. Bordin, A., et al., *Analysis of tool wear in cryogenic machining of additive manufactured Ti6Al4V alloy.* Wear, 2015. **328-329**: p. 89-99.
70. Oliveira, A., Jardini, A., and Del Conte, E., *Effects of cutting parameters on roughness and residual stress of maraging steel specimens produced by additive manufacturing.* The International Journal of Advanced Manufacturing Technology, 2020. **111**: p. 1-11.
71. Neuenfeldt, M., Zanger, F., and Schulze, V., *Influence of lpbf process parameters on milling of a maraging tool steel.* MM Science Journal, 2021. **2021-November**: p. 5030-5037.
72. Tamura, S., et al., *Anisotropic Cutting Force Characteristics in Milling of Maraging Steel Processed Through Selective Laser Melting.* Journal of Manufacturing Science and Engineering, 2021. **144**(3): p. 1-16.
73. de Oliveira, A.R. and Del Conte, E.G., *Concurrent improvement of surface roughness and residual stress of as-built and aged additively manufactured maraging steel post-processed by milling.* The International Journal of Advanced Manufacturing Technology, 2021. **116**(7): p. 2309-2323.
74. Wüst, P., Edelmann, A., and Hellmann, R., *Areal surface roughness optimization of maraging steel parts produced by hybrid additive manufacturing.* Materials, 2020. **13**(2): p. 1-17.
75. Du, W., Bai, Q., and Zhang, B., *Machining characteristics of 18Ni-300 steel in additive/subtractive hybrid manufacturing.* The International Journal of Advanced Manufacturing Technology, 2018. **95**: p. 2509–2519.
76. Du, W., Bai, Q., and Zhang, B., *A Novel Method for Additive/Subtractive Hybrid Manufacturing of Metallic Parts.* Procedia Manufacturing, 2016. **5**: p. 1018-1030.
77. Sarafan, S., et al., *Evaluation of Maraging Steel Produced Using Hybrid Additive/Subtractive Manufacturing.* Journal of Manufacturing and Materials Processing, 2021. **5**(4): p. 107.
78. Silva, T.E.F., et al., *Comparison of the machinability of the 316L and 18Ni300 additively manufactured steels based on turning tests.* Proceedings of the Institution of Mechanical Engineers, Part L: Journal of Materials: Design and Applications, 2021. **235**: p. 2207-2226.
79. Laínho, M., *Machinability studies of additively manufactured 18Ni300 maraging steel*. 2020, MSc Thesis, University of Porto: Porto.
80. Gregório, A.V.L., et al., *A Methodology for Tribo-Mechanical Characterization of Metallic Alloys under Extreme Loading and Temperature Conditions Typical of Metal Cutting Processes.* Journal of Manufacturing and Materials Processing, 2022. **6**(2): p. 46.
81. *Chapter 3 Tribology of the tool-chip and tool-workpiece interfaces*, in *Tribology and Interface Engineering Series*, V.P. Astakhov, Editor. 2006, Elsevier. p. 124-219.

82. Silva, T., et al., *Mechanical Behaviour of Maraging Steel Produced by SLM.* Procedia Structural Integrity, 2021. **34**: p. 45-50.
83. Pinto Soares, J., *Aços - Características, Tratamentos*. 6ª ed. 2009: Publindústria.
84. Chakravarthi, K.V.A., et al., *Microstructure, properties and hot workability of M300 grade maraging steel.* Defence Technology, 2018. **14**(1): p. 51-58.
85. Mougo, A.L., Campos, F.O., and Araujo, A.C., *Size Effect on the Micromilling of the Super Duplex Stainless Steel*, in *International Conference on Micro Manufacturing - 4M/ICOMM2015*. 2015: Milano, Italy.
86. Thakur, D., B, R., and Vijayaraghavan, L., *Effect of High Speed Cutting Parameters on the Surface Characteristics of Superalloy Inconel 718.* Lecture Notes in Engineering and Computer Science, 2010. **2185**.
87. Rodrigues, A.R. and Jasinevicius, R.G., *2 - Machining scale: Workpiece grain size and surface integrity in micro end milling*, in *Microfabrication and Precision Engineering*, J.P. Davim, Editor. 2017, Woodhead Publishing. p. 27-68.
88. Singh, V., Venkateswara Rao, P., and Ghosh, S., *Development of specific grinding energy model.* International Journal of Machine Tools and Manufacture, 2012. **60**: p. 1-13.
89. Muthusamy Subramanian, A.V., Nachimuthu, M.D.G., and Cinnasamy, V., *Assessment of cutting force and surface roughness in LM6/SiCp using response surface methodology*. Journal of Applied Research and Technology, 2017. **15**(3): p. 283-296.
90. Acevedo, R., et al., *Residual stress analysis of additive manufacturing of metallic parts using ultrasonic waves: State of the art review.* Journal of Materials Research and Technology, 2020. **9**(4): p. 9457-9477.